

**Magnetic Traps and Guides for Bose-Einstein  
Condensates on an Atom Chip: Progress toward a  
Coherent Atom Waveguide Beamsplitter**

by

**Peter D. D. Schwindt**

B.A./B.S., The Evergreen State College, 1997

A thesis submitted to the  
Faculty of the Graduate School of the  
University of Colorado in partial fulfillment  
of the requirements for the degree of  
Doctor of Philosophy  
Department of Physics

2003

This thesis entitled:  
Magnetic Traps and Guides for Bose-Einstein Condensates on an Atom Chip:  
Progress toward a Coherent Atom Waveguide Beamsplitter  
written by Peter D. D. Schwindt  
has been approved for the Department of Physics

---

Eric A. Cornell

---

Dana Z. Anderson

Date \_\_\_\_\_

The final copy of this thesis has been examined by the signatories, and we find that both the content and the form meet acceptable presentation standards of scholarly work in the above mentioned discipline.

Schwindt, Peter D. D. (Ph.D., Physics)

Magnetic Traps and Guides for Bose-Einstein Condensates on an Atom Chip: Progress  
toward a Coherent Atom Waveguide Beamsplitter

Thesis directed by Dr. Eric A. Cornell

Atom interferometry has proven itself to be an extremely sensitive technology for measuring rotations, accelerations, and gravity. Thus far, atom interferometers have all been realized with atoms moving through free space and are restricted to the Mach-Zender configuration. However, if the atoms are guided, the shape of the interferometer can be customized to measure the inertial effect of interest, e.g. a ring or figure-eight interferometer could be realized. The enabling technology for guiding atoms is the "atom chip," where miniature copper wires are patterned onto a substrate and placed inside a vacuum chamber allowing the atoms to be only microns away. Current through these wires generates a magnetic field that can be configured to create a 2-D guiding potential or a 3-D trapping potential. My research has been focused on building a versatile apparatus for atom chip experiments with Bose-Einstein condensates (BEC) and studying the behavior of a BEC in a waveguide beam splitter, the primary element of an interferometer. Our apparatus collects  $^{87}\text{Rb}$  atoms in a magneto-optical trap, precools them, and delivers them to the atom chip. On the chip we have demonstrated that we can capture the atoms in several types of micro-magnetic traps, and once the atoms are trapped, we evaporatively cool them to form a BEC. Our main focus has been using the BEC as a single mode atomic source for characterizing the coherence properties of a waveguide beamsplitter. To this point, small current deviations inside the  $10 \times 20 \mu\text{m}$  copper conductors prevent the coherent operation of the beamsplitter, and we propose ideas to improve the beamsplitter's performance.

## **Dedication**

To my wife,  
Susan E. Duncan, for all of her love and support.

## Acknowledgements

My graduate career here at JILA and CU has been great experience due to the many wonderful and inspirational people with whom I have had the pleasure to work. First I would like to thank my advisor Eric Cornell. I am fortunate to have been advised by someone with such a great enthusiasm for experimental physics and an extensive knowledge of atomic physics. My second advisor Dana Anderson has taught me much about the technical aspects of our experiment, and his knowledge of optical physics brings a fresh perspective to our atom-optics experiment. I thank both of my advisors for their numerous inspirational ideas and wise guidance throughout my years here at JILA.

I could not have asked for two better people to work with in the lab than Tetsuo Kishimoto and my fellow grad student Ying-Ju Wang. I have spent many long days and nights with them in the lab, and without them this thesis would not have been possible. Tetsuo's enthusiasm, creativity, and sense of humor has kept Ying-Ju and me motivated during some discouraging times, and he has taught us much about the subtler aspects of running our experiment. Ying-Ju and I have been able to learn a lot from each other, and working with her has been so much fun.

Numerous other people have helped me out along the way. The advice and encouragement from Carl Wieman and Debbie Jin has been very helpful. When I first started working in the lab I was fortunate to work with Dirk Mueller on the first magnetic guiding experiments. He guided me through my first electronics and optics projects and

taught me the basics of building a vacuum system and making a MOT. The design of our apparatus was helped greatly by Heather Lewandowski and Dwight Whitaker. Since they had designed a similar apparatus a year before we started ours, their advice was invaluable. I also appreciate the help of the many people who have worked in our lab including Wonho Jhe, Nathan Koral, Volker Schweikhard, and Quentin Diot. I also thank all of the people in the Anderson, Cornell, Wieman, and Jin groups for numerous helpful discussions and for letting me borrow some very nice equipment.

Support staff here at JILA has been truly excellent. Leslie Czaia assembled the pyramid mirror for our pyramid MOT and has given us very useful advice on assembling our atom chip holder. The people in the electronics shop and the machine shop are always willing to help solve problems, and their superb craftsmanship contributed significantly to our experiment.

Last I would like to thank my friends and family for their support. My wife Susan kept me going and put up with numerous late nights while I wrote this thesis, and I thank her for proofreading the final copy. I thank Anne Curtis for her proofreading services as well. Any mistakes that remain are my own. My parents April and Fred have always given me support and encouragement. Finally my good friends Adela Marian, Anne Curtis, Malcolm Rickard, and Mike Dunnigan have make my stay here in Boulder a lot of fun.

## Contents

### Chapter

<b>1</b>	Introduction	1
1.1	Atom Optics . . . . .	3
1.1.1	Guiding Atoms . . . . .	4
1.2	Atom Chips . . . . .	5
1.3	Guided Atom Interferometry . . . . .	7
1.4	Thesis Overview . . . . .	9
<b>2</b>	The Experimental Apparatus	11
2.1	Vacuum System . . . . .	12
2.2	Laser System . . . . .	15
2.3	The Pyramid-MOT Chamber . . . . .	18
2.3.1	MOT and Magnetic Trap Diagnostics . . . . .	21
2.3.2	Mirror Coatings . . . . .	23
2.4	Transfer between Pyramid MOT and Evaporation Chambers . . . . .	26
2.5	The Evaporation Chamber . . . . .	27
2.5.1	Imaging in the HIP Trap . . . . .	29
2.6	Application Chamber . . . . .	34
2.6.1	Atom-Chip Assembly . . . . .	34

<b>3</b>	<b>The Atom Chip</b>	<b>38</b>
3.1	Magnetic Guiding . . . . .	39
3.2	The Chip . . . . .	42
3.3	Imaging on the Atom Chip . . . . .	44
3.4	The Coupling Region . . . . .	49
<b>4</b>	<b>Transferring the Atoms to the Atom Chip</b>	<b>56</b>
4.1	The Permanent Magnets . . . . .	56
4.2	The Concept of Slowing and Focusing with a Coil . . . . .	60
4.2.1	A Simple Analytical Model for Slowing and Focusing . . . . .	60
4.2.2	The Analytical Model Compared to a Coil . . . . .	64
4.3	Slowing and Focusing During Transport to the Chip . . . . .	68
4.3.1	Bounce Experiment . . . . .	70
4.3.2	A New Slowing Method . . . . .	74
<b>5</b>	<b>BEC on an Atom Chip</b>	<b>80</b>
5.1	Trapping Techniques . . . . .	81
5.1.1	The Cross Trap . . . . .	81
5.1.2	The T Trap . . . . .	83
5.1.3	The L Trap . . . . .	85
5.1.4	The Big Dimple Trap . . . . .	85
5.1.5	The Z Trap . . . . .	86
5.2	Loading the T trap . . . . .	87
5.2.1	Loading the Z Trap . . . . .	92
5.3	BEC on the Chip . . . . .	93
5.3.1	Coupling the RF to the Atoms . . . . .	95
5.3.2	BEC in the T Trap . . . . .	95
5.3.3	Two BECs on the Chip . . . . .	97



5.3.4	BEC in the Big Dimple Trap . . . . .	98
5.4	Conclusions . . . . .	99
<b>6</b>	<b>The Atom Waveguide Beamsplitter and Other Experiments</b>	<b>102</b>
6.1	Single Mode Propagation . . . . .	102
6.2	Surface Effects . . . . .	106
6.2.1	Fragmentation of the Cloud . . . . .	107
6.2.2	Current Noise . . . . .	113
6.3	The Waveguide Beamsplitter . . . . .	115
6.3.1	A Two-Wire Beamsplitter . . . . .	115
6.3.2	Thermal Atom Beamsplitter . . . . .	123
6.3.3	The Beamsplitter with a BEC . . . . .	125
6.4	Outlook for the Waveguide Beamsplitter . . . . .	132
	<b>Bibliography</b>	<b>137</b>

## Tables

### Table

2.1	Gold versus Dielectric Coated Pyramid . . . . .	25
4.1	Coils for Slowing and Focusing . . . . .	68
4.2	Results of Slowing and Focusing . . . . .	78
5.1	Results of Loading the T Trap and the Z Trap . . . . .	89
6.1	Survey of Fragmentation Results . . . . .	112

## Figures

### Figure

1.1	The Sagnac and Mach-Zender Interferometers . . . . .	8
2.1	Schematic of the Three Chamber System . . . . .	13
2.2	Vacuum System . . . . .	14
2.3	MOPA Schematic . . . . .	15
2.4	$^{87}\text{Rb}$ Levels . . . . .	17
2.5	Pyramid MOT . . . . .	20
2.6	Reflectivity of the Pyramid MOT . . . . .	24
2.7	Field of the Quadrupole Coils and the Permanent Magnets . . . . .	27
2.8	HIP Trap . . . . .	28
2.9	Imaging Optics . . . . .	30
2.10	Atom Chip Assembly . . . . .	35
3.1	Magnetic Sublevels . . . . .	39
3.2	Atom Chip . . . . .	41
3.3	Atom Chip Fabrication . . . . .	43
3.4	Image Timing and Expansion due to Guide Wire Push . . . . .	47
3.5	Measured and Numerical Expansion with Guide Wire Push . . . . .	48
3.6	Gradient of Small Magnets and Field from the Bias Sheet T . . . . .	49
3.7	Loading the Atom Chip . . . . .	51

3.8	Adiabatic Loading of Atom Chip . . . . .	52
3.9	Longitudinal Bias Field Produced in the Coupling Region . . . . .	54
4.1	Longitudinal Field from the Large Permanent Magnets . . . . .	57
4.2	Coils . . . . .	59
4.3	Analytical Model for Slowing and Focusing on a Linear Slope . . . . .	61
4.4	Analytical Model compared to a Coil . . . . .	65
4.5	Timing Diagram for Stopping the Atoms . . . . .	69
4.6	Slowed Atoms . . . . .	71
4.7	Bouncing Atoms . . . . .	73
4.8	Timing Diagram for Stopping the Atoms . . . . .	74
4.9	Final Slowing and Focusing Technique . . . . .	76
4.10	Field from the T in the Main Wire . . . . .	77
5.1	Cross Wire Trapping Fields . . . . .	82
5.2	T Wire Trapping Fields . . . . .	84
5.3	L Wire Schematic . . . . .	85
5.4	Big Dimple Wire . . . . .	86
5.5	Z Trap . . . . .	88
5.6	Trapping Region . . . . .	89
5.7	Loading the T Trap . . . . .	90
5.8	Images of loading the T Trap and the Z Trap . . . . .	91
5.9	Loading the Z Trap . . . . .	94
5.10	Time of Flight Images of the BEC on the Chip . . . . .	96
5.11	Two BECs on the Chip. . . . .	98
5.12	The Big Dimple Wire and the L-Shaped Wire . . . . .	100
6.1	Releasing the BEC into the Waveguide . . . . .	104

6.2	Single Mode Propagation in the Waveguide . . . . .	106
6.3	A Fragmented Cloud . . . . .	107
6.4	Fragmentation of the Cloud while it Propagates . . . . .	108
6.5	Fragmentation of the Cloud in the Big Dimple Trap . . . . .	109
6.6	Model of the Corrugated Potential . . . . .	113
6.7	The Two Wire Beamsplitter . . . . .	116
6.8	Eigenmodes of a Waveguide Beamsplitter . . . . .	119
6.9	The Beamsplitter Region of the Chip . . . . .	124
6.10	Splitting a BEC . . . . .	127
6.11	Fragmentation of a BEC in the Beamsplitter . . . . .	129
6.12	Model of a Beamsplitter with a Current Deviation . . . . .	131
6.13	A New Beamsplitter Idea . . . . .	135

## Chapter 1

### Introduction

Interferometry has a long established tradition of being an exquisitely sensitive measuring technique. The first light interferometers were developed in the 19th century, and perhaps the most famous interferometry experiment of the era was the Michelson-Morley experiment in 1887 that found a null result while trying to prove the existence of ether, the proposed propagation medium for light [1]. With the proposal by de Broglie in 1924 that matter should exhibit wave-like behavior, it became clear that a matter interferometer should, in principle, be possible as well. Indeed, three years after the de Broglie proposal, electron diffraction experiments showed the wave-like behavior of massive particles [2], and the demonstration of the first electron interferometer in 1954 [3, 4] and the first neutron interferometer in 1962 [5] paved the way for a host of matter-wave-interferometry experiments. Atom interferometry was experimentally realized relatively recently in 1991 when a series of micro-fabricated transmission gratings were used to split and recombine an atomic beam [6, 7]. These first atom interferometers used periodic material gratings, but it is also possible to use an off-resonant periodic light field [8]. A second class of atom interferometers was developed only months after material grating interferometers [9, 10]. These experiments achieved spatial separation of an atomic beam by applying off-resonant Raman light pulses, and the recoil momentum transferred to the atoms from the electromagnetic field separated and recombined the atoms.

Neutral atom interferometers are sensitive to electric, magnetic, and electromagnetic fields due to the atom's internal level structure but are finding the widest use in sensing inertial and gravitational effects. Atom interferometers are beginning to reach the sensitivity provided by traditional inertial and gravitational sensors. In fact, atom interferometers already claim the highest short term sensitivity to rotation and are starting to be a viable technology for measuring gravity and gravity gradients [11]. While atom interferometers appeared relatively late because the atom beamsplitter technology was not available [12], they are now proving to be a more practical technology compared to other matter wave interferometers. In fact, work is beginning to create a field-ready gravity gradiometer using atom interferometry technology, and this gravity gradiometer would be the first portable matter wave interferometer [13].

The Sagnac effect provides a good example of the inherent sensitivity of an atom interferometer [14]. When a photon or a massive particle moves through the split path of the interferometer, a rotation in the plane of the interferometer causes a small path length difference, giving rise to a relative phase shift between the two paths

$$\Delta\phi = \vec{A} \cdot \vec{\Omega} \frac{E_r}{\hbar c^2} \quad (1.1)$$

where  $A$  is the enclosed area of the two paths,  $\Omega$  is the rotation rate of the interferometer, and  $E_r$  is the relativistic energy of the particle traversing the interferometer. The dramatic advantage of using atoms over light to measure this phase shift is that an atom's relativistic energy (given by  $mc^2$ ) is a factor of  $10^{11}$  greater than the relativistic energy of a visible photon (given by  $h\nu$ ). This large “on-paper” enhancement in sensitivity to rotation is the main motivation for past and current research into the development of atom gyroscopes. However, it is not possible to achieve all eleven orders of improvement mainly because of a much smaller atom flux and a smaller enclosed area compared to optical gyroscopes, but three to four orders of magnitude enhancement in sensitivity can still be expected [15].

## 1.1 Atom Optics

The successful development of atom interferometers is rooted in the field of atom optics, the study of the physics of atomic matter waves. The manipulation of the matter waves is in many ways analogous to the manipulation of optical electromagnetic waves, and a major effort of atom optics is to create atom-optical elements similar to their optical counterparts. Atom mirrors [16–20] and atom lenses [21–24] using magnetic and electromagnetic fields have all been demonstrated. Of great importance to atom interferometry is the advent of atomic beamsplitters. The richness of atom optics becomes apparent in the types of beamsplitters used in the atom interferometers mentioned above. The material grating beamsplitters simply modify the external degrees of freedom of an atom’s wavefunction, and the beamsplitter’s function does not depend strongly on the type of atom used. The light pulse beamsplitter relies on the internal level structure of the atom to modify its external degrees of freedom and thus can only be used for a particular atom in a particular state. Each atom offers the experimenter a different choice of mass, internal electronic structure, magnetic moment, polarizability, etc., for use in the atom-optical element of interest.

Major advances in atom optics in the last twenty years have been propelled by the rapid progress in the use of laser light to manipulate atoms. As an atom absorbs or emits a photon, it exchanges momentum with the photon, giving rise to a light force, and the energy of the photon can interact with the atom conservatively through the dipole-dipole interaction or non-conservatively by changing the internal state of the atom. The narrow band-width of the laser allows precise control of these interactions. The laser makes possible many of the atom optical element already mentioned, and it also has improved the atomic sources for atom optics. The radiation pressure of a properly tuned laser on atoms can be used to slow an atomic beam or [25–27] to transversely cool it [28,29]. The laser light can also be used to select the desired internal state of the atom



for the particular atom optics experiment. Perhaps the greatest advance in the laser manipulation of atoms is the use of the laser plus an inhomogeneous magnetic field to not only cool the atoms but trap them as well [30]. The magneto-optical trap (MOT) uses the magnetic field to give the radiation force of the counter-propagating beams of light a spatial dependence, providing a trapped cloud of atoms with unprecedented low temperatures and high densities. The MOT revolutionized low temperature atomic physics, and many atomic physics experiments today rely on the MOT as a reliable and robust source of cold trapped atoms. For atom optics the MOT can provide a brighter source of atoms, and more precise control of the atoms deBroglie wavelength can be achieved with the initially lower temperature of the MOT.

The MOT and other laser cooling and trapping techniques made possible the demonstration of perhaps the ultimate atomic source for atom optics, a Bose-Einstein condensate. A Bose-Einstein condensate (BEC) in a dilute gas was demonstrated in 1995 first in the group of Cornell and Wieman with rubidium [31] and later in the groups of Ketterle with sodium [32] and Hulet with lithium [33]. The discovery of BEC later was recognized with the 2001 Nobel prize in physics. While the study of the varied properties of BECs is a vast field itself, it has just in the last few years started to be used as a source for atom-optics experiments. As something that has been dubbed the “atom laser,” the BEC is sure to continue to find wider use in atom optics as the techniques for producing a BEC become more accessible.

### 1.1.1 Guiding Atoms

Analogous to guiding light in optical fibers, atoms can be guided in various waveguide structures. Previous work in our group and others has shown that atoms can be guided through hollow-core glass fibers where off-resonant light, also guided in the fiber, provides a force to transversely confine the atoms as they move down the fiber [34–37]. Another method of guiding atoms utilizes magnetic fields. An inhomogeneous magnetic

field provides a force on the magnetic dipole of the atoms, and by arranging the fields to create 2-D confinement, the atoms can be guided. Large, macroscopic guides have been created with both permanent magnets and current-carrying wires [38–42], but guiding atoms with smaller magnetic structures seems to be very promising. Photolithography can be used to pattern small conductors on the substrate, and a current through these wires can create a guiding potential. The process of photolithography reproducibly generates precisely patterned wires in any configuration in a planar geometry. These substrates have been used by our group and others to guide the atoms with various wire configurations [43–45], and several atom waveguide devices have been demonstrated, including a beamsplitter [46, 47] and a switch [48] for thermal atoms.

## 1.2 Atom Chips

The substrates described above contained a single guide or device on them. The term “atom chip” has been coined to describe a substrate onto which many atom-optical devices have been integrated. Atom chips aim to miniaturize many of the atom-optics devices mainly using small current-carrying wires. The large size of traditional magnetic potentials relegates them to mere containers for the atoms, but the close proximity of the field-producing elements to the atoms on an atom chip allows the complex manipulation of atomic wave packets. To date, most successful implementations of atom chip technology have used only lithographically patterned current-carrying wires to create a wide variety atom-optical elements. Perhaps the most dramatic example of an integrated atom chip is that used in the Hänsch group in Germany [49, 50]. Their chip was used to magnetically trap atoms in a number of configurations, to adiabatically transport the atoms with an “atom motor,” and to create a novel mirror MOT for collecting atoms near the surface of the chip. A reflective layer deposited on the surface of the chip creates the mirror for the mirror MOT. Another group implemented a mirror MOT along with a waveguide beamsplitter for thermal atoms [46]. Besides current-carrying

wires, other-field producing elements can be implemented on a atom chip. There is a proposal to implement a quantum computation scheme on an atom chip using both electric and magnetic fields to entangle pairs of atoms through controlled collisions [51]. In this scheme the chip's conductors are used to create both the electric and magnetic fields. Small optical cavities could also be placed on the chip and be used for single-atom detection and manipulation on the chip [52]. An interesting variant of an atom chip is used by the Prentiss group in which high  $\mu$  magnetic foils wrapped with wires are mounted rigidly in a chip-like structure [53]. The foils are centimeters long and less than a millimeter in length, and a set of four foils can produce a strong transverse magnetic gradient for guiding. This chip is also coated with a reflective layer for use in a mirror MOT.

The main focus on atom-chip technology in our group and others over the last three to four years has been to create a BEC on the chip. The main challenge of atom-chip technology has been to load a sufficient number of atoms at a low enough temperature to be able to perform efficient evaporative cooling. In a traditional BEC experiment a large volume magnetic trap with a large trap depth is used to capture atoms from a MOT before evaporation to BEC begins. Although atom chips can create a wide variety of magnetic potentials for manipulating atoms, magnetic traps made from the small conductors on the chip have very small trap volumes and are only hundreds of microns away from the chip's surface. The trap volume can be made large, but then the trap is very weakly confining and has a shallow trap depth. Only the Hänsch group has succeeded in capturing atoms from a mirror MOT in a magnetic trap with sufficient atom number to make a BEC using only wires on the chip, but after evaporation the BEC is quite small, with slightly more than  $10^3$  atoms [54]. Other groups loading atoms from a mirror MOT use a wire greater than  $500\text{ }\mu\text{m}$  in diameter imbedded in or under the chip [55,56]. The larger wire allows a larger current, giving the magnetic trap created by the wire a larger capture range and trap depth. These techniques yield BECs with

$10^4 - 10^5$  atoms. Our group and the Zimmermann group magnetically trap the atoms off-chip and then magnetically transfer the atoms to the chip for the final evaporation to make a BEC [57]. Again the BECs contain  $10^4 - 10^5$  atoms. The technique that has achieved the greatest atom number in the BEC on the chip was developed by the Ketterle group [58,59]. They make the BEC off-chip and transport the BEC to the chip using optical tweezers achieving  $10^6$  atoms in the BEC.

### 1.3 Guided Atom Interferometry

The combination of guided atoms and a guided atom beamsplitter could lead to a new type of atom interferometer, and this is the ultimate goal of the research in this thesis. Theoretical consideration to several types of guided atom beamsplitters and interferometers is given in references [60–64]. A guided atom interferometer has several advantages over the current free-space interferometers. The enclosed area of the free-space atom interferometers is on the order of one  $\text{cm}^2$  or less due to the small splitting angles of the beamsplitters, severely limiting the sensitivity of the device (Equation 1.1). To achieve even these small enclosed areas, the interferometers are meters long, and their length is limited by the gravitational sag of the atomic beam. Guided atom interferometers offer larger enclosed areas in a much smaller package. Because the atoms are guided, the splitting angle of the guided beam can be much greater allowing a larger enclosed area in a compact apparatus. Conceivably, an enclosed area of many square centimeters could be formed by a circular guide. Another disadvantage of free-space interferometers is that they are generally in the Mach-Zender configuration. For making a measurement of rotation, this is not the ideal geometry. In the two separated paths of a Mach-Zender interferometer, an atom's wavefunction can experience different potentials, giving a phase shift between the two paths that is not due to the rotation (Figure 1.1). Ideally, each part of the atom's wavefunction would traverse the same path but in opposite directions to form a Sagnac interferometer, which cancels out the

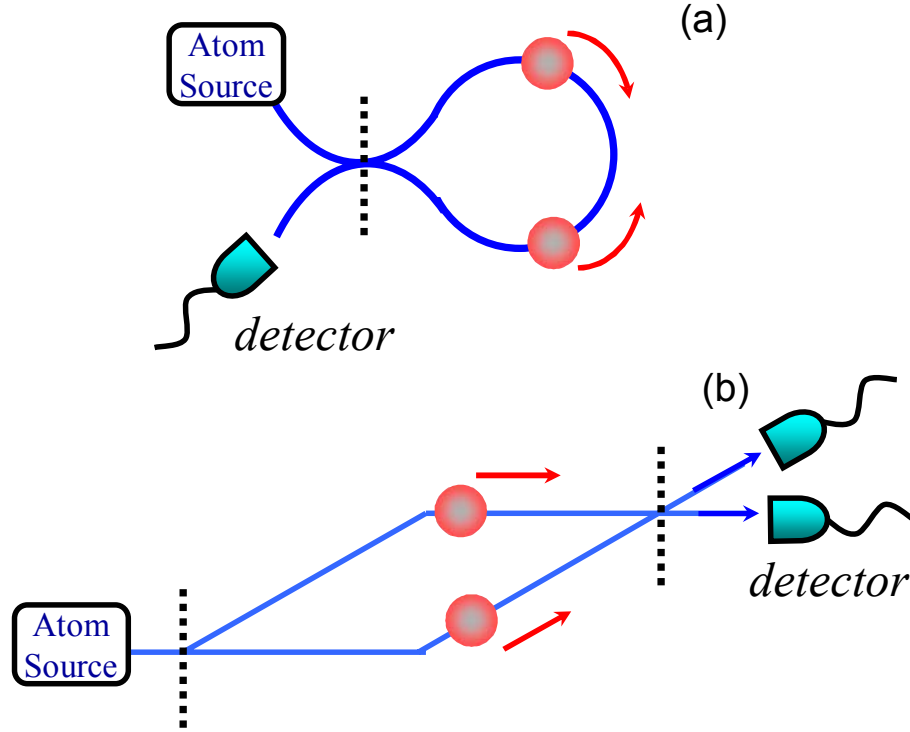


Figure 1.1: A schematic diagram of (a) the Sagnac interferometer and (b) the Mach-Zender interferometer. The loop geometry of the Sagnac rejects much of the interferometer noise that the separated paths of the Mach-Zender geometry do not. The vertical dotted lines indicate the beamsplitters.

effect of these potentials. With guided atom interferometers the Sagnac geometry can likely be realized. In general, the geometry of a guided atom interferometer can be tailored to be sensitive to the effect of interest, such as a particular multipole term of the gravitational potential, while canceling many undesirable effects.

A great challenge in the development of guided atom interferometers is to find a single-mode source of atoms. Free-space interferometers can use a thermal beam of atoms in the way free-space light interferometers can use slightly diverging light because the different spatial modes separate spatially. However, guided atom interferometers cannot tolerate multi-mode guiding (except in a very limited case [63]) because the various modes would create varying interference patterns similar to the speckle in a multi-mode optical fiber. The obvious single-mode, high-intensity source for a guided

atom interferometer is a BEC, and the major effort of this thesis is to introduce a BEC onto an atom chip containing a magnetic waveguide and a waveguide beamsplitter.

## 1.4 Thesis Overview

The stated goal of our research project for the past eight years has been to produce a guided atom interferometer. In fact, our group is currently working on two parallel projects in this direction. My own experiment is designed as the initial test bed for waveguide beamsplitters and interferometers. With this experimental apparatus we can easily change the atom chip allowing for a number of different test chips. The other experiment is designed as the type of apparatus that may be used in an actual portable guided-atom gyroscope, and they are researching various technologies to miniaturize the whole instrument. They already have fabricated a glass cell where the atom chip forms one wall of the vacuum system, and all of the atom optics experiments occur in a  $1\text{ cm}^3$  volume. The work in this thesis builds upon the work in the thesis of the previous graduate student Dirk Müller in which substrate based magnetic guiding and beamsplitting were demonstrated using MOT temperature atoms [15]. With the atom optical elements for guided atom interferometry demonstrated for thermal atoms, our next step was to build a machine to achieve BEC on an atom chip, and this is where this thesis begins. After we achieved BEC on the chip, we began to characterize the coherence properties of the atoms moving through a waveguide beam splitter, and here I present preliminary results of these experiments.

In designing our machine, we decided to take the approach of using the conventional, well-known technology of the state-of-the-art BEC machines developed in the wider Cornell-Wieman-Jin group [65,66]. We adapt the standard two vacuum chamber system for our purposes by adding a third vacuum chamber to contain an atom chip. In chapter 2, I discuss the overall system and the operation of the first two chambers of the system in which a sample of atoms is prepared for delivery to the atom chip. In chapter

3, I describe the basic principles of our integrated atom chip where three sections of the chip are designed to perform three different functions. In this chapter, I also describe how the atom chip is loaded. Chapter 4 is devoted to the transfer of the prepared sample of atoms from the second chamber of the system to the chamber containing the atom chip. Here, I describe a magnetic transfer mechanism that produces a guided and pulsed atomic beam, and I show how we can control the longitudinal speed and size the beam. We can stop the guided beam of atoms on the atom chip as it comes to its minimum longitudinal size. With the atoms stopped on the chip we can trap them and perform evaporative cooling to make a BEC, and this is the subject of Chapter 5. In this chapter I review various traps that can be formed on the chip and give results for loading and making a BEC in a few of these traps. In Chapter 6, I discuss the initial results of guiding the BEC and splitting it with the waveguide beamsplitter. A number of new effects from the atoms being in close proximity to a current-carrying wire are described as well.

## Chapter 2

### The Experimental Apparatus

In designing our apparatus, we wanted a system that could deliver a large sample of cold atoms to an atom chip. Our group has developed a number of BEC apparatuses, and we decided to modify the design of a recently built apparatus that is, by comparison to other systems, relatively easy to build [66]. This two-vacuum-chamber system has one chamber for creating a vapor-cell magneto-optical trap (MOT), and the other is an ultra-high vacuum chamber where the evaporation takes place to cool the atoms to BEC. Our modification adds a third chamber to the system to contain the atom chip and includes a magnetic transfer method to move the atoms onto the atom chip. Originally, we planned to make the BEC off-chip and subsequently transport it to the chip. However, we are not able accomplish this without heating the atoms, and now we transport a thermal cloud of atoms to the chip and trap the atoms to make the BEC on-chip. Our transport method will be discussed in the later chapters.

This chapter discusses not only the vacuum system and the laser systems but also gives details on the experimental results in the first two chambers of the vacuum system. The first two chambers are the atom source for the experiments on the atom chip, and Reference [66] gives a detailed explanation of this atom source. Below, I highlight the aspects of our system that differ from the system described in Reference [66].



## 2.1 Vacuum System

The three chambers of the system are the pyramid-MOT chamber, the evaporation chamber, and the application chamber (Figure 2.1). We make a modular system by placing a gate valve between each chamber so we can modify one chamber without affecting the integrity of the vacuum in another. In particular, we can rapidly change out the atom chip (in 3 days) without affecting the other two chambers. Each chamber has a different vacuum requirement,  $10^{-9}$ ,  $10^{-11}$ , and  $10^{-10}$  torr for the pyramid-MOT, evaporation, and application chambers respectively. When the experiment is running, the gate valves are open to allow the transfer of atoms between the chambers, and a differential pressure is maintained by limiting the conduction between the chambers. Between the pyramid-MOT chamber and the evaporation chamber there is a 6 cm long tube with a diameter of 1.06 cm, and between the evaporation chamber and the application chamber there is a 1 mm diameter pinhole to limit the conduction.

The pumping requirements for this system are significant, and the physical design of the system has to accommodate the pumping and the moving quadrupole coils that transfer the atoms from the pyramid MOT chamber to the evaporation chamber (see Section 2.4). The pyramid-MOT chamber is pumped by two ion pumps (see Figure 2.2). A 25 l/s ion pump pumps directly on the pyramid-MOT chamber. A 40 l/s ion pump pumps on the transfer tube just before the gate valve to the evaporation chamber. The evaporation chamber is pumped by a 40 l/s ion pump and a titanium sublimation pump (TSP) in a 5 cm diameter tube. The pumps for these two chambers are set far enough away from the chambers and the transfer tube to allow for the motion of the quadrupole coils. Additionally, any flanges in or near the transfer tube must be smaller than the 10 cm spacing between the quadrupole coils, limiting flange size to  $3\frac{3}{8}$  inch or less. For baking and pumping down these two chambers, we use a detachable pumping station with a 250 l/s turbo pump backed by a dry scroll pump. The application chamber is

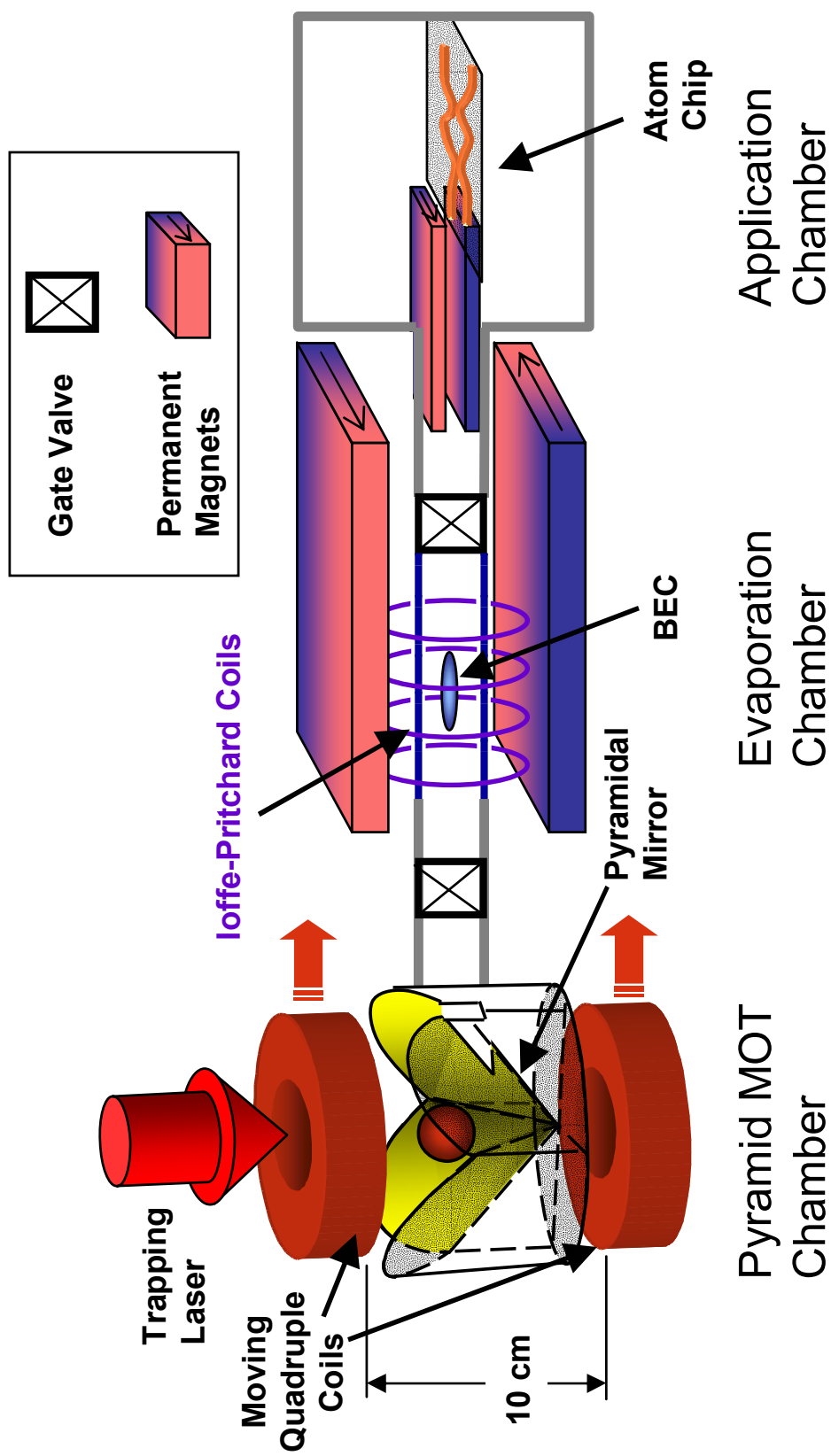


Figure 2.1: Schematic of the Three Chamber System. A gate valve separates each chamber for easy modification of the chambers. The arrows and the coloring of the permanent magnets indicate the direction of magnetization.

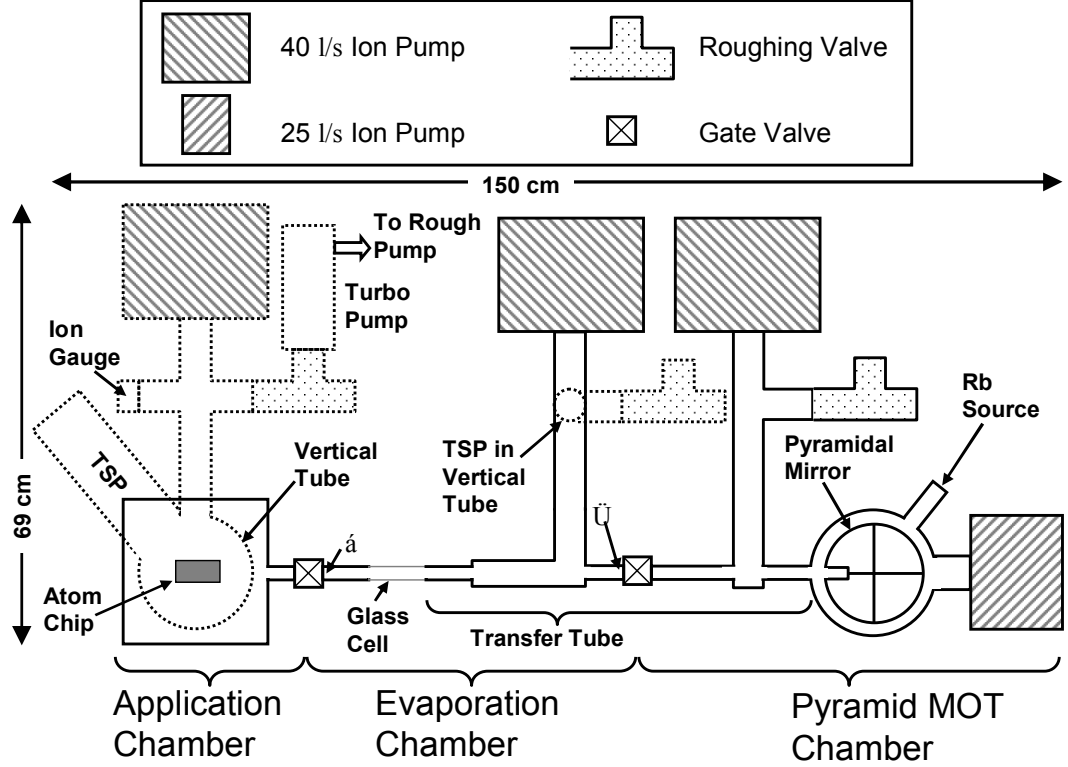


Figure 2.2: Layout of the vacuum system. The dotted lines indicate components of the vacuum system that are elevated at least 30 cm above the optical table. The rest of the system is centered 15 cm above the optical table. The † indicates the location of the  $6 \times 1.09$  cm tube for differential pumping, and the ‡ indicates the location of the 1 mm pinhole. TSP stands for titanium sublimation pump.

pumped by a 40 l/s ion pump and TSP in a 10 cm diameter tube. The larger tube for the TSP is used to increase the pumping speed as the pumping speed scales linearly with the coated surface area. For baking and pumping down the application chamber, a 70 l/s turbo pump is permanently attached to the chamber and separated from the rest of the chamber by a right-angle valve. The turbo pump is backed by the dry scroll pump on the pumping station.

The rubidium source for the MOT is contained in an appendage to the pyramid-MOT chamber (Figure 2.2). One gram of Rb in a glass ampule is contained inside a flexible stainless steel tube. After the chamber is pumped down and baked out, the glass ampule is crushed by squeezing the stainless steel tube with pliers to release the Rb into

the pyramid MOT chamber. We can control the Rb partial pressure in the chamber by heating the Rb ampule, but we usually leave the ampule at room temperature. A right-angle valve separates the ampule from the pyramid-MOT chamber so that if we have to vent the chamber to air, we can seal off the Rb source. If Rb comes into contact with air, it oxidizes, making the source useless. The valve allows us to vent the chamber several times before we need to change the Rb ampule.

## 2.2 Laser System

We use three diode lasers in this experiment. Two of the lasers are for trapping and cooling the atoms in the MOT, and the third is used as the probe laser for imaging the atoms in both the evaporation chamber and the application chamber. A diode laser in the master-oscillator power amplifier (MOPA) configuration [67, 68] with an output power of 470 mW provides the trapping and cooling light for the MOT. The master oscillator (MO) is a external-cavity grating-stabilized diode laser [69, 70] that provides 12 mW of single-frequency light at 780 nm. This light passes through two New Focus

35-dB optical isolators, after which a polarizing beamsplitter cube (PBS) directs 1 mW to a locking setup and allows the rest of the light to pass through (see Figure 2.3). The remaining 7 mW of light is directed to the power amplifier (PA) via two steering mirrors. The SDL tapered amplifier chip boosts the input light to 470 mW of output power. The output of the PA strongly diverges and has an astigmatism. The beam is collimated and shaped to be roughly square using first an aspherical lens and then a series of three cylindrical lenses. Next, the beam passes through an optical isolator and is directed to a single-mode polarization-maintaining optical fiber with another two steering mirrors. With the two mirrors and a five-axis, New Focus fiber aligner, we can couple approximately 50% of the light into the 10 m fiber such that 200 mW of single-frequency light is delivered to the optical table containing our vacuum system. To align the polarization of the input beam to the polarization axis of the fiber, we pass the beam through a quarter-wave plate and a half-wave plate to rotate the polarization. To optimize the angle of the wave plates, we monitor the polarization of the output of the fiber while manually shaking the fiber. If the input polarization is not aligned to the fiber axis, the output polarization will change as the fiber is shaken.

Since the MOPA laser provides the main trapping light, it is detuned to the red of the  $5S_{1/2}(F = 2) \rightarrow 5P_{3/2}(F' = 3)$  “cycling” transition of  $^{87}\text{Rb}$  (see Figure 2.4). To lock the MOPA to this frequency, we pass the light split off of the main beam by the PBS through a 120 MHz acoustic-optic modulator (AOM). We maximize the power in the negative first order and direct this deflected beam to a saturated-absorption spectrometer (SAS) [69]. We then peak-lock to the  $(2 \rightarrow 2', 2 \rightarrow 3')$  crossover line by dithering the diode current of the MO at  $\sim 50$  kHz and locking to the zero crossing of the error signal’s first derivative. By adjusting the frequency of the AOM, we can tune the frequency of the MOPA over several natural linewidths around the  $(2 \rightarrow 3')$  transition.

The second MOT laser is used for repumping the atoms that fall into the  $(F = 1)$

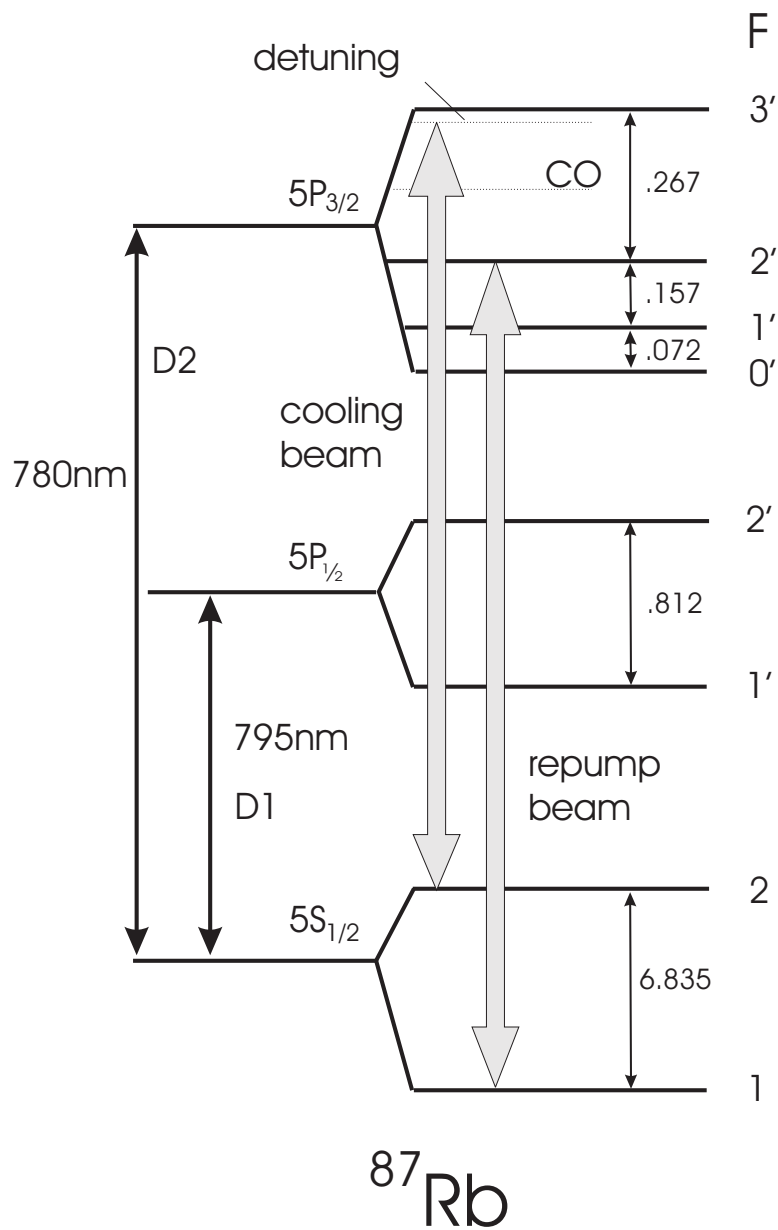


Figure 2.4: Level diagram for  $^{87}\text{Rb}$ . The MOPA and repump laser transitions are shown. CO indicates the  $(2 \rightarrow 2', 2 \rightarrow 3')$  crossover used as the lock point for the MOPA saturated absorption spectrometer. The levels splittings are given in GHz.

hyperfine ground state back to the ( $F = 2$ ) ground state. A 30-mW external-cavity grating-stabilized diode laser supplies 11 mW of light peak-locked to the  $5S_{1/2}(F = 1) \rightarrow 5P_{3/2}(F' = 2)$  transition via an SAS where we dither the diode current at  $\sim 50$  kHz to obtain the first-derivative signal. Without an AOM the repump laser cannot be widely tuned.

The probe laser is a external-cavity grating-stabilized diode laser purchased from New Focus. This laser is tuned near two different transitions depending on the chamber in which we are imaging. For imaging in the evaporation chamber, we lock near the  $5S_{1/2}(F = 1) \rightarrow 5P_{3/2}(F' = 1)$  transition, and for imaging in the application chamber we lock near the  $5S_{1/2}(F = 2) \rightarrow 5P_{3/2}(F' = 3)$  transition. The probe beam passes through two 260 MHz AOMs. The first directs the light to an SAS, and by tuning the frequency of this AOM, we change the frequency of the probe. To peak-lock the laser, we apply a 300 kHz dither to the AOM so that the light directed to the experiment is not dithered. The second AOM is essentially used as a fast shutter to control the duration of the image pulse. The difference between the frequencies of the two AOMs determines the detuning of the probe beam from the transition to which we lock. The output of the second AOM is coupled into a single-mode polarization-maintaining optical fiber and brought to the experiment to detect the atoms.

### 2.3 The Pyramid-MOT Chamber

In the first chamber of our system we collect  $^{87}\text{Rb}$  atoms from a room temperature rubidium vapor in a MOT [30]. To simplify the optics for the MOT, we use a pyramid MOT [71] where an inverted pyramidal-shaped mirror creates the necessary six beams from a single large laser beam that illuminates the entire mirror (Figure 2.5). A MOT requires circularly polarized light, and upon reflection, circularly polarized light changes handedness. The reflections inside the pyramid naturally give the correct polarizations to make a MOT. Our pyramidal mirror is constructed from four wedge-shaped pieces

of glass coated with a dielectric stack designed for high reflectivity for both s- and p-polarizations at  $45^\circ$ . The wedge-shaped mirrors are glued onto an aluminum mount creating the inverted pyramid with a diameter across the top of 9.9 cm. The pyramid is placed inside the vacuum chamber.

The beams from the MOPA and the repump laser are combined into a single beam with a polarizing beamsplitter cube and are directed to the pyramid mirror. Immediately before the beam enters the vacuum chamber, it is expanded from 0.2 cm in size to 5 cm (FWHM) to fully illuminate the mirror. The magnetic-field gradient for the MOT is produced by the two coils outside the chamber that generate a spherical quadrupole field. We set the coils' current to give a gradient of 10.5 G/cm in the vertical direction for loading the MOT. We load  $2 \times 10^{10}$  atoms into the MOT with the MOPA detuned 26 MHz to the red of the  $(2 \rightarrow 3')$  transition.

After the MOT is loaded, we magnetically trap the atoms for transfer to the evaporation chamber. Before the atoms are magnetically trapped, we perform a compressed MOT (CMOT) [72] stage to further cool and compress the atoms. We start the CMOT stage by reducing the field gradient to 2.7 G/cm and the repump power by a factor of 200. Twenty-five milliseconds later the trapping laser is detuned by 60 MHz. The CMOT is completed after a total time of 100 ms, and then the repump is switched off 2 ms before the trapping light in order to optically pump all of the atoms to the  $F = 1$  ground state. Immediately after the trapping light is switched off, the gradient from the quadrupole coils is jumped to 60 G/cm to magnetically trap the atoms in the  $|F = 1, m_F = -1\rangle$  state and is then slowly ramped to its maximum gradient of 175 G/cm over 200 ms. We are able to magnetically trap  $6 \times 10^9$  atoms, and with the trap at full gradient the resultant temperature is  $\sim 500$   $\mu$ K. While optimizing the loading of the magnetic trap, we worked to increase the initial phase-space density of the atoms in the magnetic trap. In our large MOT the density is limited by the radiation pressure from the re-radiation of photons within the cloud, which creates an outward force. Detun-



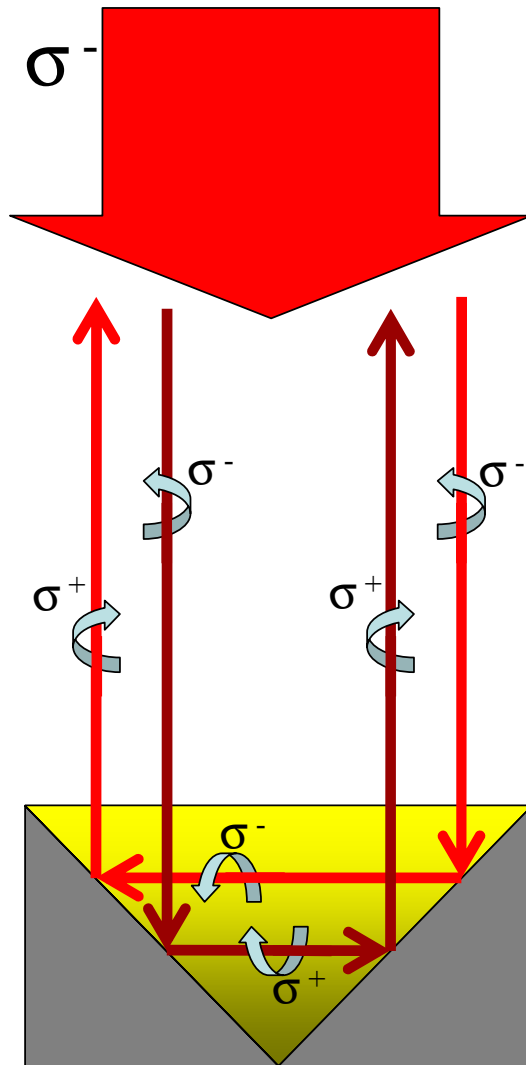


Figure 2.5: Schematic of the pyramid MOT. The large beam enters the pyramid, and the four mirrors create the necessary six beams for a MOT. The figure shows four beams with the correct polarization. The other two beams travel out of the plain of the page.

ing the trapping laser decreases the probability of absorption and reducing the repump power increases the population of atoms in the  $F = 1$  ground state, greatly reducing the radiation pressure in the MOT, thereby increasing the density. The decreased spatial extent of the cloud reduces the potential energy gained as the magnetic trap is turned on increasing the initial phase-space density of the magnetically trapped atoms. We are also careful to make sure that the center of the CMOT overlaps the magnetic trap center to avoid an additional gain in magnetic potential energy.

### 2.3.1 MOT and Magnetic Trap Diagnostics

We use two diagnostics to characterize the MOT and the magnetic trap. We determine the number of atoms by focusing the fluorescence of the trapped atoms onto a photodiode with a single lens. With the atoms inside the pyramidal mirror, the lens focuses not only the cloud but also four reflections of the cloud. Care is taken so that only the image of the cloud is incident on the photodiode. The number of trapped atoms is given by

$$N = \frac{4\pi N_\gamma}{\Omega R T_g} \quad (2.1)$$

where  $N_\gamma$  is the number of photons per second incident on the photodiode,  $\Omega$  is the solid angle subtended by the collection lens, and  $T_g$  refers to the total transmittivity of the optical surfaces between the atoms and the photodiode.  $R$ , the photon scattering rate in photons/sec/atom, is determined by

$$R = \frac{\pi\Gamma \frac{I}{I_s}}{1 + \frac{I}{I_s} + 4(\frac{\Delta}{\Gamma})^2} \quad (2.2)$$

where  $I$  is the total intensity of all of the light incident on the atoms,  $I_s$  is the saturation intensity for the  $(2 \rightarrow 3')$  transition with random polarization, which is 4.1 mW/cm<sup>2</sup>,  $\Delta$  is the detuning of the MOPA from the  $(2 \rightarrow 3')$  transition, and  $\Gamma$  is the natural linewidth of the transition.

To determine the spatial size of the cloud, we image the atoms with a charge-coupled device (CCD) camera. The fluorescence of the cloud is focused onto the CCD with a single lens. We find that a single lens works well as we need to demagnify the cloud and there is no vignetting with a single lens imaging system [66]. To image the MOT and the CMOT, we turn off the MOPA and the repump lasers with mechanical shutters approximately 1 ms after the camera shutter is opened. If we used only the camera shutter to control the exposure, the exposure time would be approximately 7 ms which would saturate the CCD camera. Imaging atoms in the magnetic trap is accomplished by shutting off the magnetic trap and turning on the repump 100  $\mu$ s before the MOPA is turned on for 200–1000  $\mu$ s. The delay between when the magnetic trap turns off and the MOPA turns on can be varied from 0.2 to 30 ms. To extract the temperature of the magnetically trapped atoms, we want to measure the in-trap size of the cloud by imaging 0.2 ms after the coils are shut off. This is complicated by the fact that turning off the coils suddenly produces eddy currents in the stainless steel chamber that persist for almost 8 ms and shakes the optical table enough to perturb the frequency of any laser on the optical table. Originally, the MOPA was on the same optical table as the vacuum system so its frequency would oscillate for several hundred milliseconds after the coils were turned off. Thus, the number of trapped atoms was unknown since the MOPA's frequency was oscillating, and the size of the cloud was unknown because the eddy currents produced an unknown magnetic field gradient causing an unknown frequency shift across the cloud due to the Zeeman effect. To solve these problems, we moved the MOPA to another optical table and brought the light to the optical table with the vacuum system using a single-mode fiber. Unfortunately, the eddy currents cannot be eliminated so we simply wait 9 ms for the eddy currents to decay before we image the atoms.

To extract the temperature of the magnetically trapped cloud, we fit the image with a 2-D Gaussian. Although the in-trap spatial distribution is not exactly Gaussian,

the fit gives a reasonable value for the half width half maximum of the cloud,  $\sigma_{HWHM}$ . The temperature and the peak density of a cloud in-trap is given by

$$T = \frac{4}{5} \frac{\mu_B g_F}{k_b} B'_x \sigma_{HWHM} \quad (2.3)$$

$$n_{peak} = 10.16 \frac{N}{\sigma_{HWHM}^3} \quad (2.4)$$

where  $\mu_B$  is the Bohr magneton,  $g_F$  is the Landé  $g$ -factor, and  $k_b$  is Boltzmann's constant.  $B'_x$  refers to the radial (horizontal) gradient of the spherical quadrupole field. The horizontal direction is used for the determination of the temperature because we image the MOT and magnetic trap at a  $\sim 35^\circ$  angle from the vertical such that the vertical  $\sigma_{FWHM}$  is a combination of the vertical and horizontal size. Because the cloud expands for 9 ms before we image, we do not measure the in-trap size. The size of the cloud as a function of time is, assuming an initial spatial Gaussian distribution,

$$\sigma_{HWHM}(t) = \sqrt{\left(\frac{5}{4} \frac{k_b}{\mu_B g B'_x} T\right)^2 + \frac{k_b T}{2 \ln(2) m_{Rb}} t^2} \quad (2.5)$$

where  $m_{Rb}$  is the mass of  $^{87}\text{Rb}$ . Using  $\sigma_{HWHM}(0 \text{ ms}) = \sigma_{HWHM}(9 \text{ ms}) - 0.6 \text{ mm}$ , we can calculate the temperature over the range of 300-1000  $\mu\text{K}$  with a maximum error of 3% at 300  $\mu\text{K}$ .

### 2.3.2 Mirror Coatings

We have tried two different coatings for the pyramidal mirror. Our first pyramid was coated with an unprotected gold layer. The pyramid was assembled first, and then the gold layer was evaporated onto the mirror surface. Because of the concave geometry of the inverted pyramid, the gold was not evaporated evenly across the surfaces. We chose gold because of its high reflectivity at 780 nm and because the induced phase shift between s- and p-polarizations upon reflection at  $45^\circ$  is generally smaller than for dielectric coatings (see Table 2.1). Although we were able to make a large MOT with the gold pyramid, transfer into the magnetic trap proved difficult to optimize. Additionally,

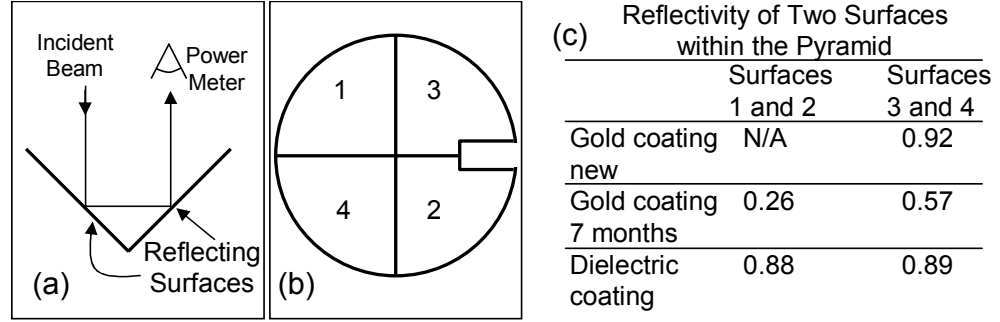


Figure 2.6: (a) By shining a laser that is circularly polarized into the pyramid, we measure the power reflected by two surfaces. The angle of incidence for both reflections is  $45^\circ$  (b) The drawing shows the four reflecting surfaces of the pyramidal mirror. (c) The table displays the ratio of the reflected power to the incident power. The ratio includes the transmittivity of the anti-reflective coated window over the pyramid.

the results were not reproducible over a time scale of weeks. We attribute these problems to a power imbalance between the beams in the pyramid MOT. The reflectivity of each pyramid surface largely determines the power in each beam in the MOT, although we can make small adjustments with the position of the incident beam. We found that the position of the CMOT is affected by the power balance, and as mentioned above, the temperature of the atoms in the magnetic trap is affected by position of the CMOT. We used shim coils to try and overlap the center of the CMOT with the magnetic trap, but it was very difficult to load into the magnetic trap without heating the atoms. We also found that the center of the CMOT drifted over time. This occurred because the reflectivity of the pyramidal mirror was changing over time due to the slow deposition of rubidium onto the gold surfaces. Over a period of seven months the reflectivity of a single surface dropped on average by 30% (see Figure 2.6).

Realizing that unprotected gold is a poor surface as it has an affinity for rubidium, we now use a pyramidal mirror coated with a dielectric stack. A dielectric stack can produce exceptional reflectivity ( $> 98\%$  for a single surface reflection), but the phase shift between the s- and p-polarizations upon reflection can be unpredictable. For the MOT we use circularly polarized light, and under ideal conditions the phase shift

Table 2.1: A comparison of the performance of the gold coated and dielectric coated pyramids.  $R$  and  $\alpha$  are measured at an angle of incidence of  $45^\circ$ .

	Gold	Dielectric
Anomalous phase shift $\alpha$ (single surface reflection)	$\sim 17^\circ$	$\sim 22^\circ$
Reflectivity $R$ (single reflection)	0.97 (New)	0.95
# in MOT	$1.1 \times 10^{10}$	$1.3 \times 10^{10}$
# in Magnetic Trap	$1 \times 10^9$	$5 \times 10^9$
Transfer Efficiency	10%	40%
Temperature ( $\mu\text{K}$ )	650	500

between the two polarizations upon reflection is  $180^\circ$ , e.g. left circular polarization goes to right circular polarization. Expressed in terms of the transverse electric field vector, circularly polarized light does the following upon reflection

$$\frac{E}{\sqrt{2}} \begin{pmatrix} 1 \\ e^{i\frac{\pi}{2}} \end{pmatrix} \xrightarrow{\text{reflection}} \frac{E\sqrt{R}}{\sqrt{2}} \begin{pmatrix} 1 \\ e^{i(-\frac{\pi}{2}+\alpha)} \end{pmatrix} \quad (2.6)$$

where  $E$  is the electric field,  $R$  is the reflectivity of the surface, and  $\alpha$  is the anomalous phase shift of the reflecting surface.

Our current pyramid has a single surface reflectivity of  $\sim 95\%$ , and over nine months we have not seen a significant reduction in the reflectivity. The reflectivity of the dielectric coating is  $< 98\%$  because we asked the coating company to optimize for a small  $\alpha$  between s- and p-polarization. Unfortunately, the attempted optimization reduced the reflectivity of the coating, and they could not control the phase shift. Surprisingly, even with an anomalous phase shift greater than that of gold, the dielectric coated pyramid altogether out performs the gold pyramid for loading the MOT and the magnetic trap (Table 2.1). Also, we do not need to use shim coils to move the center of the CMOT since the CMOT is naturally centered on the magnetic trap because of the good power balance of the beams. Another dielectric coating, optimized only for high reflectivity for both s- and p-polarizations, gave  $98\%$  reflectivity with a similar  $\alpha$  of  $20^\circ - 25^\circ$ , and our next pyramid will use these mirrors.

## 2.4 Transfer between Pyramid MOT and Evaporation Chambers

With the atoms magnetically trapped, we transfer the atoms to the evaporation chamber by physically moving the magnetic quadrupole trap between the two chambers. The quadrupole coils are mounted on a servo controlled linear track that is able to move the atoms to the evaporation chamber 58 cm away in 1.4 s. To allow the atoms out of the pyramid MOT chamber, a  $1.3 \times 1.3$  cm hole is cut in one edge of the pyramidal mirror. The main loss with this transport method occurs when the atoms pass through

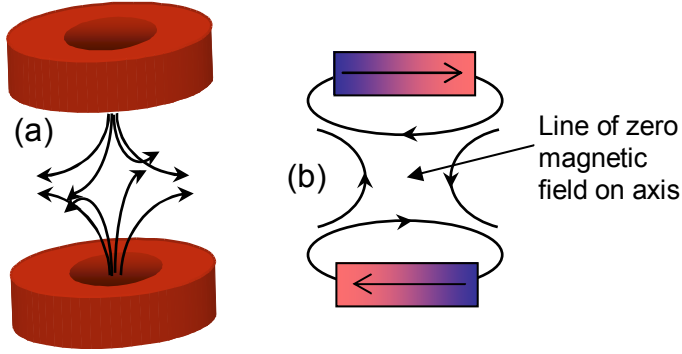


Figure 2.7: (a) Shows the field lines of the quadrupole coils. (b) Shows the 2-D field of the permanent magnets.

a 6-cm-long tube that provides the differential vacuum between the two chambers. The transfer efficiency through the tube is  $\sim 80\%$  depending of the temperature of the cloud.

As shown in Figure 2.1, there are two permanent magnets outside the evaporation chamber that provide a strong 2-D quadrupole field with a gradient of 650 G/cm. This 2-D quadrupole is oriented  $45^\circ$  relative to the spherical quadrupole of the moving coils (see Figure 2.7). Thus, the atoms are moved slowly into the magnets' quadrupole to allow the increasing of the gradient and the rotation of the field to occur adiabatically, which takes  $\sim 2$  s. Once the atoms are past the entrance to the permanent magnets, we move the atoms to the center of the hybrid Ioffe-Pritchard trap (see next section).

## 2.5 The Evaporation Chamber

The evaporation chamber is mainly a  $1.9 \times 1.9$  cm square glass tube that is 10 cm long. The cell is surrounded by the hybrid Ioffe-Pritchard (HIP) trap that uses both permanent magnets and electromagnetic coils to provide the trapping fields. The radial confinement is provided by the two permanent magnets and the axial confinement is provided by four "Ioffe-Pritchard (IP)" coils (see Figure 2.8). The two outer coils provide a large axial field and curvature. The axial field is partially canceled in the center by the two inside coils to set the longitudinal bias field in the HIP trap. The coils are



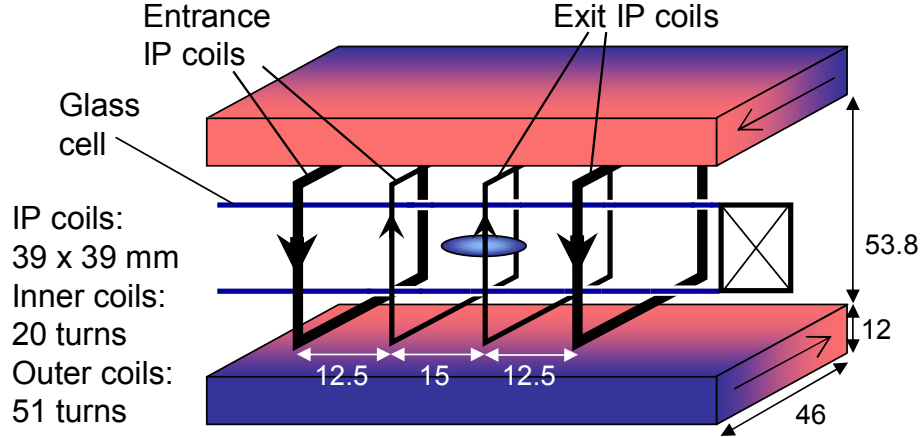


Figure 2.8: The dimensions of the IP coils and the permanent magnets used in the HIP trap are shown. All of the dimensions are in mm.

designed such that all four coils can be connected in series and powered with a single current supply, or the entrance and the exit IP coils can be run separately. Typical trap frequencies in our HIP trap are 170 Hz in the radial direction and 7 Hz in the axial direction.

To transfer the atoms to the HIP trap from the quadrupole coils, we slowly lower the gradient of the quadrupole field such that the axial confinement provided by the quadrupole coils will approximately match the confinement of the IP coils. Then, we rapidly turn off the quadrupole coils and turn on the IP coils in less than a millisecond. With the atoms trapped in the HIP trap, we perform the radio frequency (RF) evaporative cooling. By setting the depth of the final RF cut, we can control the temperature of the cloud that is sent down to the application chamber. In fact, we can cool the cloud to quantum degeneracy and make a BEC containing  $\sim 2 \times 10^5$  atoms. Unfortunately, the cloud heats significantly as we move the cloud to the atom chip, and we generally cool to only 1  $\mu$ K before transport to the chip so that the heating is not such a large effect.

For transferring the atoms to the application chamber, we extend the large permanent magnets from the HIP trap to the application chamber. Where the large permanent

magnets end, another smaller set of permanent magnets, inside the application chamber, extends to overlap the atom chip producing a gradient of 1600 G/cm (Figures 2.1 and 4.1). These two sets of magnets confine the atoms radially, making a macroscopic guide for the atoms as they move to the chip. To accelerate the atoms down this magnetic guide, we can slowly turn off the exit IP coils and ramp up the entrance IP coils. This was our first method for accelerating the atoms, but more recent methods turned out to be better. Transferring the atoms turned out to be a complicated process, and will be discussed in more detail in Chapter 4.

We use two different rare-earth materials for the two sets of permanent magnets. The large permanent magnets are made from neodymium iron boron. This material is chosen for its greater material strength and magnetic field strength when compared to samarium cobalt. We use samarium cobalt for the small permanent magnets. These magnets go inside the application chamber and need to be baked. Samarium cobalt has a high Curie temperature and can be baked to 250 C. However, we currently bake the small magnets only to 100 C, and at this temperature we could use neodymium iron boron. This may be a better choice because the small samarium cobalt magnets are very brittle and, therefore, extremely difficult to handle without breaking them.

### 2.5.1 Imaging in the HIP Trap

We use absorption imaging to characterize the atomic cloud in the HIP trap. By imaging the cloud, we can measure its optical density as a function of position, and this image gives us all the information we know about the atomic sample. While producing an image in the HIP trap is relatively easy, extracting quantitative information from the images is difficult because the non-uniform field from the permanent magnets cannot be shut off, which produces several systematic effects. Reference [66] demonstrates a rather complicated scheme for imaging in the HIP trap that eliminates these systematics, requiring microwave frequencies and a 100 G bias field. However, as we only require

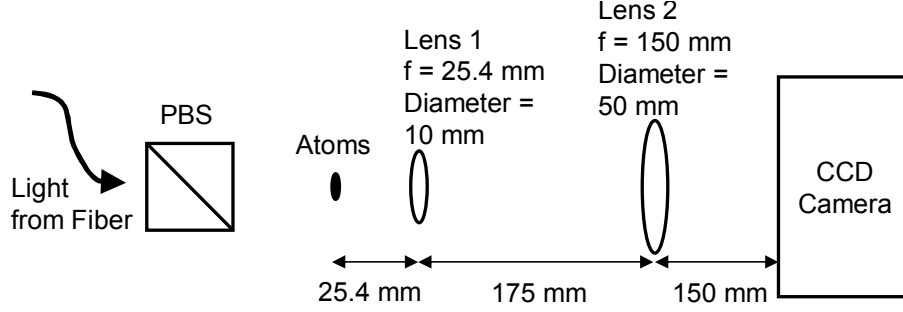


Figure 2.9: Schematic of the optics for absorption imaging. Lens 1 is a gradient singlet and Lens 2 is an achromatic doublet. The PBS is a polarizing beamsplitting cube.

absolute quantitative information on the 20% level in the evaporation chamber, we can utilize a much simpler imaging scheme that will give us accurate relative information.

The imaging optics are shown in Figure 2.9. Light from the probe laser is brought to the evaporation chamber via a single-mode fiber (see Section 2.2), and the beam is expanded to a diameter of 1 cm to evenly illuminate the 200- $\mu\text{m}$  sample of atoms. The light first passes through a polarizer and then illuminates the atoms inside the glass cell. The light passes through two lenses to focus the image of the atoms onto a CCD camera, magnifying the cloud by a factor of six. Our camera's CCD array is  $512 \times 512$  pixels with an individual pixel size of 24  $\mu\text{m}$ .

Before discussing the systematic effects of imaging in the HIP trap, let us discuss the usual imaging protocol for atoms in a trap where the field can be shut off, which we do use for imaging on the atom chip. First, the trap or guide is shut off and the atoms are allowed to expand. After a certain time of flight, an (approximately) uniform bias field is turned on in a direction parallel to the propagation of the probe beam. If the atoms are in the ( $F = 1$ ) ground state, they can be repumped to the ( $F = 2$ ) ground state by applying a laser resonant to the ( $F = 1$ )  $\rightarrow$  ( $F' = 2$ ) transition. The probe beam illuminates the atoms resonantly on the  $|F = 2, m_F = \pm 2\rangle \rightarrow |F' = 3, m_F = \pm 3\rangle$  transition with  $\sigma_{\pm}$  polarization. Exciting the atoms in this way, they cycle on this transition and rarely fall into a dark state where they no longer would absorb probe

light. The imaging pulse illuminates the atoms for 20–100  $\mu\text{s}$ . An image of the probe beam is recorded on a CCD camera such that the shadow of the atoms is focused onto the CCD array. The optical column density (OD) at a specific position in the cloud is determined by the amount of light absorbed by the atoms and is governed by Beer's law,

$$I = I_o e^{-OD} \quad (2.7)$$

where  $I$  is the intensity after the light has passed through the atoms and  $I_o$  is the initial intensity of the probe beam. Equation 2.7 is valid for  $I_o \ll I_s$ , where  $I_s$  is the saturation intensity of the atomic transition.

In practice, we use three images to measure the OD. First, we image the atoms as described above (Atom Frame). Next, we produce the same image except the atoms are not present (Light Frame). This image allows us to know the initial intensity,  $I_o$ . A final image is taken with the probe laser and the repump laser (if used) off so we can subtract ambient light and any other offsets that are not due to the imaging light and the atoms (Dark Frame). The OD as a function of position,  $OD(\vec{r})$ , is experimentally determined by

$$OD(\vec{r}) = \ln \left( \frac{I_{light} - I_{dark}}{I_{atom} - I_{dark}} \right) \quad (2.8)$$

By fitting a 2-D Gaussian to the image of the cloud, we can extract the root mean squared (rms) width of the cloud and the peak OD, the OD at the center of the cloud.  $OD(\vec{r})$  is related to the atomic distribution by

$$OD(\vec{r}) = \int n(\vec{r}') \sigma_o dz \quad (2.9)$$

where  $z$  is in the direction of the probe beam,  $\sigma_o$  is the on-resonant optical cross-section, and  $n(\vec{r}')$  is the density distribution of the cloud. By assuming that the cloud is in a harmonic trap and using the 2-D Gaussian fit, we can determine many useful physical quantities about the cloud. Reference [66] extends this discussion further to show the

calculations for these physical quantities and describes the effects of  $I_o$  close to  $I_s$  and of high density clouds that absorb almost all of the probe light during the imaging process.

Because the radial field of the HIP trap cannot be shut off, we have to image the atom in-trap. To image the axial and the radial size of the cloud, the probe beam must propagate in a direction perpendicular to the axial bias (quantization) field in the HIP trap. Thus, there is no available cycling transition because the probe beam cannot drive a purely  $\sigma_+$  or  $\sigma_-$  transition. To image the atoms in-trap, we linearly polarize the light parallel to the axial bias field and drive the  $|F = 1, m_F = -1\rangle \rightarrow |F' = 1, m_F = -1\rangle$  transition, scattering on average 1.7 photons per atom before the atoms fall into another ground state that is not resonant with the probe laser. Since the atoms fall dark so quickly, the optical depth we measure is never the true optical depth and has to be rescaled. Unfortunately, the scaling factor is dependent on the local density in the cloud, causing a systematic narrowing in the measured width of the cloud.

To determine the effect of the atoms falling into dark states during the imaging pulse, we must calculate how the OD changes as function of time. Since an atom can scatter only  $\alpha = 1.7$  photons, the number of atoms per unit area that can scatter photons,  $n_A$ , is a function of time during the imaging pulse,

$$\frac{dn_A(t)}{dt} = -\frac{\gamma}{\alpha}n_A(t) \quad (2.10)$$

where  $\gamma$  is the number of photons scattered per atom per unit time given by

$$\gamma = \frac{I_o \sigma_o}{h\nu} \left( \frac{1 - e^{-OD_o}}{OD_o} \right) \quad (2.11)$$

where  $\nu$  is the frequency of the incident photons and  $OD_o$  is the initial OD.  $OD_o$  is the quantity we need to calculate the physical properties of the cloud. By solving Equation 2.10 for  $n_A(t)$ , we can calculate  $OD(t)$ . To relate the OD that we measure,  $OD_{meas}$ , to  $OD_o$ , we need to integrate  $OD(t)$  for the duration of the imaging pulse,  $t_{pulse}$ ,

$$OD_{meas} = \int_0^{t_{pulse}} OD(t) dt \quad (2.12)$$

Performing this integral, we find

$$OD_{meas} = \frac{\alpha h \nu}{\sigma_o I_o t_{pulse}} \left[ \text{Li}_2 \left( (1 - e^{OD_o}) e^{-\frac{\sigma_o I_o t_{pulse}}{\alpha h \nu}} \right) - \text{Li}_2 (1 - e^{OD_o}) \right] \quad (2.13)$$

where  $\text{Li}_n(z) = \sum_{k=1}^{\infty} z^k / k^n$ . Whereas  $OD_o$  is a function of neither the imaging pulse duration nor probe intensity, Equation 2.13 does depend on the imaging pulse parameters making a fast evaluation of an image difficult. Additionally,  $OD_o$  varies throughout the cloud so there is no simple numerical factor relating  $OD_o$  to  $OD_{meas}$  for the whole cloud. Ideally, we would make the probe pulse intensity and duration as small as possible such that  $OD_o \approx OD_{meas}$ , but experimentally this is impractical since the signal-to-noise ratio in the image worsens as we do this. Thus, we try to adjust the probe-pulse intensity and duration such that we have an acceptable signal-to-noise ratio but there is only a small error in the measurement in the width of the cloud. Then, we approximate the distribution of the cloud with  $OD_o(\vec{r}) = \beta \cdot OD_{meas}(\vec{r})$ . For the conditions of  $I_o = 50 \mu\text{W}/\text{cm}^2$ ,  $t_{pulse} = 20 \mu\text{s}$ , and the peak  $OD_{meas} = 0.5$ ,  $\beta = 4$ , and the measured width is 10% too small. Equation 2.13 scales so that as the peak OD decreases,  $\beta$  increases but the error in the measured width decreases.

To avoid error in the measurement of the width, we try to image clouds with a low OD ( $< 0.5$ ), but often in-trap clouds have a  $OD_{peak} > 1$ , and they are too small to resolve. We use adiabatic rapid passage [73] to transfer the atoms to the  $|F = 1, m_F = 1\rangle$  state, which is untrapped, and the atoms spread rapidly in the anti-trapping potential. In 1–2 ms the atoms spread enough to allow good imaging on the  $|F = 1, m_F = 1\rangle \rightarrow |F' = 1, m_F = 1\rangle$  transition. However, if the atoms spread too much, the gradient from the permanent magnets will cause a spatially varying energy shift due to the Zeeman effect, such that the probe laser is not equally resonant across the entire cloud. This gives rise to another systematic narrowing of the cloud, but mainly in the radial direction, as the cloud expands much more quickly in the radial direction than in the axial direction. Therefore, we use the axial width to determine

the in-trap size and the temperature of the cloud.

Extracting exact numbers from images taken of atoms in the HIP trap is very tedious. Fortunately, for most experiments performed in the HIP, we do not need absolute numbers—we only require the OD and the size of the image change monotonically with the cloud, and the imaging system does do this.

## **2.6 Application Chamber**

The application chamber is a large chamber designed to house the atom-chip assembly while giving good optical access along the length of the chip. The stainless steel chamber was built to have two viewports with a viewable diameter of 7.5 cm as close to the atom chip as possible. We were able to set the viewports 8.8 cm away from the center of atom chip. With this configuration we can image atoms along the length of a 5-cm long chip. To allow for a certain amount of out-gassing from the atom chip assembly, we designed the chamber to have a large pumping speed. Thus, we pump through large diameter (10 cm) tubes for good conduction. The TSP inside the 10 cm tube provides most of the pumping speed (see Figure 2.2).

### **2.6.1 Atom-Chip Assembly**

The atom-chip assembly supports the atom chip, the bias sheet, and the small permanent magnets inside the application chamber. The bias sheet is two  $3 \times 1.6$  mm wires that run underneath the atom chip to provide a transverse bias field (Figure 2.10). The assembly is mounted on a single flange which contains twenty 5-A electrical feedthroughs to supply current to the atom chip and two 30-A current feedthroughs for the bias sheet. The atom chip, the bias sheet, and the small permanent magnets are mounted together on a copper block called the atom-chip holder. The alignment of the chip, the bias sheet, and the magnets is critical for loading the atoms onto the central waveguide of the chip, and the atom-chip holder is precisely machined to align these

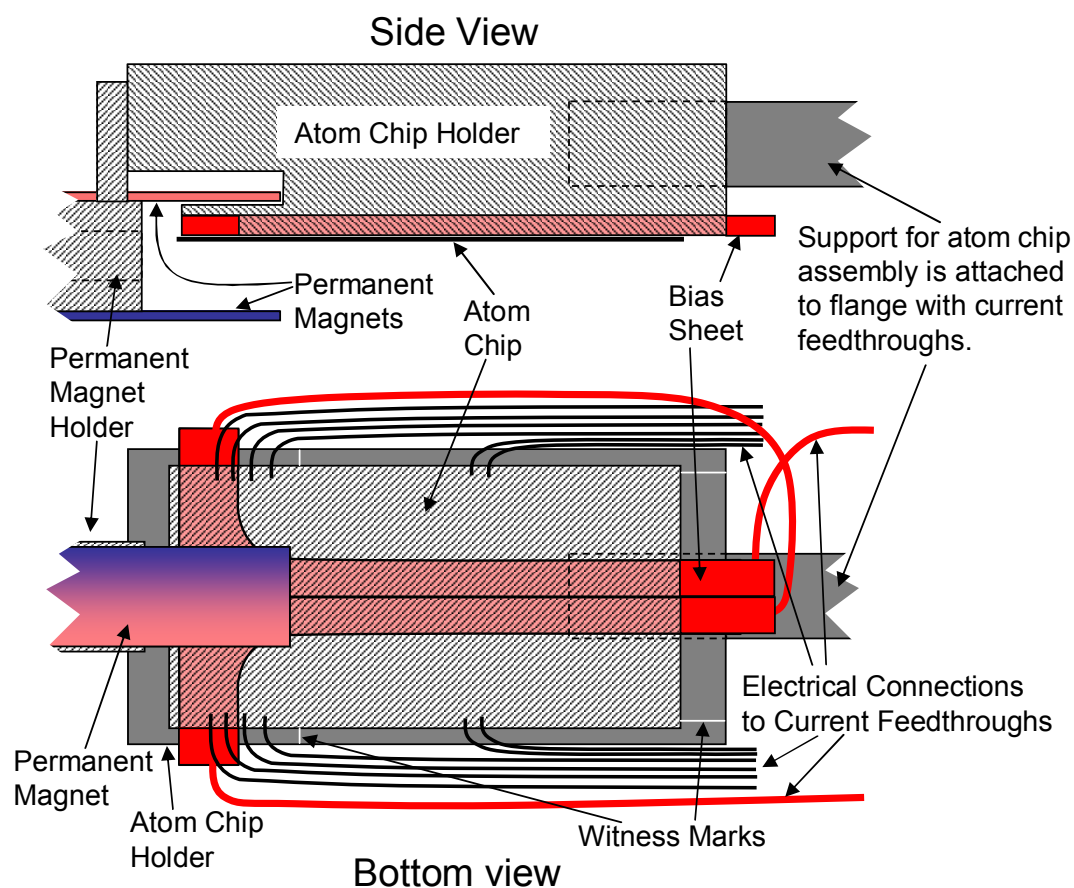


Figure 2.10: Schematic of the atom chip assembly showing both a side view and a bottom view. A 6 inch flange, with the current feedthroughs and a viewport welded onto it, supports the atom chip assembly. The bottom view shows the electrical connection for the bias sheet and a few of the wires connected to the atom chip.



components to better than 100  $\mu\text{m}$  accuracy. The atom-chip holder also conducts heat away from the chip and the bias sheet. The assembly is mounted upside down in the application chamber so that dust is less likely to settle on the chip's surface.

In constructing the atom chip assembly, care is taken to make sure the components are precisely aligned and to use materials compatible to a UHV environment. The magnet holder, atom-chip holder, and bias sheet are made out of oxygen-free (OF) copper with 99.99% purity, and the support for the assembly is made from 6061 aluminum. Both materials are UHV compatible. The magnet holder and atom-chip holder are aligned with pins and held together with a screw. All of the pins and screws used in the vacuum are made of a non-magnetic stainless steel and are vented down their centers to allow air to escape from the bottom of their holes. The bias sheet and atom chip are attached to the atom-chip holder with a UHV compatible glue, EpoTek 353ND. 353ND is good to  $10^{-11}$  torr and is bakeable to 200 C. We also use 353ND to glue the magnets to the magnet holder and to coat the magnets so they cannot outgas into the vacuum. Because both the bias sheet and the atom-chip holder are copper, they need to be electrically insulated so that current does not flow into the atom-chip holder. The two bias sheet wires also need to be insulated from each other. We use 25- $\mu\text{m}$  thick polyimide sheets for insulation. Polyimide, also known as Kapton or Vespel, withstands temperatures to 250 C and is good at  $10^{-11}$  torr. To align the atom chip to the atom-chip holder, we scratch precisely placed witness marks onto the surface of the atom-chip holder, and under a microscope align the witness marks to markers patterned onto the atom chip (see Figures 2.10 and 3.2).

We use 24 AWG wires to connect the conductors on the atom chip to the electrical feedthroughs. These wires are manufactured from electrolytic tough pitch (EPT) copper (99.9+% purity with  $\sim 200$  ppm oxygen) and are coated with a polyimide coating for insulation. The wires are attached to the chip with 5% silver/95% tin solder. A standard zinc/tin solder is not used because of the high vapor pressure of zinc. The wires are

attached to the electrical feedthrough with a copper beryllium crimp-solder connector. The wires that connect the bias sheet to the 30-A feedthroughs are cut from 1.6-mm-thick OF-copper sheet. They are bent into the correct shape, screwed to the bias sheet, and attached to the high current feedthroughs with barrel connectors.

## Chapter 3

### The Atom Chip

An atom chip can be used to make many different types of potentials for guiding and trapping atoms. To date, most atom chips use lithographically-patterned current-carrying wires to manipulate atoms with a magnetic field. However, other field producing structures can be created. For example, there is a proposal to use both electric and magnetic fields to manipulate atoms in a quantum-computing scheme [51]. It is also possible to place optical fibers onto the chip to make an optical cavity for high-efficiency detection of the atoms [52]. Atom-chip experiments seek to exploit the close proximity of the atoms to the field-producing elements to explore new regimes created by these potentials. With the atoms close to the current-carrying wires, the magnetic-field gradients and curvatures the atoms experience can be extremely high. A strong 2-D potential also allows atoms to be guided, and two guides may be brought together to make a waveguide beamsplitter analogous to a fiber optical beamsplitter. The atom waveguide beamsplitter is an enabling technology for a guided atom interferometer, and the prospect of a guided atom interferometer is our impetus for researching atom-chip technology.

This chapter describes the basic design of our atom chip used throughout most of this thesis. I discuss how a magnetic guide is created on an atom chip, where I focus on one guiding scheme, the “bias-field guide”, and how the atoms are imaged once they are in the guide. We also describe how the atoms are coupled onto the atom chip as

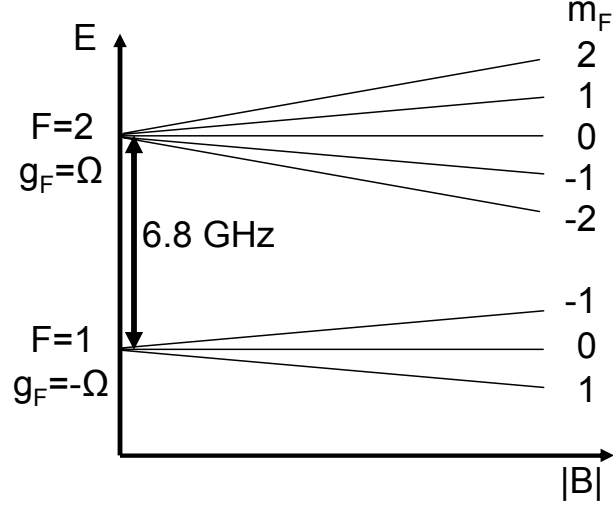


Figure 3.1: Schematic plot of the energy of the magnetic sublevels under the influence of a small magnetic field. The linear Zeeman effect splits the degeneracy of the magnetic sublevels of the  $5S^{1/2}$  ground states,  $F = 1$  and  $F = 2$ . The magnetically trappable Zeeman states or weak-field seeking state are  $F = 1, m_F = -1$  and  $F = 2, m_F = 1, 2$ .

they travel from the HIP trap down the permanent magnetic guide and into the central waveguide on the atom chip.

### 3.1 Magnetic Guiding

A neutral atom in a small magnetic field experiences a linear Zeeman potential

$$V = -\boldsymbol{\mu} \cdot \mathbf{B} \quad (3.1)$$

where  $\mu$  is the magnetic moment of the atom. If the atom moves adiabatically through the magnetic field, the potential can be written as

$$V = \mu_B g_F m_F |\mathbf{B}| \quad (3.2)$$

where  $\mu_B$  is the Bohr magneton,  $g_F$  is the Lande  $g$ -factor, and  $m_F$  is the magnetic quantum number. Whether an atom is attracted to a magnetic minimum (a weak-field seeker) or repelled by a magnetic minimum (a strong-field seeker) depends on the internal state of the atom. Figure 3.1 shows how the degeneracy of the magnetic

sublevels in the  $F = 1$  and  $F = 2$  ground states of the  $^{87}\text{Rb}$  is broken in the presence of a small magnetic field. For our magnetic trapping and guiding experiments, we use atoms in the  $|F = 1, m_F = -1\rangle$  weak-field seeking state.

To guide the atoms, we superpose the magnetic field from a current-carrying wire with a transverse bias field  $B_t$ , making a 2-D guiding potential with no longitudinal confinement [47, 74]. To calculate the field of this “bias-field guide,” we need the field from a infinitely thin wire carrying a current  $I$ ,

$$B = \frac{\mu_o I}{2\pi r} \quad (3.3)$$

where  $\mu_o$  is the permeability of free space, and  $r$  is the distance from the wire. The distance  $d$  at which  $B_t$  cancels the field from the wire to form the magnetic minimum is

$$d = \frac{\mu_o I}{2\pi B_t} \quad (3.4)$$

(see Figure 3.2 (a)), and the gradient  $B'$  at that distance is

$$|B'| = \frac{\mu_o I}{2\pi d^2} \quad (3.5)$$

The field surrounding the magnetic zero forms a 2-D quadrupole. To complete the magnetic guide, we apply a longitudinal bias field  $B_{\parallel}$ , parallel to the wire, to set the field at the guide center, to adjust the transverse guide frequency, and to prevent nonadiabatic spin flips [75, 76] at the center of the guide where the radial fields go to zero. The application of  $B_{\parallel}$  makes the guide harmonic, and the transverse frequency of the guide is given by

$$\nu = \frac{1}{2\pi} \sqrt{\frac{\mu_B g_F m_F}{m_{Rb}}} \frac{2\pi B_t^2}{\mu_o I \sqrt{B_{\parallel}}} \quad (3.6)$$

where  $m_{Rb}$  is the mass of  $^{87}\text{Rb}$ . Typical parameters for our bias field guide are  $B_t = 20$  G,  $I = 1$  A, and  $B_{\parallel} = 3$  G. This gives  $d = 100 \mu\text{m}$ ,  $B' = 2000$  G/cm, and  $\nu = 1.04$  kHz.

To create  $B_t$ , we use the bias sheet, two  $1.6 \times 3$  mm, high-current wires running along the back side of the atom chip. We model the bias sheet as a single infinitely thin

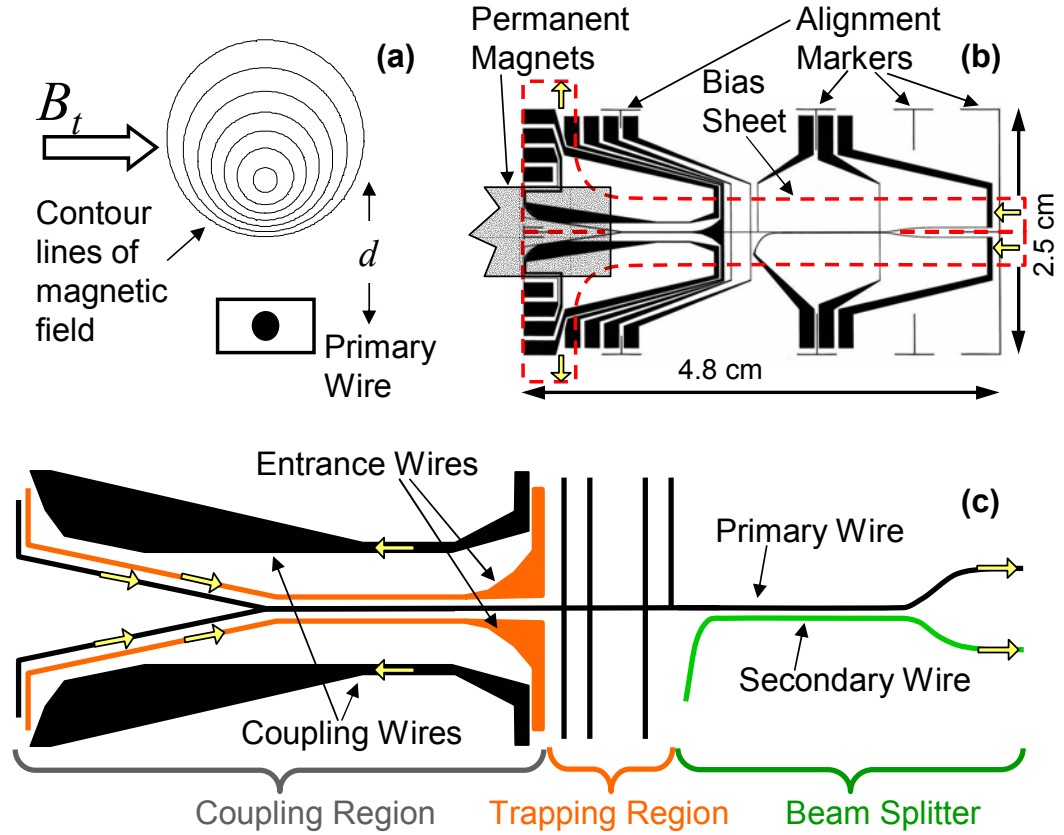


Figure 3.2: (a) The “bias-field guide.” The transverse bias field,  $B_t$ , from the bias sheet cancels the field from the wire at a distance  $d$  from the wire. (b) The conductor pattern on the atom chip (to scale). The small permanent magnets overlap the chip by 9 mm. The dotted line shows the outline of the bias sheet. The arrows indicate the direction of the current in the bias sheet. The alignment markers are used to align the chip to the atom chip holder’s witness marks (Figure 2.10). (c) The central region of the atom chip is expanded to show the general shape of the wires (not to scale). The atoms move from left to right along the primary wire.

current sheet with a width of  $a = 6$  mm. The field is given by

$$\mathbf{B}_t = \frac{\mu_o 2I_{sheet}}{2\pi a} \left[ \left( \arctan\left(\frac{z}{y + \frac{a}{2}}\right) - \arctan\left(\frac{z}{y - \frac{a}{2}}\right) \right) \hat{y} + \frac{1}{2} \ln\left(\frac{(y + \frac{a}{2})^2 + z^2}{(y - \frac{a}{2})^2 + z^2}\right) \hat{z} \right] \quad (3.7)$$

where  $I_{sheet}$  is the current of a single bias sheet wire. The sheet lies in the  $xy$ -plane with the current running the  $-x$ -direction. The guiding wire is offset 1.4 mm below the sheet in the  $z$ -direction, and the current runs in the  $x$ -direction. With  $I_{sheet} = 13.49$  A,  $\mathbf{B}_t = \hat{y}20$  G.

### 3.2 The Chip

Our atom chip contains three main regions: a coupling region, a trapping region, and a beamsplitting region (see Figure 3.2 (c)). The design of these three regions is largely determined by the type of waveguide that we use, the bias-field guide. We chose this guiding scheme because a beamsplitter is easily made by bringing two of these guides close together. Experiments performed with our atom waveguide beamsplitter in the beamsplitter region will be discussed in Chapter 6. The coupling region of the chip is where the atoms transition from the small permanent magnets onto the atom chip and into the central waveguide. In Section 3.4, I discuss the coupling scheme we developed that allows for a misalignment between the small permanent magnets and the central waveguide. In the trapping region wires intersect the primary guiding wire. A current through these wires creates a trapping potential by adding curvature to  $B_{||}$  [49, 77]. Chapter 5 shows how we can trap atoms using these wires and then use RF evaporation to make a BEC.

Our atom chips are fabricated in the group of Victor Bright in the Department of Mechanical Engineering here at the University of Colorado. They use a process of photolithography and electro-plating to create precisely patterned copper wires (Figure 3.3). They start with a circular aluminum nitride (AlN) substrate 7.62 cm in diameter,

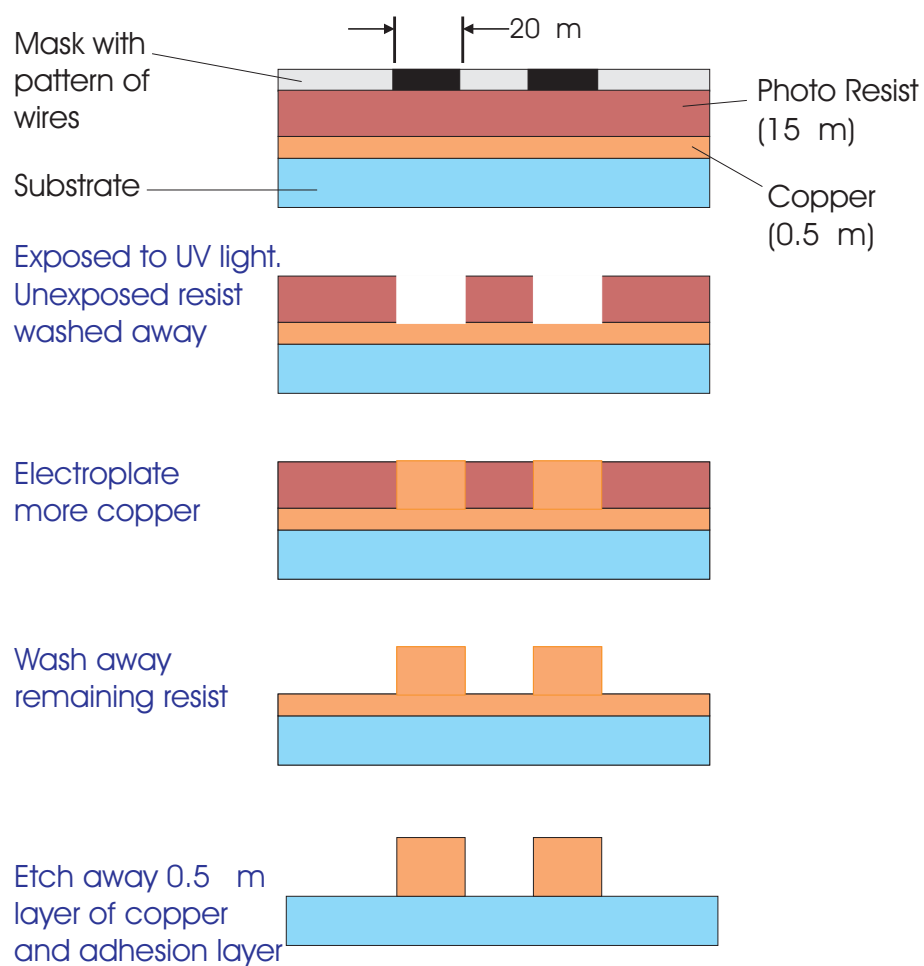


Figure 3.3: The steps for fabricating the atom chip. A titanium tungsten adhesion layer (not shown) lies between the copper and the AlN substrate.



commercially coated with a 50-nm thick titanium tungsten adhesion layer and a 0.5- $\mu\text{m}$  seed-layer of copper. We use AlN as a substrate material because of its relatively high thermal conductivity and its ease of handling. Reference [78] gives a table of the physical properties of various substrate materials for making atom chips. A 10-20- $\mu\text{m}$  layer of photoresist is spun onto the substrate. A mask is placed over the substrate, and the photoresist is exposed to UV light. Once the photoresist is cured, the unexposed photoresist is washed away where the wires are to be electro-plated. The substrate is then placed in an electro-plating solution, and a current is passed through the solution to deposit copper onto the exposed copper on the chip. The copper is deposited to a thickness of 8-14  $\mu\text{m}$ . With the electro-plating completed, the rest of the photoresist is washed from the substrate. Finally, the 0.5- $\mu\text{m}$  layer of copper and the titanium tungsten adhesion layer are removed from the entire surface leaving the desired pattern of wires.

This fabrication process gives wires that are  $\sim 10\text{-}\mu\text{m}$  thick and of almost arbitrary width. The resolution of photolithography is  $< 1\text{ }\mu\text{m}$ , but when electroplating to a 10- $\mu\text{m}$  thickness, small structures can grow together, limiting the smallest sized structure to  $\sim 10\text{ }\mu\text{m}$ . On the atom chip described in this thesis, most of the guiding wires are 20  $\mu\text{m}$  wide.

### 3.3 Imaging on the Atom Chip

Imaging on the atom chip can be done on the  $(2 \rightarrow 3')$  cycling transition since all of the confining magnetic fields are produced electromagnetically and can be rapidly switched off. We employ the imaging procedure described in Section 2.5.1 that uses light tuned to the  $(2 \rightarrow 3')$  transition. The only difficulty of imaging atoms on the atom chip is imaging near the surface of the chip, where two problems arise. The probe beam for the absorption imaging develops high-contrast fringes from diffracting off the two edges of the atom chip. Also, if the atoms are suddenly released out of a trap or guide

and allowed to expand, the cloud can expand faster than it falls under the influence of gravity, and half of the cloud will be deposited onto the surface of the chip. A cloud must be below 5  $\mu\text{K}$  for this effect to be small. To alleviate these problems, we can easily push the atoms away from the chip before imaging. To do this, we rapidly shut off the transverse bias field so that the atoms feel the large gradient from the wire. The wire accelerates the atoms away from the chip, and when the atoms are  $> 0.25$  mm away from the chip, the fringes do not affect the image. With this method we can easily image clouds with temperatures  $> 50$   $\mu\text{K}$ .

To image the axial and radial (vertical) dimensions of the cloud, we direct the probe beam such that it propagates perpendicular to the primary wire across the chip. Before the image is taken, we repump the atoms to the  $F = 2$  ground state, and turn on the bias sheet to provide a magnetic field parallel to the probe beam. The probe beam illuminates the atoms resonantly on the  $|F = 2, m_F = -2\rangle \rightarrow |F = 3, m_F = -3\rangle$  transition. The timing of the imaging process is shown in Figure 3.4(a).

Using the guide wire to push the atoms away from the chip creates another imaging problem: difficulty in accurately determining the temperature of the atoms in the guide. Usually, the temperature is determined by measuring the momentum distribution of the cloud by allowing it to freely expand after a rapid shut off of the guiding fields. By measuring the radial rms size of the cloud after a certain expansion time,  $\sigma_r(t_{\text{expand}})$ , we can calculate the temperature with the equation

$$T = \frac{m_{Rb}(\omega_r \sigma_r(0))^2}{k_b} \quad (3.8)$$

where  $\omega_r$  is the radial frequency of the guide.  $\sigma_r(0)$  is the in-trap size of the cloud (the size at  $t = 0$ ), which is given by

$$\sigma_r(0) = \frac{\sigma_r(t_{\text{expand}})}{\sqrt{1 + (\omega_r t_{\text{expand}})^2}} \quad (3.9)$$

However, determination of the temperature becomes difficult when one is using the

pushing method because the guide wire not only pushes the atoms but also slows the expansion of the cloud due to the curvature of its field  $B'' = \frac{\mu_o I}{\pi r^3}$ .

To accurately determine the temperature of the atomic sample, we need to relate the measured size of the cloud,  $\sigma_r(t_{expand})$ , to the in-trap size of the cloud,  $\sigma_r(0)$ . Through a numerical model of the expansion process, we can do this. The model calculates the trajectories of single atoms as the bias sheet and the guiding wire are turned off. Each atom is given some initial potential and kinetic energy in the guide such that each atom starts with the same total energy, the mean energy of the atoms in the guide. Then we calculate the trajectory of the atoms in the vertical direction by solving the differential equation

$$\frac{d^2z}{dt^2} = \frac{-1}{m_{Rb}} \frac{\partial V(z, t)}{\partial z} - g \quad (3.10)$$

where  $g$  is the acceleration due to gravity and  $V(z, t)$ , given by equation 3.2, is the potential the atoms experience due to the time dependent magnetic field. By tracing 16 trajectories, we can accurately determine the rms size of the cloud. The outermost trajectory at a given time determines  $\sigma_r(t)$ , and as the expansion progresses, the outermost trajectory changes (see Figure 3.4 (e)). In a free expansion, at  $t_{expand} = 0$ , the outermost trajectory is the atom with only potential energy as its initial condition, and then, as the cloud expands, the outermost trajectory is asymptotically the atom with only kinetic energy as its initial condition. However, when the atoms are pushed by the wire, the atom with the outermost trajectory for large  $t_{expand}$  will have not only kinetic energy as its initial condition. A different atom starting with a combination of potential and kinetic energy will asymptotically be the outermost. The curvature of the field from the wire causes these mean atomic trajectories to oscillate about the center of the cloud during the expansion. Figure 3.4(b)-(e) shows the results of a calculation where the wire pushes the atoms away for differing lengths of time,  $t_{push}$ . Figure 3.4(d) shows that the size of a cloud pushed for  $t_{push} = 0.5$  ms is linearly proportional to the

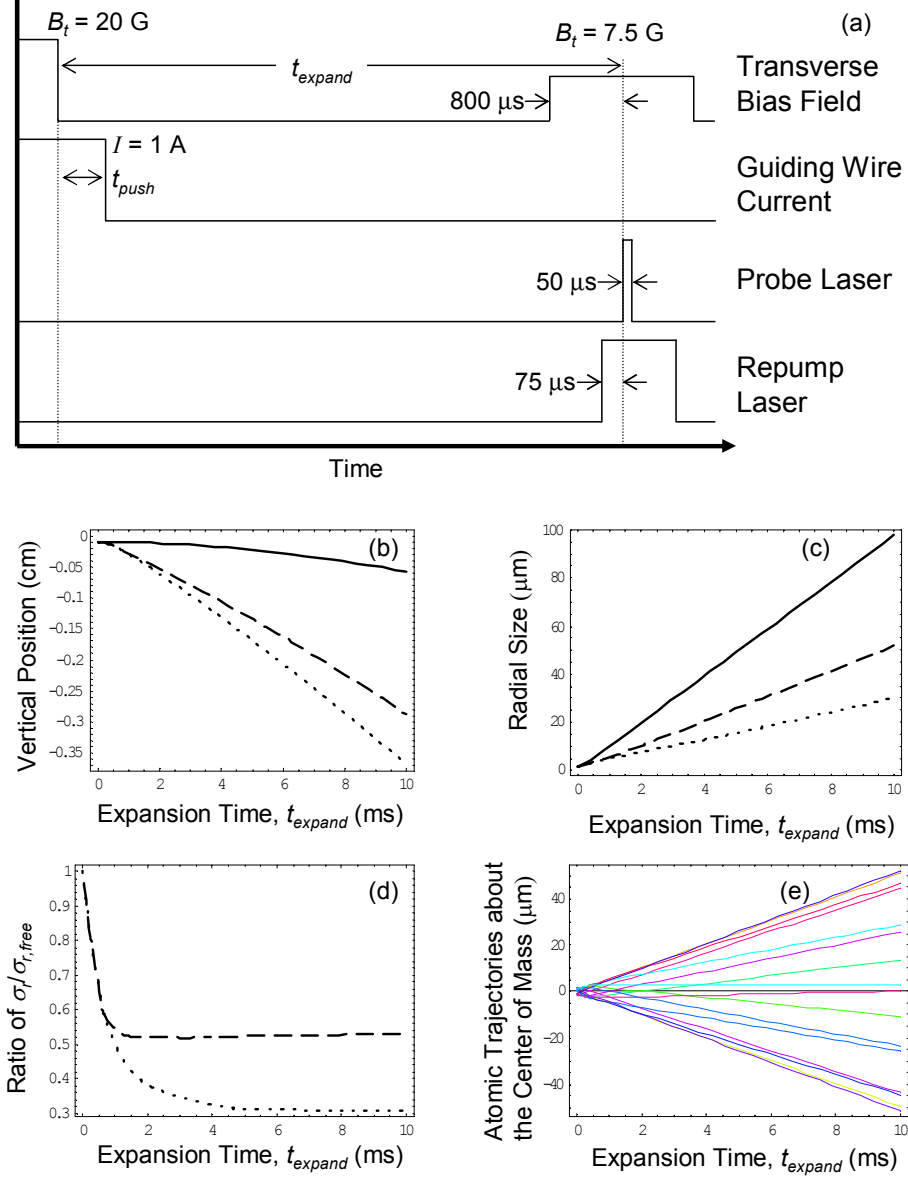


Figure 3.4: (a) Timing diagram for imaging (not to scale). (b)-(d) Plots of the expansion of a  $1 \mu\text{K}$  cloud with  $I = 1$  A,  $B_t = 20$  G, and  $B_{\parallel} = 3$  G. The solid line shows a free expansion,  $t_{\text{push}} = 0$  ms. The dashed line is for  $t_{\text{push}} = 0.5$  ms. The dotted line is for  $t_{\text{push}} = t_{\text{expand}}$ . (b) A plot of the center of mass of the cloud as it falls away from the chip. (c) The plot shows the size of the cloud as it expands. (d) The plot shows the ratio of the size of a cloud pushed for  $t_{\text{push}} = 0.5$  ms to the size of a cloud that expanded freely (dashed line), and the ratio of the size of a cloud pushed for  $t_{\text{push}} = t_{\text{expand}}$  to a cloud that expanded freely (dotted line). Note that a shorter push causes the cloud to expand proportionally to the free expanded cloud after the wire is turned off. (e)  $t_{\text{push}} = 0.5$  ms. A plot of the position of the trajectories with the mean energy of the cloud minus the center of mass position. Until the wire is turned off, the trajectories of the atoms oscillate about the center of mass position. After the wire is turned off, the atoms expand freely, and the outer most trajectory determines the size of the cloud.

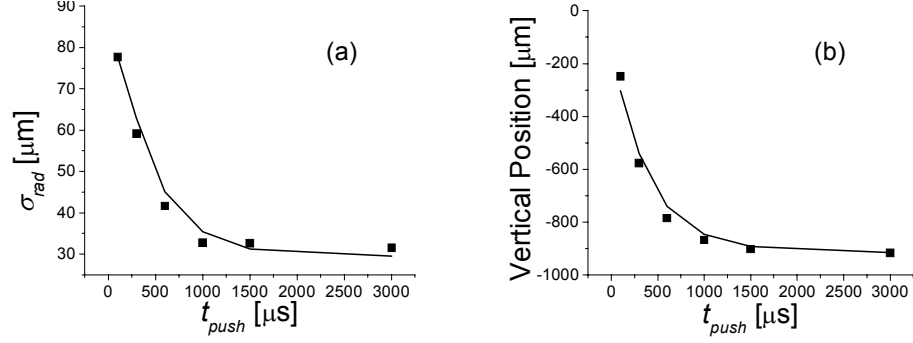


Figure 3.5: The plots show the radial size (a) and the vertical position (b) of the atoms as a function of how long the guide wire remains on after the bias sheet is turned off,  $t_{push}$ . The expansion time is fixed at  $t_{expand} = 3$  ms. The points are measured experimentally and the line is the numerical simulation. In Figure (a) the numerical simulation has been multiplied by a constant scaling factor to fit the temperature, and in Figure (b) a certain distance has been subtracted from the measured data to put the surface of the substrate at zero. The experimental conditions are:  $B_t = 23$  G,  $I = 1$  A, and  $B_{\parallel} \approx 3$  G.

size of a freely expanded cloud after 2 ms of expansion. This constant factor,  $k_{expand}$ , between the size of the freely expanded cloud and the pushed cloud, can be used to determine the in-trap size of the cloud,

$$\sigma_r(0) = \frac{\sigma_r(t_{expand})}{k_{expand} \sqrt{1 + (\omega_r t_{expand})^2}} \quad (3.11)$$

where the expansion factor,  $k_{expand}$ , depends neither on  $t_{expand}$  nor the temperature of the cloud. In practice, we measure the currents for the guide wire and the bias sheet, the guide's radial frequency, and  $t_{push}$ , and then we use the numerical model to calculate the expansion factor,  $k_{expand}$ . Once we know  $k_{expand}$ , we can easily calculate the temperature of the atoms in the guide.

To check the results of the numerical simulation, we compared it with the experiment by allowing the atoms to expand for 3 ms while varying  $t_{push}$  (Figure 3.5). While the results agree qualitatively, there is as much as  $\sim 10\%$  error on both the vertical position and the radial size. This error is reduced with a more accurate determination of the experimental parameters, mainly  $B_t$  and  $B_{\parallel}$ .

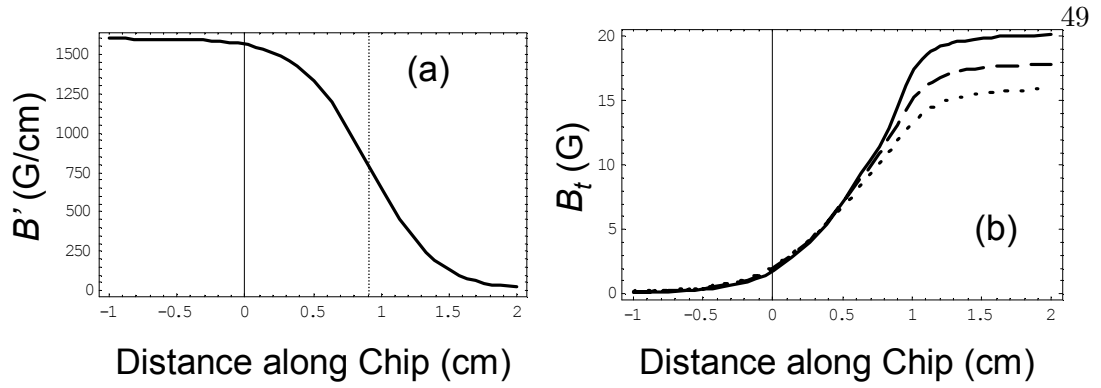


Figure 3.6: Figure (a) shows the estimated magnetic field gradient produced by the small permanent magnets as a function of distance along the chip. The vertical solid line shows the edge of the atom chip, and the vertical dotted line shows the end of the permanent magnets. Figure (b) shows the estimated transverse bias field for three different distances below the chip. The solid line is 0.5 mm below, the dashed line is 1.0 mm below, and the 1.5 mm below.

### 3.4 The Coupling Region

As the atoms move from the evaporation chamber to the atom chip, the atoms travel down the magnetic guide created by the permanent magnets. As the atoms leave the small permanent magnets, they need to move into the bias-field guide created by the field from the primary wire and the bias sheet. We want this transition to occur adiabatically, and the atoms should be able to follow a single magnetic minimum from the magnets to the waveguide. For simplicity, we do not want to ramp any currents during the transition. We also need to allow for a certain misalignment between the permanent magnets' minimum and the waveguide,  $\pm 500 \mu\text{m}$  in the two radial dimensions.

The conductors in the coupling region of the chip allow us to accomplish the above goals. As the atoms move away from the small permanent magnets, the magnets' 1600 G/cm gradient decays to zero over a distance of  $\sim 1$  cm (Figure 3.6 (a)). Typically, each bias sheet wire carries 15 A to provide a transverse bias field,  $B_t$ , of 23 G, and the current exits the bias sheet symmetrically out both sides of the T in the bias sheet at the beginning of the atom chip (Figure 3.2(b)). Thus, the transverse bias field increases as

the atoms move past the T of the bias sheet (Figure 3.6 (b)). The quadrupole field of the magnets and the transverse bias field are oriented such that magnetic minimum of the permanent magnets moves up toward the chip as the gradient of the magnets weakens and  $B_t$  strengthens. With the permanent magnets and the atom chip aligned properly, the magnetic minimum moves toward the primary guiding wire on the chip, and primary wire “captures” the magnetic minimum coupling the atoms into the waveguide. The loading of atoms into the waveguide is shown in Figure 3.7 (c).

If the primary wire and the permanent magnets are not well aligned, the primary wire will not capture the minimum, and the atoms will crash into the substrate. The atom chip assembly aligns the physical position of the permanent magnets relative to the atom chip to a tolerance of  $\pm 50 \mu\text{m}$ , but we were uncertain how well the magnetic minimum of the permanent magnets is aligned with the geometric location of the magnets. To increase the “capture range” of the primary wire, we add extra wires in the coupling region (Figure 3.2(c)). The “coupling wires” act to repel the minimum from the permanent magnets and push it towards the primary wire. The coupling wires carry a current of 5 A each in the opposite direction of the primary wire current, and they are spaced 1 mm away from the primary wire. Their width at the narrowest point is  $100 \mu\text{m}$ . The entrance wires run close to the primary wire in the coupling region, separated from the primary wire by  $40 \mu\text{m}$  (center to center). With a 0.5–1 A current running in the same direction as the primary wire, the entrance wires add to the field created by the primary wire, again increasing the capture range. With these extra wires the capture range is  $\pm 500 \mu\text{m}$  in the horizontal direction. In the vertical direction the magnetic minimum from the permanent magnets can be offset 0.5–2.0 mm below the primary wire (see Figure 3.7). We designed the offset to be 1.15 mm. When loading the atom chip in practice, we are able to couple the atoms in the primary waveguide with only 1 A in the primary wire. Thus far, with three different atom chips, we have not needed the other wires in the coupling region. This means that the magnetic minimum

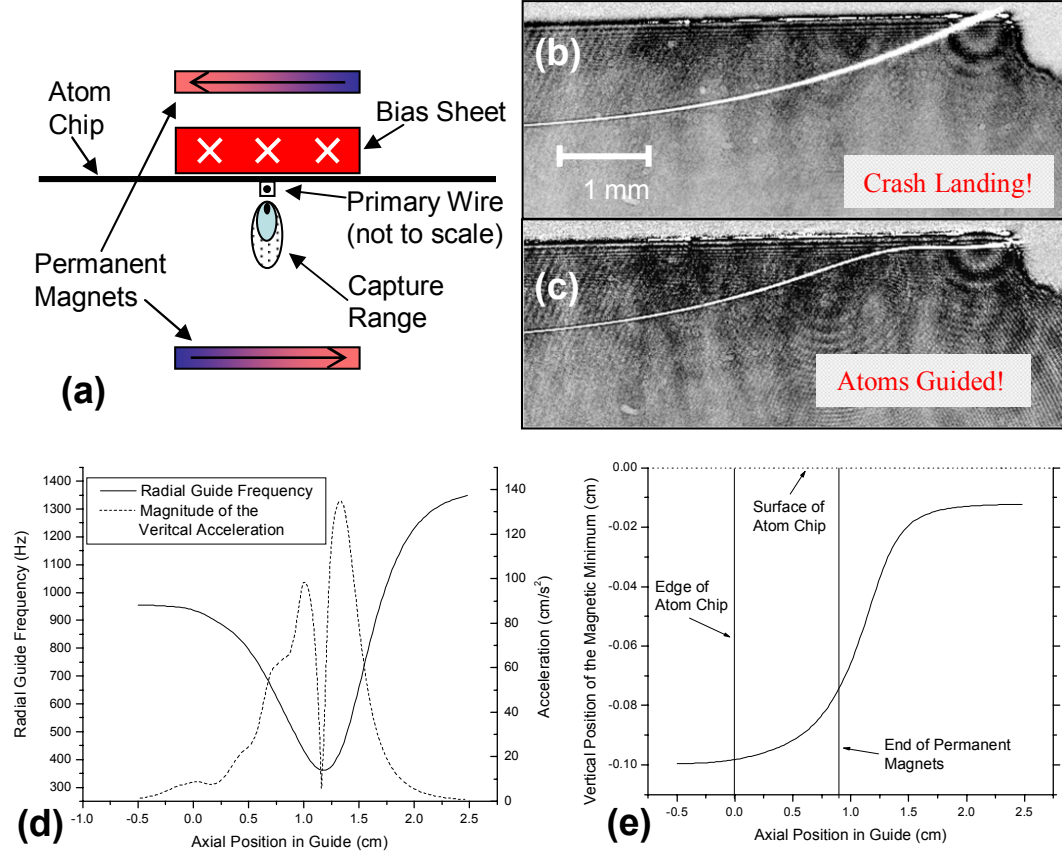


Figure 3.7: (a) Cross section of the atom chip assembly (to scale). The capture range is depicted for three conditions by the three ellipses. The conditions are (from smallest to largest):  $I_{\text{primary}} = 0.5$  A,  $I_{\text{primary}} = I_{\text{entrance}} = 0.5$  A, and  $I_{\text{primary}} = I_{\text{entrance}} = 0.5$  A  $I_{\text{coupling}} = 5$  A. See Figure 3.2 (c) for the wire configuration. (b) This image shows the transverse bias field ( $B_t = 23$  G) bringing the magnetic minimum up to the chip. None of the wires in the coupling region are on so the atoms crash into the chip. (c) In this image  $I_{\text{primary}} = I_{\text{entrance}} = 0.5$  A and  $I_{\text{coupling}} = 5$  A. The atoms are “captured” in the waveguide. (d) Plot of the transverse guide frequency and vertical acceleration vs. axial position in the guide. The vertical acceleration is calculated for atoms moving at 20 cm/s longitudinally. (e) The calculated vertical position of the magnetic minimum versus the axial position.



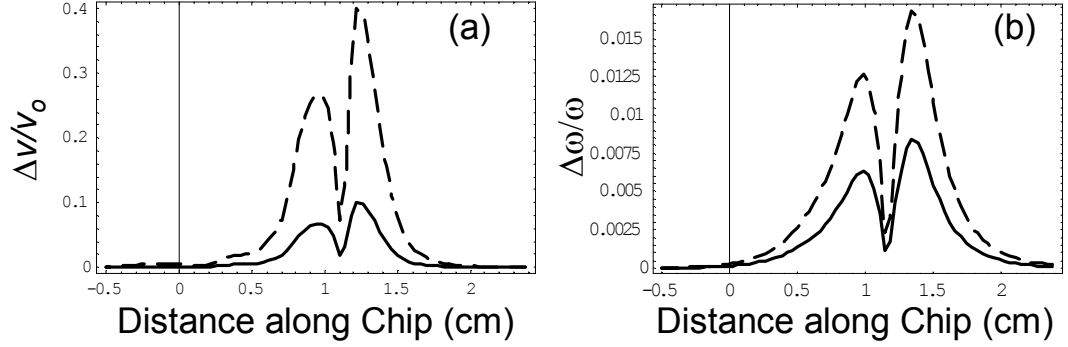


Figure 3.8: These plots show the calculated adiabatic parameters as the atoms move onto the chip. The solid line is for atoms moving with a longitudinal velocity of 10 cm/s, and the dashed line is for atoms moving at 20 cm/s. In this calculation  $I_{primary} = I_{entrance} = 0.5$  A and  $I_{coupling} = 5$  A Plot (a) shows the adiabaticity of the transverse movement of the center of the guide, and Plot (b) shows the adiabaticity of the change in radial confinement.

of the magnets is well centered below the primary wire within a tolerance of  $\pm 100$   $\mu\text{m}$ .

Figure 3.7(d) shows the calculated guide frequency and transverse acceleration as a function of the longitudinal position. Unfortunately, the trap frequency is near a minimum during the largest acceleration. To avoid heating during the acceleration and decompression, we must maintain a slow enough velocity to make sure the transition to the chip is adiabatic. To characterize the adiabaticity of the transition, we define two adiabatic parameters. First, we want the change in angular frequency,  $\Delta\omega$ , in one angular period,  $\Delta t = 1/\omega$ , to be small compared to the angular frequency,  $\omega$ , or

$$\frac{\Delta\omega}{\omega} \ll 1 \text{ in a time, } \Delta t \quad (3.12)$$

for the change in frequency to be adiabatic. We can also write this as

$$\frac{\Delta\omega}{\omega} \frac{1}{\Delta t\omega} \Rightarrow \frac{d\omega}{dt} \frac{1}{\omega^2} \ll 1 \quad (3.13)$$

where  $\Delta t\omega = 1$ . Second, the change in the center-of-mass transverse velocity of the atoms as they move onto the chip,  $\Delta v$ , in one angular period,  $\Delta t$ , needs to be small compared to the rms velocity of the ground state of the guide,  $v_o = \sqrt{\hbar\omega/m_{Rb}}$ . This

gives the adiabatic condition for the movement of the center of the guide to be

$$\frac{\Delta v}{v_o} \frac{1}{\Delta t \omega} \Rightarrow \frac{dv}{dt} \frac{1}{v_o \omega} = \frac{a_t}{v_o \omega} \ll 1 \quad (3.14)$$

where  $a_t$  is the transverse acceleration of the atoms as they move down the guide. This condition is overly strict for a constant acceleration, but with the acceleration constantly changing as the atoms move onto the chip, we believe that Equation 3.14 is a reasonable condition. Figure 3.8 shows that the radial frequency of the guide changes slow enough for atoms moving at both 10 and 20 cm/s, but the transverse acceleration is on the edge of adiabaticity. Atoms moving at 20 cm/s are likely moving too fast, and atoms moving at 10 cm/s might not heat as they are loaded. The adiabaticity of the end of the coupling region where the entrance wires split away from the primary wire needs to be evaluated as well. A velocity of 10 cm/s is also necessary for no heating during this transition. A 10 cm/s velocity is a difficult velocity for the atoms to reach due to problems that will be discussed in Chapter 4.

The wires in the coupling region start widely separated and taper in symmetrically over a length of a 1–1.5 cm. This geometry prevents a number of problems. We apply a 3 G longitudinal bias field to prevent nonadiabatic spin flips in the guide. Currents that flow perpendicular to the longitudinal field create a field that adds to this field. If the field from a wire is too strong, it can cancel the longitudinal field and the atoms will be lost from the guide, or the fields can add, creating a potential bump in the guide that is larger than the atoms' kinetic energy causing the atoms to reflect. To avoid this problem, we bring the currents in symmetrically at the beginning of the chip. The fields from these opposite currents cancel along the symmetry axis of the primary wire. This solves the problem if the atoms are perfectly centered over the chip, but the guide may be offset horizontally due to the permanent magnets, and therefore, a longitudinal field from the currents still exists. Thus, in the first 1.5 cm of the chip the wires are tapered to minimize the longitudinal field from the currents (Figure 3.9). The

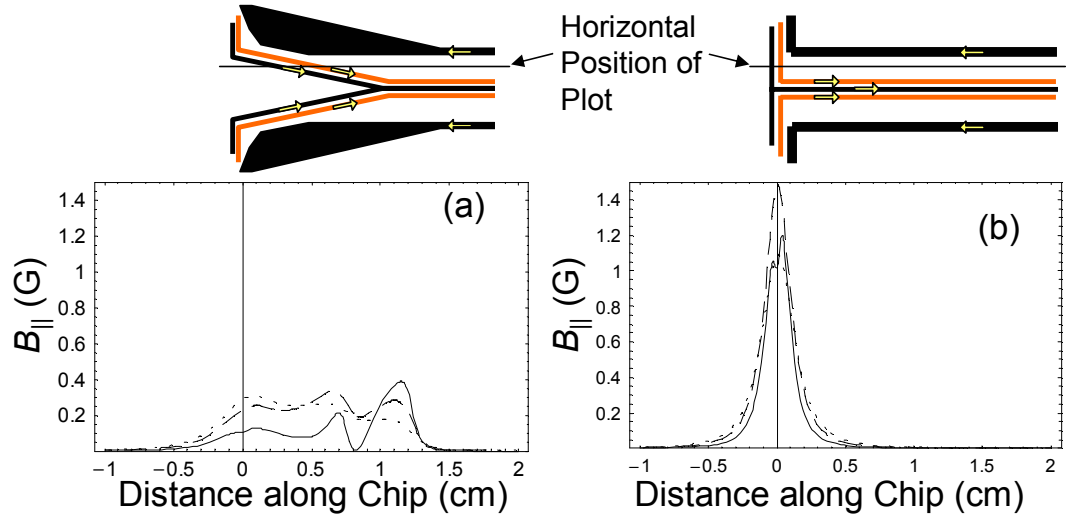


Figure 3.9: Longitudinal magnetic field produced by the wires in the coupling region. The plots show the longitudinal magnetic field along a line displaced  $500 \mu\text{m}$  off center horizontally from the primary wire and  $0.5 \text{ mm}$  (solid line),  $1.0 \text{ mm}$  (dashed line), or  $1.5 \text{ mm}$  below the chip's surface. Depending on which side of the primary wire the field is plotted, the longitudinal field is positive or negative. The currents in the wires are  $I_{\text{primary}} = I_{\text{entrance}} = 0.5 \text{ A}$  and  $I_{\text{coupling}} = 5$ . Plot (a) shows the field from the tapered coupling region used on our atom chip. Plot (b) shows the field from a T-shaped coupling region.

maximum longitudinal field from the coupling region and the T in the longitudinal bias sheet combined is calculated to be 0.8 G on the edge of the horizontal capture range ( $\pm 500 \mu\text{m}$ ), sufficiently small for our typical center of mass speeds of 10–30 cm/s.

## Chapter 4

### Transferring the Atoms to the Atom Chip

In transferring the atoms from the evaporation chamber to the application chamber and onto the atom chip, we have several goals: (1) We need high efficiency-transfer with very little atom loss. (2) The velocity of the atoms needs to be easily controlled, as experiments we are planning on the atom chip can have a large velocity dependence. (3) The longitudinal expansion of the cloud needs to be controlled as well. If the cloud spreads too much, the signal-to-noise ratio in the image will be reduced. (4) The transfer process needs to be adiabatic such that if we launch a BEC toward the atom chip, the BEC should propagate in the lowest mode of the guide.

#### 4.1 The Permanent Magnets

Unfortunately, these goals, except for high transfer efficiency, are not easily achieved with our system. This is mainly due to imperfections in the permanent magnets. As described in Section 2.5, we use a large and a small set of permanent magnets to radially confine the atoms as they are moved from the evaporation chamber to the application chamber. If the magnets were perfect, they would produce only a strong radial gradient while producing no longitudinal field. However, they do produce a spatially changing longitudinal field, rather large in magnitude, gradient, and curvature. In practice, the large permanent magnets are a set of four magnets, and the small permanent magnets are a set of six magnets (Figure 4.1(a) and (b)). Figure 4.1(c) shows

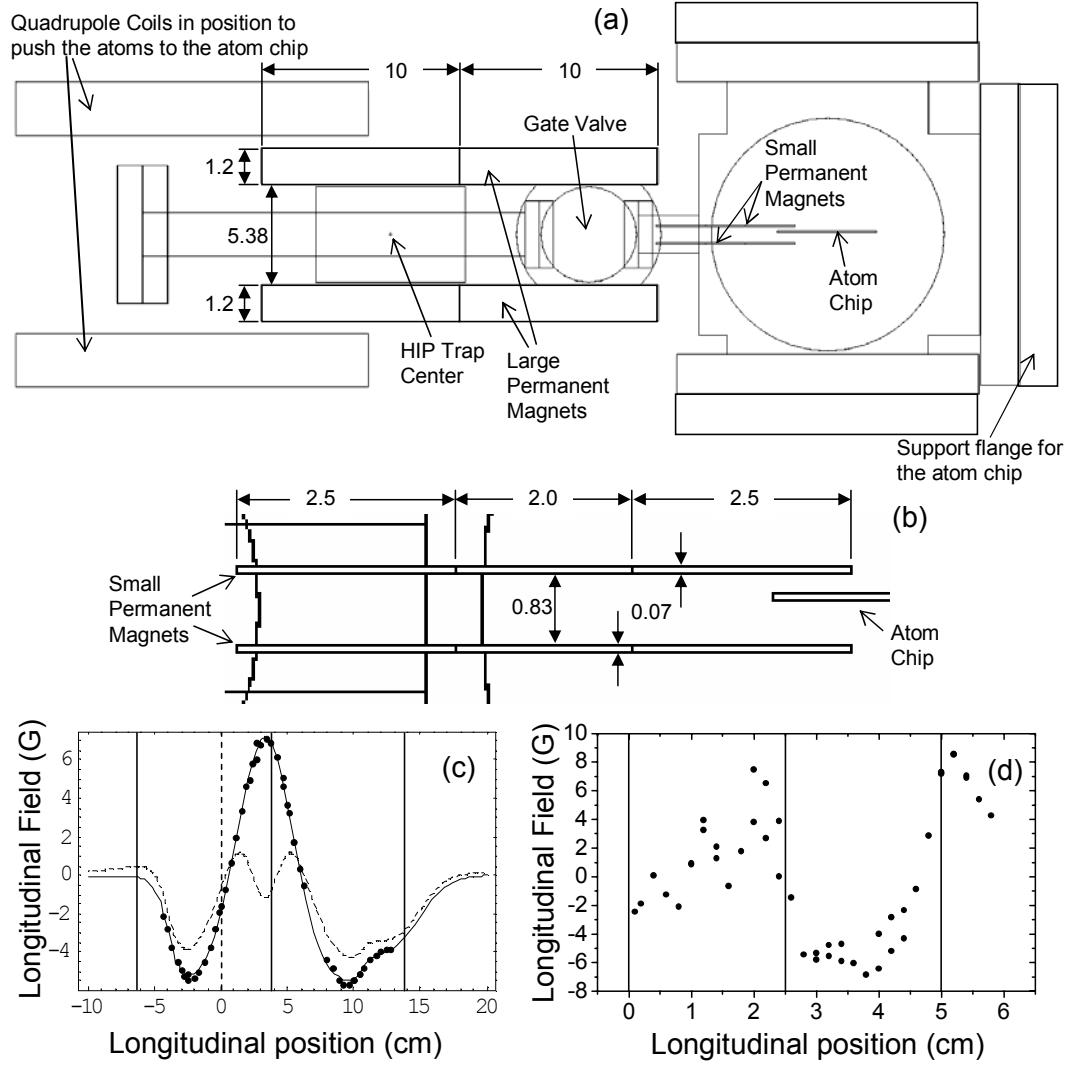


Figure 4.1: (a) A to-scale schematic of the evaporation chamber and application chamber shows the location of the large and small permanent magnets relative to the HIP trap center and the atom chip. The large magnets guide the atoms through the gate valve, and then the atoms move into the small magnets. The large magnets have a width of 4.6 cm. The distance from the HIP trap center to the atom chip is 21 cm. All of the dimensions are in centimeters. (b) An expanded view of the small permanent magnets. Their width is 0.6 cm. (c) This plot shows the measured longitudinal field from the large permanent magnets. The solid trace is an analytical approximation to the data. The dashed trace is the sum of the calculated field of the cancellation coils and the analytical approximation to the stray field from the magnets. The solid vertical lines indicate the edges of the magnets, and the vertical dotted line denotes the center of the HIP trap. (d) Measurement of four small permanent magnets. These magnets were never put into use, but they are from the same batch as the six magnets in the application chamber. The vertical lines show the edges of the permanent magnets.

the longitudinal field from our “best” set of large permanent magnets, and the joint between the magnets is where the largest longitudinal field is produced. Other sets of large magnets have a peak-to-peak magnetic field amplitude greater than 20 G, and through a process of trial and error, we selected the set of four magnets with the smallest longitudinal field.

The set of small permanent magnets also produces a longitudinal field. We attempted to select a set of six small magnets, but we found the measurements of the longitudinal field difficult to perform and not reproducible once the magnets were removed from the measuring jig. If they were replaced back into the jig, their field seemed to change. The small set of permanent magnets mounted inside the application chamber was not measured because once they were glued into the magnet holder, the magnet holder did not allow the magnetic field probe access to the center of the magnets. We did not measure the magnets before they were glued because the act of cleaning and gluing would change the longitudinal field. Measurements of another set of small magnets show a peak-to-peak amplitude of 12 G with a stronger gradient than the large magnets because they are more closely spaced (Figure 4.1(d)).

Thus, we have an irregular longitudinal potential making it very difficult to control the speed and the longitudinal spread of the cloud as it moves to the atom chip. To accelerate the atoms over the large “bump” of the large permanent magnets, we have to use both the quadrupole coil and the entrance IP coils while shutting off the exit IP coils (Figure 4.2). Once the atoms are over the bump of the large permanent magnets, they are traveling at a speed of 35 cm/s. At this speed the atoms experience a large transverse acceleration as they transfer from the small permanent magnets onto the atom chip as discussed in Section 3.4. Thus, we use a number of different coils to slow and focus the cloud as it is moving toward the atom chip. By ramping the coils on and off in time we can control the speed and spreading of the cloud. In the following sections I discuss the theory of using a coil to slow and focus the cloud and the various

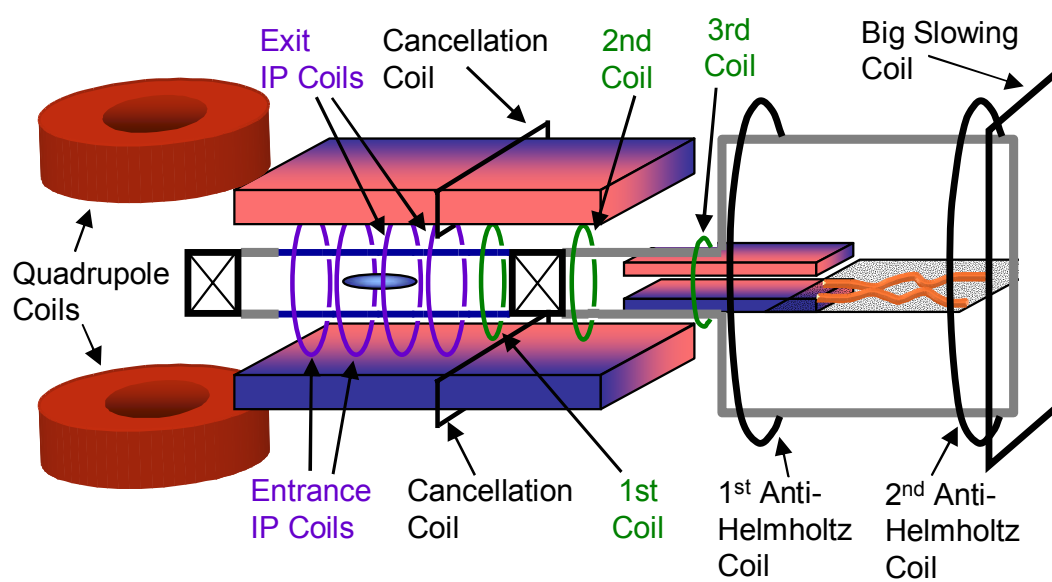


Figure 4.2: Schematic of the coils used to slow and focus the atoms.



multiple-coil schemes we have implemented experimentally.

## 4.2 The Concept of Slowing and Focusing with a Coil

As the atoms move toward the atom chip, they are radially confined by the permanent magnets, but are not confined axially. To reduce the longitudinal speed of the atoms, we can add a coil wrapped around the outside of the vacuum chamber, and as the atoms approach the coil, they lose kinetic energy by moving into the magnetic field of the coil. Once the atoms have lost enough kinetic energy, we ramp off the current running through the coil and allow the atom to propagate freely at a slower speed. However, the coil does not affect all of the atoms equally, and the head of the cloud loses more kinetic energy than does the tail, causing the cloud to focus.

### 4.2.1 A Simple Analytical Model for Slowing and Focusing

To better understand the effect of these coils, we develop a simple model to show the general behavior of the atoms as they experience a coil's field. We approximate the coil's potential as a simple linear slope, and the atoms approach the slope on a flat potential (Figure 4.3(a))

$$V(x) = \begin{cases} 0 & \text{for } x < 0 \\ m_{Rb}ax & \text{for } x \geq 0 \end{cases} \quad (4.1)$$

where  $x$  is the longitudinal coordinate and  $a$  is the longitudinal acceleration provided by the coil. We will first derive the behavior of a collimated beam of atoms. The atoms move in the positive  $x$ -direction with a uniform velocity,  $v_o$ , and are uniformly distributed over a length,  $l$ . We define  $t = 0$  when the center of cloud is at  $x = 0$ . Before the atoms move onto the slope they experience no forces. The position of an atom as a function of time is simply given by

$$x(t; x_o) = x_o + v_o \left( t + \frac{l}{2v_o} \right) \quad \text{for} \quad t < \frac{-x_o}{v_o} - \frac{l}{2v_o} \quad (4.2)$$

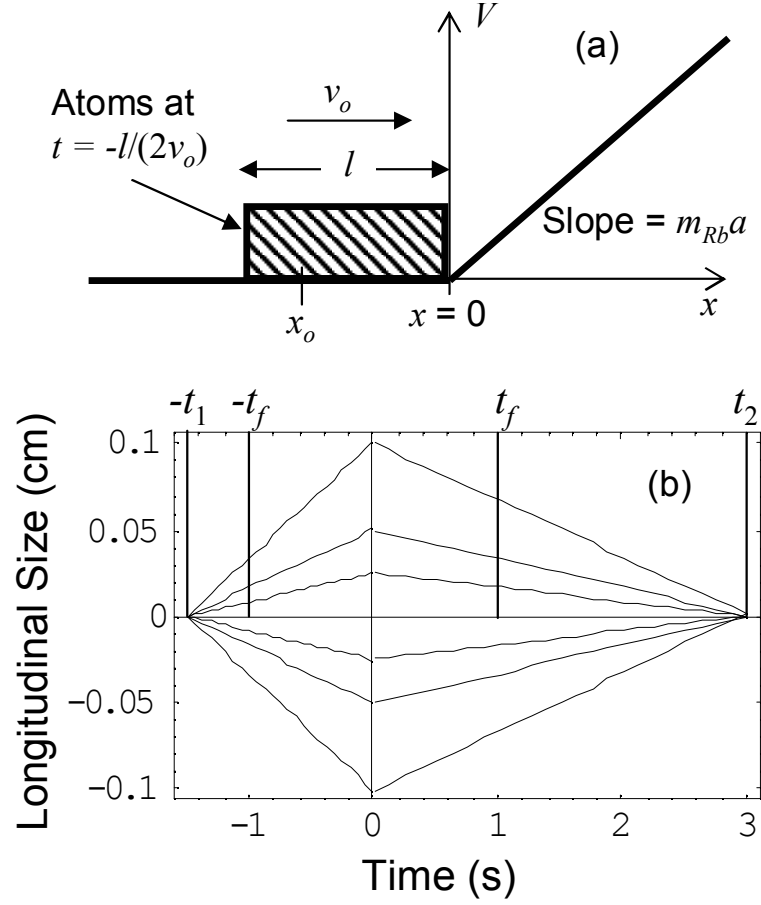


Figure 4.3: (a) A schematic of the slowing and focusing potential. The atoms are shown just before they move onto the linear slope. In (b) the trajectories of several atoms are plotted relative to the center of the cloud as function of time. The cloud is at a minimum size at  $-t_1 = -1.5$  s and then expands at a velocity,  $v_s$ , until it reaches  $x = 0$ . There, it is made to converge as it moves onto the linear slope, and at  $t_2 = 3$  s, it is focused again. The other parameters are  $t_f = 1$  s,  $a = 10$  cm/s<sup>2</sup>,  $v_o = 10$  cm/s,  $v_s = 0.067$  cm/s, and  $l = 2$  mm.

where the parameter  $x_o$  is the position of a single atom within the cloud at  $t = \frac{-l}{2v_o}$  just before the head of the cloud moves onto the slope (Figure 4.3(a)). It is constrained by  $-l \leq x_o \leq 0$ . Equation 4.2 is only valid for an atom at a position  $x < 0$ . After an atom moves onto the linear slope, it experiences a deceleration, and its position as a function of time is

$$x(t; x_o) = v_o \left( t + \frac{x_o}{v_o} + \frac{l}{2v_o} \right) - \frac{1}{2} a \left( t + \frac{x_o}{v_o} + \frac{l}{2v_o} \right)^2 \quad \text{for} \quad \frac{-x_o}{v_o} - \frac{l}{2v_o} \leq t < t_c. \quad (4.3)$$

On the slope an atom experiences a linear decrease in velocity given by

$$v(t; x_o) = v_o - a \left( t + \frac{x_o}{v_o} + \frac{l}{2v_o} \right) \quad \text{for} \quad \frac{-x_o}{v_o} - \frac{l}{2v_o} \leq t < t_c. \quad (4.4)$$

At  $t = t_c$ , the acceleration,  $a$ , is set to zero (the coil is turned off), and Equations 4.3 and 4.4 are no longer valid. An atom, then, propagates on a flat potential, and its position is found by evaluating Equations 4.3 and 4.4 at  $t_c$  to form the equation

$$\begin{aligned} x(t; x_o) = & v_o \left( t_c + \frac{x_o}{v_o} + \frac{l}{2v_o} \right) - \frac{1}{2} a \left( t_c + \frac{x_o}{v_o} + \frac{l}{2v_o} \right)^2 \\ & + \left( v_o - a \left( t_c + \frac{x_o}{v_o} + \frac{l}{2v_o} \right) \right) (t - t_c) \quad \text{for} \quad t > t_c. \end{aligned} \quad (4.5)$$

After the coil is turned off the cloud travels at a constant velocity. This final center-of-mass velocity is found by evaluating Equation 4.4 at  $t_c$  at the center of the cloud,  $x_o = \frac{-l}{2}$ ,

$$v_f = v_o - at_c. \quad (4.6)$$

While the cloud is moving onto the slope, the atoms at the head of the cloud spend more time decelerating than the atoms at the tail. This causes the atoms to focus toward each other. Because the cloud is initially collimated, we can find the focal length,  $f$ , and the focal time,  $t_f$ , of this atom lens. The focal time, the time at which the cloud reaches its minimum longitudinal size, is found by setting  $x(t; \frac{-l}{2} - \delta) = x(t; \frac{-l}{2} + \delta)$  in Equation 4.3, where  $\delta$  is a small displacement. Solving for  $t$  gives

$$t_f = \frac{v_o}{a}, \quad (4.7)$$

and the focal length is given by

$$f = x\left(t_f; \frac{-l}{2}\right) = \frac{v_o^2}{a} - v_o t_c + \frac{at_c^2}{2}. \quad (4.8)$$

To work well as an atom lens,  $t_c$  has to be long enough to allow all of the atoms to move onto the slope, giving the condition  $t_c \geq \frac{l}{2v_o}$ .

We can also consider a cloud of atoms that are converging or diverging as they approach the atom lens. For example, at a time,  $-t_1$ , the atoms are all at a point in space but are spreading at a speed,  $v_s$ . At  $t = 0$  the atoms are moving onto the linear slope, and their relative velocity distribution is being modified such that they begin to focus again. The time at which they come to a second focus,  $t_2$ , is given by

$$\frac{1}{t_1} + \frac{1}{t_2} = \frac{1}{t_f} \quad (4.9)$$

We take into consideration clouds that are not collimated in the model by making  $v_o$  a function of the initial position,  $x_o$ , in Equations 4.2, 4.3, 4.4 and 4.5,

$$v_o(x_o) = v_o + v_s \left(1 + \frac{2x_o}{l}\right) \quad (4.10)$$

Given  $v_s$ , we have

$$t_1 = \frac{l}{2v_s} + \frac{l}{2v_o}. \quad (4.11)$$

Figure 4.3(b) shows the trajectories of the atoms as they are focused by the longitudinal lens.

Above we considered a cloud with no finite size at  $t = -t_1$ , but a real cloud would have both an initial size and an initial velocity distribution. Reference [24] develops a lens model for a cloud initially trapped with independent Gaussian distributions of position and velocity, and the cloud is released and allowed to freely expand. The atoms pass through a parabolic longitudinal lens that is applied at one point in time, whereas our lens is applied at one point in space. Nevertheless, they derive Equation 4.9 for their lens, and they show that the magnification of the cloud by a longitudinal lens is

$$\gamma = -\frac{t_2}{t_1}, \quad (4.12)$$

Equations 4.9 and 4.12 show that a longitudinal lens for atoms behaves in time like a thin optical lens for light behaves in space.

#### 4.2.2 The Analytical Model Compared to a Coil

The longitudinal field from a coil slows and focuses the atoms in the actual experiment. A coil's field continuously slows the center of mass and changes the relative velocity within the cloud as it approaches the coil, whereas the simple potential of the analytical model changes the relative velocity of the atoms only at one point,  $x = 0$ , and then slows the atoms as they move up the potential. Because the coil's potential is continually changing, it is not obvious how to define the focal length or the focal time of a coil. By comparing a numerical model of a cloud propagating in a coil's magnetic field to the above analytical model, we can define these quantities and study the effect of the curvature of the coil's field.

We can numerically evaluate the behavior of a cloud as it approaches the coil by integrating the differential equation

$$\frac{d^2x}{dt^2} = \frac{-\mu_B g_F m_F}{m_{Rb}} \frac{\partial B_c(x)}{\partial x} \quad (4.13)$$

following the trajectories of several different atoms within the cloud. The longitudinal magnetic field from the coil  $B_c(x)$  is given by

$$B_c(x) = \frac{\mu_o I N_t r_c^2}{2(r_c^2 + (x - x_c)^2)^{3/2}} \quad (4.14)$$

where  $I$  is the current,  $N_t$  is the number of turns of wire,  $r_c$  is the radius of the coil, and  $x_c$  is the longitudinal position of the coil. We allow the atoms to propagate toward the coil until the center of mass of the cloud reaches a certain point,  $x_i$ . Then, the coil is shut off, and the atoms propagate freely.

We approximate the coil's field with the analytical model in the following way. We set the point  $x = 0$  such that a line from the origin is tangent to the potential from

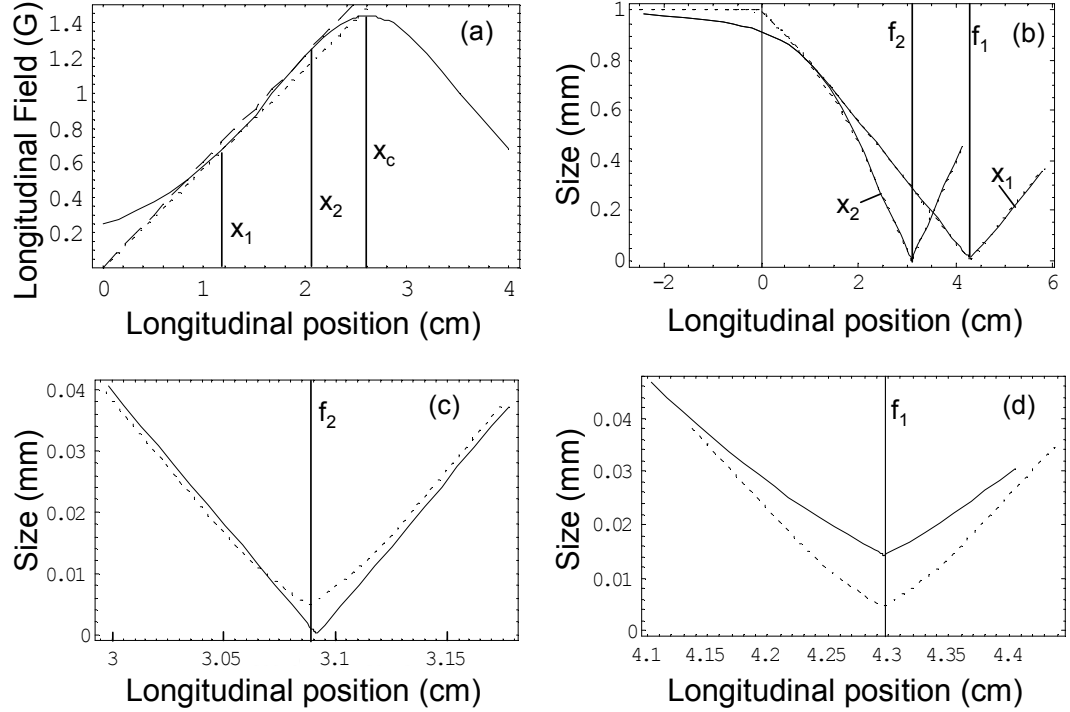


Figure 4.4: Comparison of the analytical model to the numerical model of the coil's potential where an initially collimated cloud is travelling at a velocity of  $v_o = 10$  cm/s and its initial full width is  $l = 2$  mm. (a) The potentials used in the numerical and analytical models. The solid line is the field from a coil centered at  $x_c = 2.6$  cm. ( $r_c = 1.75$  cm and  $IN_t = 4$  Amp-Turns) The atoms propagate to two different positions before the coil is shut off:  $x_i \rightarrow x_1 = 1.19$  cm and  $x_i \rightarrow x_2 = 2.06$  cm. The dotted line is tangent to the coil's potential at  $x_1$  (the acceleration,  $a_1 = 18.22$  cm/s<sup>2</sup>), and the dashed line is tangent to the coil's potential at  $x_2$  ( $a_2 = 19.44$  cm/s<sup>2</sup>). (b) The half width of the cloud as a function of longitudinal position. The solid line shows the size of the cloud propagating on the coil's potential, and the dotted line is for the atoms propagating on the linear potentials. The labels  $x_1$  and  $x_2$  indicate to which position the atoms propagate before the coil (or linear slope) is shut off. (c) The size of the cloud is plotted near the focus,  $f_2 = 3.088$  cm, for the atoms that propagated to  $x_2$  before the coil was shut off. With a negative curvature in the coil's potential at  $x_2$ , the aberration of the coil (solid line) is less than the aberration of a linear slope (dotted line), giving a smaller size at the focus. (d) The size of the cloud is plotted near the focus,  $f_1 = 4.295$  cm, for the atoms that propagated to  $x_1$  before the coil was shut off. With a positive curvature in the coil's potential at  $x_1$ , the aberration of the coil (solid line) is more than the aberration of a linear slope (dotted line), giving a larger size at the focus.

the coil at the point  $x_i$  (Figure 4.4(a)). Given the position of the coil relative to the origin,  $x_c$ , one finds that  $x_i$  is given by satisfying the condition

$$B_c(x_i) = x_i \left. \frac{\partial B_c(x)}{\partial x} \right|_{x=x_i}. \quad (4.15)$$

Solving for  $x_i$ , we have

$$x_i = \frac{1}{8} \left( 2x_c \pm \sqrt{9x_c^2 - 16r_c^2} \right). \quad (4.16)$$

The line from the origin to the point  $\{x_i, B_c(x_i)\}$  is the linear potential for the analytical model, and the acceleration,  $a_i$ , is determined by evaluating Equation 4.13 at  $x_i$ . Again,  $t = 0$  is defined as the time when the center of the cloud is at  $x = 0$ , and the time at which the potential goes to zero,  $t_c$ , is given by

$$t_c = \frac{v_o}{a_i} \left( 1 - \sqrt{1 - \frac{2a_i x_i}{v_o^2}} \right). \quad (4.17)$$

To compare the numerical model of the coil to the analytical model, we evaluate how a collimated cloud with a initial velocity,  $v_o$ , behaves in both models. In Figure 4.4, we evaluate the behavior of the two models for the coil being shut off when the atoms are at two different positions:  $x_i \rightarrow x_1$  and  $x_i \rightarrow x_2$ . Figure 4.4(b) shows that the size of the cloud given by both the model of the coil and the model of the linear potential agree very well, and the focal lengths given by each model agree to 0.1%. Thus, by defining the position of origin and slope of the linear potential using the criterion of the previous paragraph, we can accurately determine the focal time and focal length of the coil with Equations 4.7 and 4.8. Around the point  $x = 0$ , the size of the cloud in the two models does vary significantly. The atoms being slowed by the coil start to focus earlier because the slope of the coil's field changes continuously, while the slope of linear potential changes abruptly at  $x = 0$ . After the atoms reach  $x_1$  or  $x_2$  and the coil and the linear potential are shut off, the two models are in almost complete agreement.

Both the linear potential and the potential from the coil cause aberrations when the atoms come to a focus, i.e. the minimum longitudinal size, or “spot size,” does not

go to zero for an initially collimated cloud. In Reference [24], a longitudinal focusing scheme is demonstrated that does not produce aberrations. In this case the relative velocity is modified at a single point in time by a parabolic potential that is rapidly turned on and then off. The potential works purely as a lens and does not slow the cloud. In the case of the linear potential shown here, aberrations occur because the relative velocity within the cloud is modified as the atoms pass over the point  $x = 0$ , and each atom's relative velocity is modified at a different time. The minimum size for a collimated cloud that has been focused by a linear potential is  $al^2/(8v_o^2)$ . When a coil is used to slow and focus as presented here, the aberrations can be worse or better than the linear potential. In Figure 4.4(c) and (d) both cases are shown. When the second derivative of the coil's potential is positive as the coil is shut off (as is the case for  $x_i \rightarrow x_1$ ), the minimum size of the cloud at  $f_1$  is larger than the cloud that propagates on the linear potential. However, for  $x_i \rightarrow x_2$ , the second derivative of the coil's potential is negative, and the aberrations are almost perfectly corrected giving a small spot size at  $f_2$ . The aberrations are chromatic—they depend on the center-of-mass velocity of the cloud. Thus, shutting off the coil when the cloud is at  $x_2$  corrects the aberrations only for a cloud traveling at  $v_o = 10$  cm/s.

To continue the analogy with optical lenses, the focal length of the coil depends on the slope of the potential the atoms are experiencing when the coil is shut off. A large (small) slope results in a short (long) focal length and a fast (slow) lens. The spot size at the focus is determined not only by the magnification given by Equation 4.12, but also by the aberrations of the lens, which are affected by the size of the cloud when it reaches the coil, the center-of-mass speed of the cloud, and the curvature of the potential when the coil is shut off.



Table 4.1: The coils used in the various slowing and focusing experiments.

Coil Name	Distance from IP center (cm)	Length of side/ Diameter (cm)	Shape	Typical Amp-Turns
1st	7.5	3.5	circle	$20 \times 10$
2nd	13.5	3.5	circle	$10 \times 12$
3rd	15.5	2.1	circle	$-2 \times 12$
IP Entrance: Outer	-2.0	3.8	square	$8 \times 51$
Inner	-0.75	3.8	square	$-8 \times 20$
IP Exit: Outer	2.0	3.8	square	$8 \times 51$
Inner	0.75	3.8	square	$-8 \times 20$
Big Slowing	34	30	square	$12 \times 45$
1st Anti-Helmholtz	13	14	circle	$-11 \times 40$
2nd Anti-Helmholtz	32	16.5	circle	$14 \times 80$
Quadrupole	-10	14	circle	$14 \times 48$
Cancellation	3	$1.6 \times 7.7$	rectangular	$15 \times 15$

### 4.3 Slowing and Focusing During Transport to the Chip

To move the atoms to the application chamber, given the longitudinal potential of the permanent magnets, we at first use a brute force method to push the atoms. By ramping off the exit IP coils and ramping up the current in the entrance IP coils and the quadrupole coils (Figure 4.2 and Table 4.1), we are able to accelerate the atoms to a point where they have enough energy to make it over the large “bump” from the large magnets. Figure 4.5 shows the timing and the currents in the coils to release the atoms. Because of the large initial potential energy of 33 G we give to the atoms to get over the bump (Figure 4.6(a)), the atoms are traveling at 35 cm/s after they are loaded into the chip’s waveguide. On the chip, the guide is produced with a 1-A current in the primary wire, a 22-G transverse bias field and a 3-G longitudinal field, giving a guide frequency of  $\omega_r = 2\pi \times 1270$  kHz. A cloud at an initial temperature of  $0.45 \mu\text{K}$  before it is released heats to  $2.8 \mu\text{K}$  after it is loaded onto the chip. We suspect that most of the heating occurs as the atoms are loaded onto the chip. The cloud spreads to a longitudinal width of 6 mm FWHM.

To slow and bring the atoms to a focus on the chip, we mainly use two coils. The

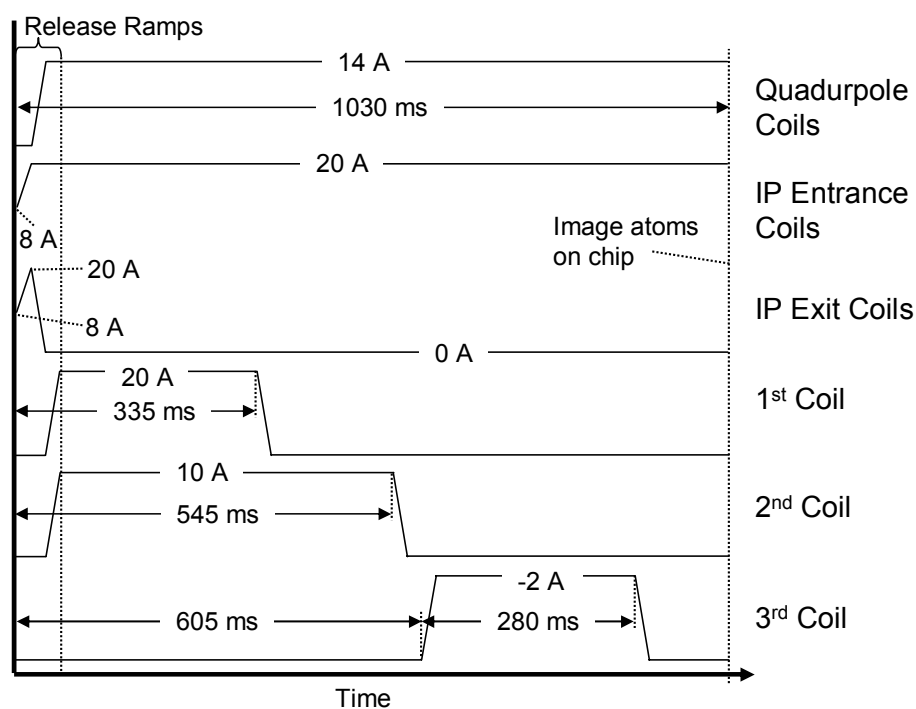


Figure 4.5: The timing diagram shows when the various coils for slowing and focusing the atoms are ramped on and off. Timing for the 1<sup>st</sup> and the 2<sup>nd</sup> coil gives a focused cloud on the chip traveling at 20 cm/s. All ramps last for 30 ms.

1st coil (Figure 4.2 and Table 4.1) removes kinetic energy from the center of mass of the cloud as we allow the atoms to move fairly high up the potential of the coil, but it creates a fast lens and increases the relative velocity of the atoms. Before the atoms reach the 2nd coil, the cloud focuses once and is expanding when it reaches the 2nd coil. We make the 2nd coil a slower lens such that it can collimate the atoms or focus the atoms at some point on the chip. The timing and currents used for the 1st and 2nd coils are shown in Figure 4.5.

Ideally, with this two coil system we could arbitrarily control the speed and spread of the atoms. However, the set of small permanent magnets creates an unknown longitudinal field, and the effectiveness of the two coil approach is limited. We have found that adding the 3rd coil can partially cancel this longitudinal field at the beginning of the small magnets. Figure 4.6(b) shows the potential created by the first two coils, neglecting the 3rd coil as we are unsure of the potential from the small magnets. With all three coils we can reduce the velocity of the cloud to 20 cm/s and its size to 3 mm FWHM. However, the cloud is still heated, and its transverse temperature can vary widely. A cloud originally at  $0.45\ \mu\text{K}$  heats from  $1.3\text{--}5.5\ \mu\text{K}$  depending on the density of the atoms and other focusing parameters (Table 4.2). While the cloud is focusing, the density increases and so does the temperature. Additionally, there is evidence that we do not focus the whole cloud. Estimates of the total number of atoms in the HIP trap and the number of atoms in a focused cloud on the chip show that the number may be reduced by a factor of 4 to 6 during the transfer. The numerical calculation shown in Figure 4.6(f) indicates that the two coil focusing has large aberrations, suggesting that we do not focus the whole cloud.

#### 4.3.1 Bounce Experiment

Unfortunately, slowing and focusing introduces another transverse heating mechanism. When the atoms go through a focus, the tail of the cloud overtakes the head,

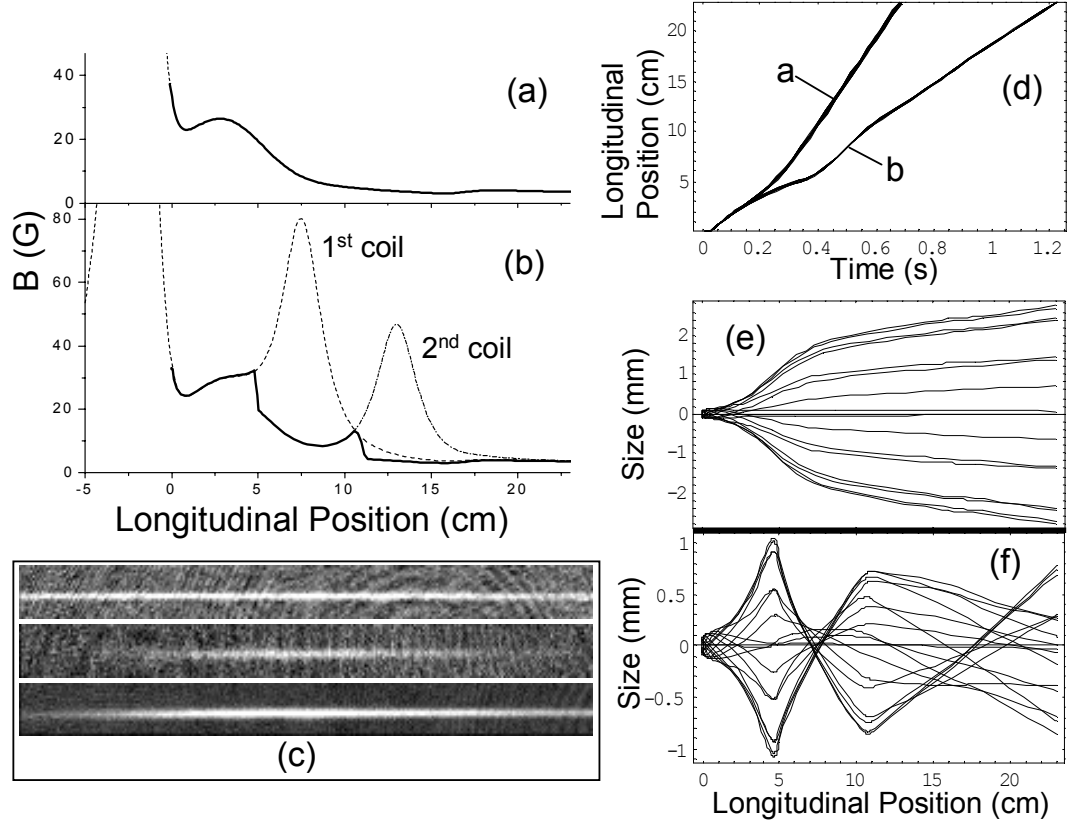


Figure 4.6: (a) The longitudinal field is plotted versus the longitudinal position, and the plot shows the potential from the permanent magnets, the entrance IP coils, and the quadrupole coils. In Plot (b) the solid line shows the potential the atoms experience as they move toward the atom chip and the coils are switched off in time. The dashed (dot-dash) line is the field from the 1st coil (2nd coil). (c) The first image shows a cloud loaded onto the chip traveling at 35 cm/s, and it has a temperature of  $2.8 \mu\text{K}$  and peak density of  $0.64 \times 10^{12} \text{ cm}^{-3}$ . The second cloud is slowed to 20 cm/s and has a temperature of  $2.5 \mu\text{K}$  and peak density of  $0.5 \times 10^{12} \text{ cm}^{-3}$ . The third cloud also is slowed to 20 cm/s and has a temperature of  $5.5 \mu\text{K}$  and peak density of  $1.0 \times 10^{12} \text{ cm}^{-3}$ . (d) This plot shows the numerically calculated longitudinal position as a function of time for atoms propagating in the potentials of plots (a) and (b). Plot (e) shows the longitudinal position of various atoms relative to the center of mass of the cloud as a function of the longitudinal center-of-mass position. The atoms are propagating in the potential of plot (a). Plot (f) is similar to (e) except the atoms are propagating in the potential of plot (b) where the 1st and 2nd coil slow and focus the atoms. Aberrations from the two coils do not allow the atoms to focus to a small size on the chip.

and during this process, the atoms can collide. The large relative kinetic energy induced by a fast lens can be redistributed into the transverse degrees of freedom. To better understand this process we perform a simple bouncing experiment in the evaporation chamber. The atoms are released out of the HIP trap by ramping off the exit IP coils and ramping up the entrance IP coils to 20 A and the quadrupole coils to 12 A. Next, the 1st coil is ramped on to 14 A. The potential in which the atoms propagate is shown in Figure 4.7(a). The atoms propagate away from the HIP trap center until they are reflected by the 1st coil. We image the atoms as they return to the trap center where they are reflected by the entrance IP coils. As the atoms come into the imaging region, they are not noticeably heated by the first reflection because the relative velocity induced by this reflection is roughly equal to the transverse velocity (if there is any heating it is below the resolution of our imaging), but as they bounce off the entrance IP coils, the head of the cloud passes through the tail—every atom must traverse the whole cloud. The relative velocity is large and the probability of a collision is high (for the conditions in Figure 4.7 the probability is 0.7), allowing the transfer of energy from the longitudinal dimension to the transverse dimensions.

We have developed a simple 1-D model that traces the trajectories of single atoms in the longitudinal direction similar to the model used in Section 4.2.2 except in this case we fully model all of the fields created by the magnets and the coils. The atoms start in HIP trap, and each atom is given some initial potential and kinetic energy such that each atom starts with the same total energy. Then, we simulate the ramping on and off of the various coils used in the experiment and allow the atoms to propagate by integrating Equation 4.13. Using this initial energy distribution, we can extract the center-of-mass position and velocity, average size, and relative velocity of the cloud by tracing only 16 trajectories. With this model we achieve good qualitative agreement with the experiment, and in cases where we know the potential very well, quantitative agreement is good. The main unknown in the potential is the longitudinal field from

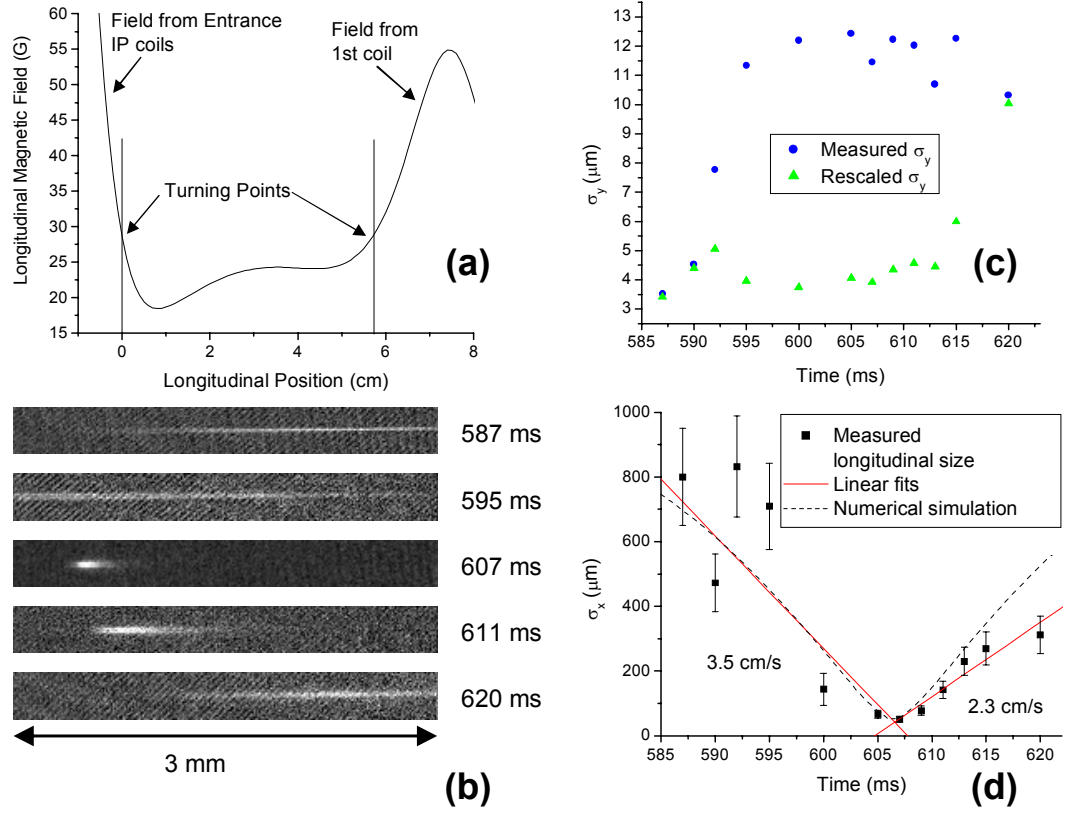


Figure 4.7: (a) The longitudinal magnetic field is plotted versus the longitudinal position. The atoms start at the left turning point. (b) The series of pictures shows cloud compressing longitudinally as the head and the tail of the cloud pass through each other. (c) The radial size is plotted versus time. The size is rescaled because the camera is not focused on the cloud across the image. (d) The longitudinal size passes through a minimum as the head and tail of the cloud pass through each other. The solid lines are linear fits to the contracting and expanding cloud. The dashed line is a numerical simulation of the longitudinal size. The numerical simulation expands faster than the actual cloud because the simulation does not allow the transfer of energy to the radial direction.

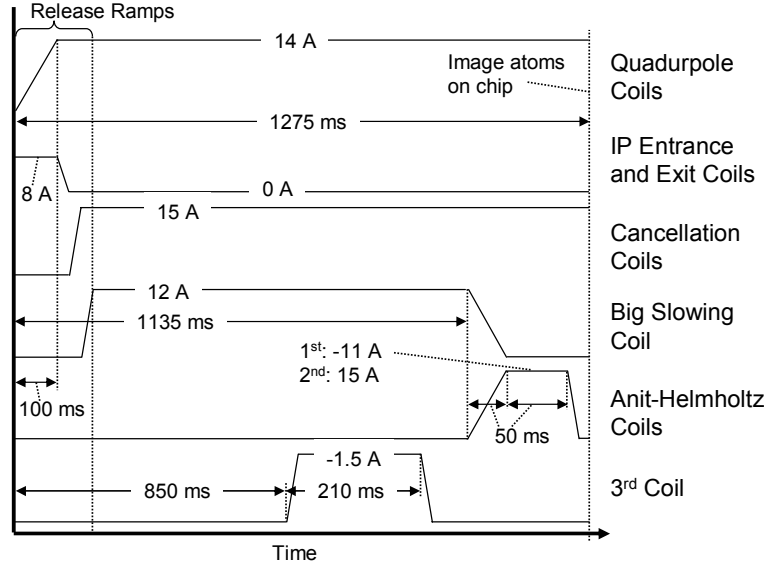


Figure 4.8: The timing diagram shows when the various coils for slowing and stopping the atoms are ramped on and off. The currents and timings vary depending on the experiment performed. In particular, the timing of the anti-Helmholtz coils varies depending on the desired final speed of the cloud. All ramps last for 30 ms unless labeled otherwise.

the permanent magnets. Using the potential in Figure 4.7(a), the model shows upon reflection off of the 1st coil that the relative velocity is less than 0.5 cm/s, but when the cloud reflects off of the entrance IP coils the relative velocity jumps to 3.5 cm/s due to the very steep potential. A linear fit to the experimentally measured size of the cloud as it compresses shows the same relative velocity (Figure 4.7(d)). However, when the cloud expands, the expansion velocity is reduced to 2.3 cm/s indicating that cloud should heat radially to a size of  $9 \mu\text{m}$  as energy is transferred to the radial dimensions. Indeed, Figure 4.7(c) shows that the radial size increases as the cloud expands to approximately  $10 \mu\text{m}$  corresponding to a radial temperature of  $\sim 600 \text{ nK}$ .

#### 4.3.2 A New Slowing Method

The implications of the bounce experiment are that if we are going to focus the atoms we must maintain a small relative velocity during the focusing. The two coil

slowing and focusing scheme gives 1 cm/s relative velocity resulting in heating. One way to reduce the relative velocity from focusing is to reduce the initial gradient on which the atoms are released. As seen in the bouncing experiment, the entrance IP coils have a large gradient, but the quadrupole coils do not. With the quadrupole coils positioned 10 cm away from the HIP trap center, they produce a weaker gradient over a much longer range. We can also reduce the necessary initial potential energy given to the atoms by cancelling the bump from the large magnets. Two coils wrapped around the magnets, centered on the position of the magnets' bump can reduce the bump's peak-to-peak amplitude by 7 G (Figure 4.1(c)). Thus, the final kinetic energy is reduced, and with the quadrupole coils and the cancellation coil, we can achieve the same velocity of 20 cm/s without using slowing and focusing coils. To further slow the atoms, we place the big slowing coil at the end of the application chamber (Figure 4.2 and Table 4.1). This big slowing coil gives a long range slowing and focusing potential. This coil focuses the whole cloud, whereas the two coil scheme did not, and we observe that the number of atoms guided on the chip is approximately equal to the number in the HIP trap. The numerical calculation in Figure 4.9(f) shows that the big slowing coil produces smaller aberrations than the two coil method while it focuses a longer cloud. Although the heating seems to be similar, more of the cloud is focused, and the density and the phase-space density are improved by a factor of five compared to the two coil system (Table 4.2).

To further slow or stop the atoms on the chip, we use an asymmetric anti-helmholtz (AH) pair of coils where the coils are placed on either side of the application chamber (Figure 4.2). With these coils on, they provide a linear slope with little curvature. As the atoms experience this potential they are slowed but not focused because on a linear slope every atom's velocity is reduced equally. In Section 4.2.1, I describe focusing with a linear potential, but this does not happen in this case because the linear slope is ramped on in time after all of the atoms have entered the region of the slope



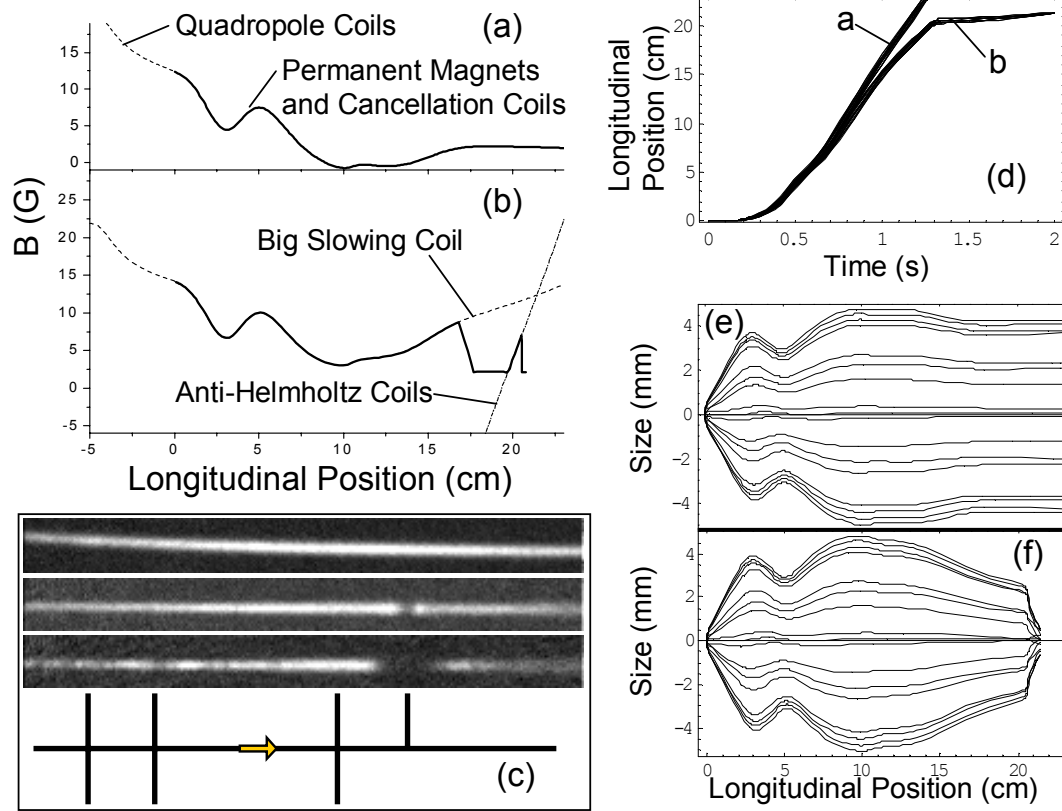


Figure 4.9: (a) The plot shows the potential from the permanent magnets, the quadrupole coils and the cancellation coils. The cancellation coils allows the atoms to start from a lower potential height, reducing their final speed. In Plot (b) the solid line shows the potential the atoms experience as they move toward the atom chip. The plot shows how the big slowing coil (dash) and the anti-Helmholtz (AH) coils (dot-dash) are switched in time to slow or stop the atoms. (c) The first image shows a cloud loaded onto the chip with the same initial conditions as the images in Figure 4.6. The cloud is slowed by the big slowing coil only and is traveling at 15 cm/s. It has a temperature of  $2.9 \mu\text{K}$  and peak density of  $4.0 \times 10^{12} \text{ cm}^{-3}$ . In the next two images, the atoms are slowed by the big slowing coil and the AH coils, and their temperature of  $1.4 \mu\text{K}$  is lower because the cloud initially started in the evaporation chamber with a lower temperature. The second cloud is slowed to 5 cm/s and split by the T in the primary wire. The third cloud is slowed to  $> 1 \text{ cm/s}$  and fragmentation occurs from the deviations of the wire current. Last is a schematic of the primary wire in the trapping region. (d) This plot shows the numerically calculated longitudinal position as a function of time for atoms propagating in the potentials of plots (a) and (b). Plot (e) shows the longitudinal position of various atoms relative to the center of mass of the cloud as a function of the longitudinal center-of-mass position. The atoms are propagating in the potential of plot (a). Plot (f) is similar to (e) except the atoms are propagating in the potential of plot (b) where the big slowing and AH coils slow and focus the atoms. Because the atoms are almost stopped, they come to a focus while the center of mass is stationary.

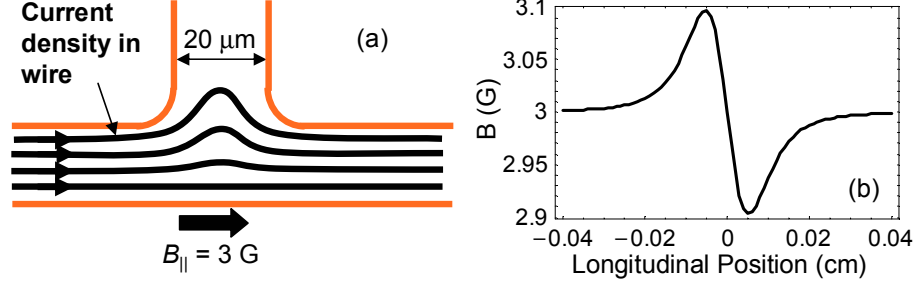


Figure 4.10: (a) Schematic drawing of the current inside the primary wire as it passes by an intersecting wire forming a T junction. The chip fabrication process tends to round the inside corner of the T. We apply a longitudinal bias field with external coils. (b) The estimated longitudinal component of the magnetic field from the current deviation superposed on the 3-G uniform longitudinal bias field is plotted 100  $\mu\text{m}$  away from the wire. The current in the wire is 1 A.

so the entire cloud experiences the same slowing force. In this way, the big stopping coil gently focuses the cloud, and the AH coils slow, stop, or reverse the direction of the cloud. With the AH coils we can stop the atoms at almost any location on the chip. Figure 4.9(c) shows a 1.4  $\mu\text{K}$  cloud slowed to 5 cm/s and  $< 1 \text{ cm/s}$  in the trapping region of the chip. As the cloud slows, the longitudinal field from the current in the main wire reveals itself in the cloud. Figure 4.9(c) shows that the cloud fragments in the area of a T in the main wire. This occurs because the current expands into the T and is thus no longer flowing straight down the wire [59] (Figure 4.10). If the current is locally flowing at an angle to the primary wire, it produces a localized longitudinal field. We estimate that the T causes a 100-mG feature in the longitudinal field when there is 1 A flowing in the wire. When there is a cross in the main wire, the current expands symmetrically, and the effect is minimized. However, careful examination of the stopped cloud shows that there still is a small effect, and the atoms bunch up on the “upstream” side of the crosses. Other structure in the cloud is due to small deviations of the average direction of current in the primary wire as shown by References [59, 79].

We have studied various ways of moving the atoms to the atom chip, the results of which are summarized in Table 4.2. We have made improvements in the transfer,

Table 4.2: The results of the slowing and focusing experiments. This table compares the properties of a cloud of atoms in the HIP trap and on the atom chip using three different transfer methods.

Focusing Condition	Speed (cm/s)	Temperature ( $\mu$ K)	Peak Density ( $cm^{-3}$ )	Phase Space Density	Number $\times 10^5$
In HIP trap	0	0.45	$8 \times 10^{12}$	0.2	$\sim 6$
Accelerate w/ Quadrupole and Entrance IP coils, No Focusing (Figure 4.6(a))	35	2.8	$6.5 \times 10^{11}$	$1 \times 10^{-3}$	N/A
Slow and focus w/ 1st and 2nd coils (Figure 4.6(b))	20	1.3-5.5	$0.3-1.1 \times 10^{12}$	$0.4-1.2 \times 10^{-3}$	$\sim 1$
Use cancellation coils, big slowing coil, and AH coils (Figure 4.9(b))	0-15	3	$4 \times 10^{12}$	$5 \times 10^{-3}$	$\sim 6$

but the atoms still heat more than expected in the transverse direction as they are transferred to the atom chip. Our hope had been that a BEC sent to the atom chip would propagate in the lowest mode of the guide, but this does not occur. To make an atom waveguide interferometer, we need a BEC as a single mode source. To achieve BEC in the waveguide on the chip, we can stop the atoms with the AH coils, trap them, and recool them in the trapping region. This is the subject of the next chapter.

## Chapter 5

### BEC on an Atom Chip

To make a BEC on our atom chip, we need to three-dimensionally confine the atoms transferred from the evaporation chamber. Once the atoms are trapped, we can evaporatively cool the atomic sample to make a condensate. The main difficulty in making a BEC on the chip was to find an effective trapping technique to efficiently capture most of the guided atoms in a longitudinally confining potential without significantly reducing the phase-space density of the cloud. The trapping region of the atom chip was designed with the idea of trapping the atoms with a Z-shaped wire, following the lead of other groups that have successfully loaded this type of trap [49, 58, 80]. This “Z trap” appeared to be a good choice for us because it can be formed with two wires intersecting the primary wire and it forms a very elongated trap in the longitudinal dimension allowing us to trap the elongated cloud in the guide. However, due to difficulties described below, we loaded the Z trap with little success, and we resorted to using a “T trap.” Formed with one wire intersecting the primary wire, the relatively short-range longitudinal potential of the T trap can capture a large percentage of the guided atoms when they are properly stopped and focused in the guide.

In this chapter I discuss several magnetic microtrapping techniques for trapping atoms on the chip, and I describe the loading procedure for these traps. With the atoms magnetically trapped on the chip, we perform radio frequency (RF) evaporation to cool the atoms to form a BEC. We can make a BEC in several different traps, including the

simultaneous formation of two BECs in side-by-side T traps.

## 5.1 Trapping Techniques

To make a trap on our atom chip, we need to provide longitudinal confinement for a cloud in the bias-field magnetic waveguide. As described in Section 3.1, the 2-D confinement of the bias-field guide is created by the transverse bias field,  $B_t$ , cancelling the magnetic field from a current-carrying wire at a distance,  $d$ , from the wire. To complete the guide, we add a longitudinal bias field,  $B_{\parallel}$ , with large external coils to set the field at the center of the guide where the radial field goes to zero. With the primary wire lying on the  $x$ -axis and  $B_t$  in the positive  $y$ -direction, the total field of the waveguide is given by

$$\mathbf{B}_0 = \begin{pmatrix} B_{\parallel} \\ B_t - \frac{\mu_o I_0}{2\pi} \frac{z}{y^2 + z^2} \\ \frac{\mu_o I_0}{2\pi} \frac{y}{y^2 + z^2} \end{pmatrix} \quad (5.1)$$

At a distance  $z = d$ , the  $y$ -component of  $\mathbf{B}_0$  goes to zero, setting the vertical position of the guide. To trap the atoms in the longitudinal ( $x$ ) direction, we need to create a local minimum in  $B_{\parallel}$ . This can be accomplished with coils near the atom chip [57], or, perhaps more conveniently, with wires on or near the chip.

### 5.1.1 The Cross Trap

Wires on the chip oriented perpendicular to the primary guide wire produce a field that is parallel or anti-parallel to  $B_{\parallel}$ , providing a local maximum or minimum in the longitudinal field [77]. With the current,  $I_+$ , running in the  $y$ -direction, a cross wire intersecting the primary wire produces the field

$$\mathbf{B}_+ = \frac{\mu_o I_+}{2\pi} \frac{1}{x^2 + z^2} \begin{pmatrix} z \\ 0 \\ -x \end{pmatrix} \quad (5.2)$$

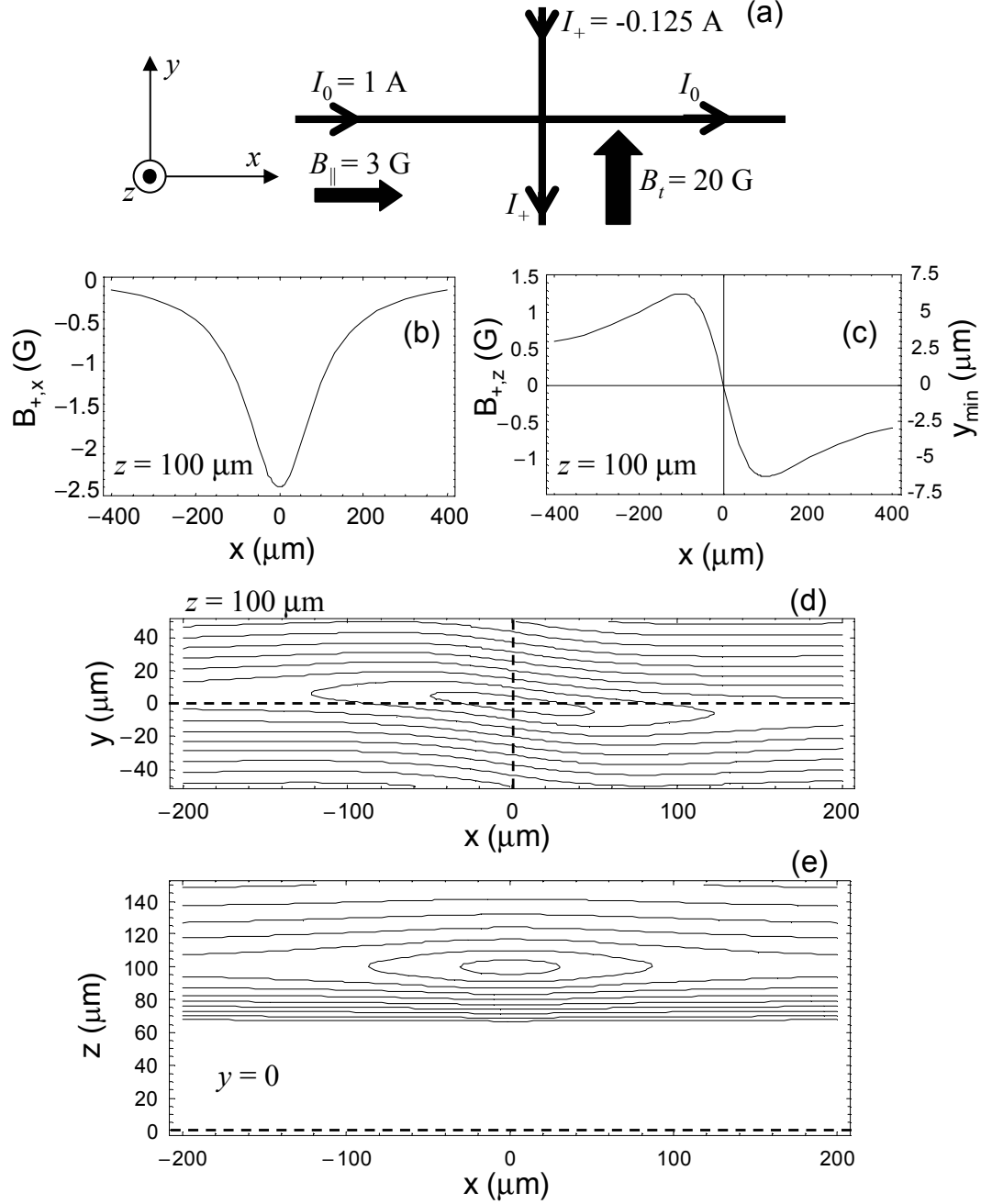


Figure 5.1: (a) Two wires intersect to form a cross trap. The primary wire lies on the  $x$ -axis and the cross wire lies on the  $y$ -axis. The  $z$ -axis points out of the page. (b) The  $x$ -component of the field from the cross wire along the line  $z = d = 100$   $\mu\text{m}$ . (c) The  $z$ -component of the field from the cross wire. The right axis show how much this field deflects the magnetic minimum in the  $y$ -direction. (d) A contour plot in the  $xy$ -plane at  $z = d$  shows the magnitude of the magnetic field. The field from the cross wire cancels  $B_{\parallel}$  to create a local minimum. The contours are spaced by 1 G, and the 1 G contour line is at the center of the plot. The dotted lines show the positions of the wires in the  $z = 0$  plane. (e) A contour plot in the  $xz$ -plane at  $y = 0$ .

Figures 5.1(b) and (c) show the  $x$ - and  $z$ -components of  $\mathbf{B}_+$  along the guide's minimum. With a positive current,  $B_{+,x}$  creates a repulsive potential for the weak-field-seeking atoms traveling in the guide. However, an attractive potential can be created by reversing the direction of  $I_+$  to partially cancel  $B_{\parallel}$  around  $x = 0$ , creating a “dimple” in the longitudinal field. In this way we can create a 3-D trapping potential in the magnetic guide (Figure 5.1(d) and (e)), but care must be taken not to completely cancel  $B_{\parallel}$  by making  $I_+$  too strong to prevent loss caused by nonadiabatic spin flips. Because a vertical field horizontally shifts the 2-D quadrupole of the guide,  $B_{+,z}$  has the effect of slightly twisting the guide in the  $xy$ -plane.

### 5.1.2 The T Trap

To reduce the number of currents we need to control for the trap, we prefer to use a T shaped wire rather than a cross wire (Figure 5.2). The T wire starts at the origin and runs along the positive  $y$ -axis. This changes the trap in two ways. The T wire's current joins the current in the primary wire, and they flow together along the positive  $x$ -axis. This causes the guiding center on either side of the T to be at different heights, and the center of the trap above the T is

$$d = \frac{\mu_o}{2\pi} \frac{I_0 + \frac{I_T}{2}}{B_t} \quad (5.3)$$

where  $I_T$  is the current in the T wire. The T trap is then twisted at a small angle in both the  $xz$ -plane and the  $xy$ -plane (Figure 5.2). The second effect is that the field produced by the T wire now depends on  $y$ ,

$$\mathbf{B}_T = \frac{\mu_o I_T}{4\pi(x^2 + z^2)} \left( 1 + \frac{y}{\sqrt{x^2 + y^2 + z^2}} \right) \begin{pmatrix} -z \\ 0 \\ x \end{pmatrix} \quad (5.4)$$

where we define a positive current in the T wire as running in the negative  $y$ -direction. Because the T wire is only half of the cross wire,  $\mathbf{B}_T = -\mathbf{B}_+/2$  in the  $xz$ -plane. Thus,



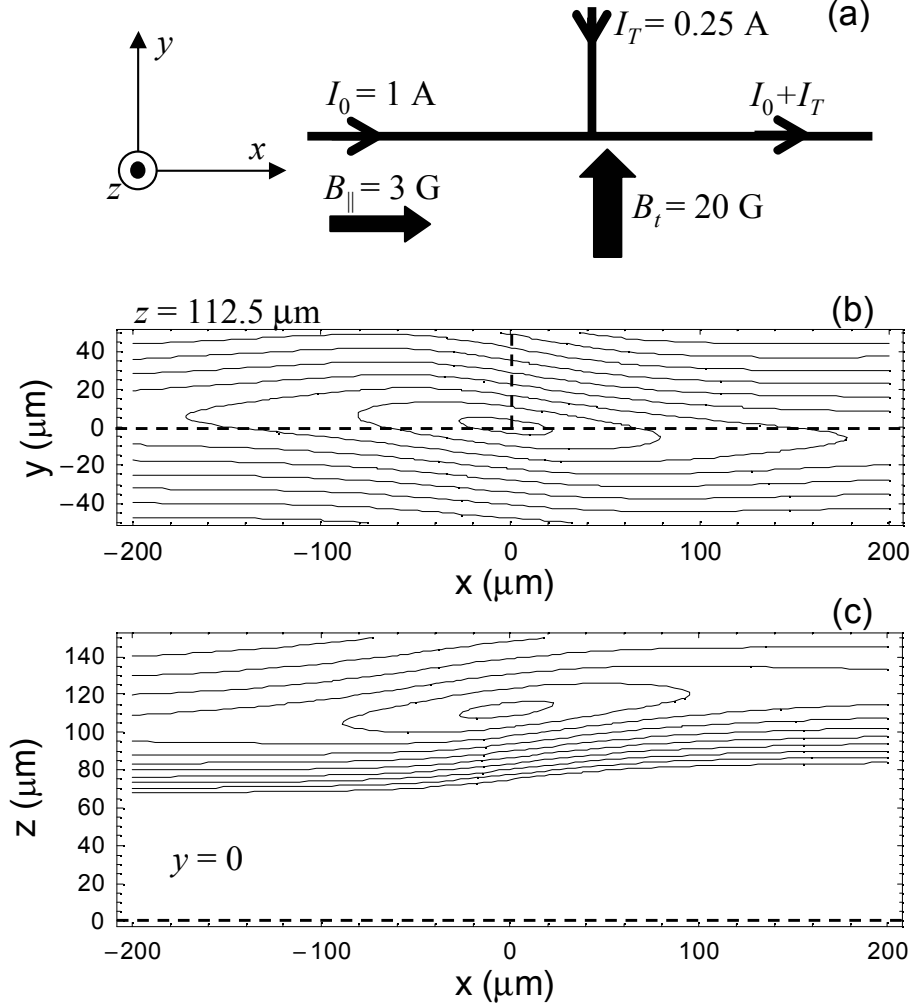


Figure 5.2: (a) Two wires intersect to form a T trap. In this figure the current in the T wire has been doubled compared to the cross wire in Figure 5.1 so that its field contribution in the  $xz$ -plane is the same as a cross wire. (b) A contour plot in the  $xy$ -plane at  $z = d = 112.5 \mu\text{m}$  shows the magnitude of the magnetic field. Again, the contours are spaced by 1 G, and the 1 G contour line is at the center of the plot. (c) A contour plot in the  $xz$ -plane at  $y = 0$ . The extra current in the primary wire on the positive  $x$ -axis causes the guide minimum to twist in the  $xz$ -plane as well.

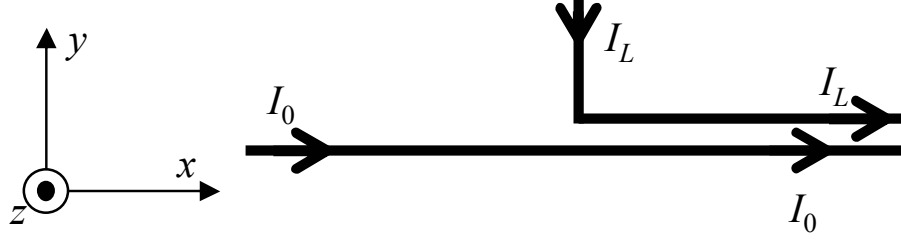


Figure 5.3: Schematic of the L wire coming toward and then running parallel to the primary wire.

twice the current in the T wire is needed to create the same dimple depth as the cross wire.

### 5.1.3 The L Trap

A variation on the T trap is the L trap. To form the L trap, the T wire is replaced with an L wire, where one section of the L wire still lies on the positive  $y$ -axis, but it does not intersect the primary wire. Just before reaching the primary wire, it turns and runs parallel to the primary wire (Figure 5.3). Because the parallel section of the L wire is separated from the primary wire, it can cause the twisting of the trapping potential in the  $xz$ -plane to worsen depending on the distance between the L wire and the primary wire. However, in some cases the L trap is useful because there is no wire intersecting the primary wire, preventing the type of current deviations caused by a T wire as described in Section 4.3.2.

### 5.1.4 The Big Dimple Trap

Instead of having the cross wire intersect the primary wire, we could have it run underneath the primary wire. There are two ways to do this. One is to have a multi-layer atom chip, where electrically isolated layers of conductors are patterned on the chip. The less technologically advanced method is to embed a wire underneath the atom chip in the chip holder [55, 56]. This “big dimple wire” under the chip creates a long,

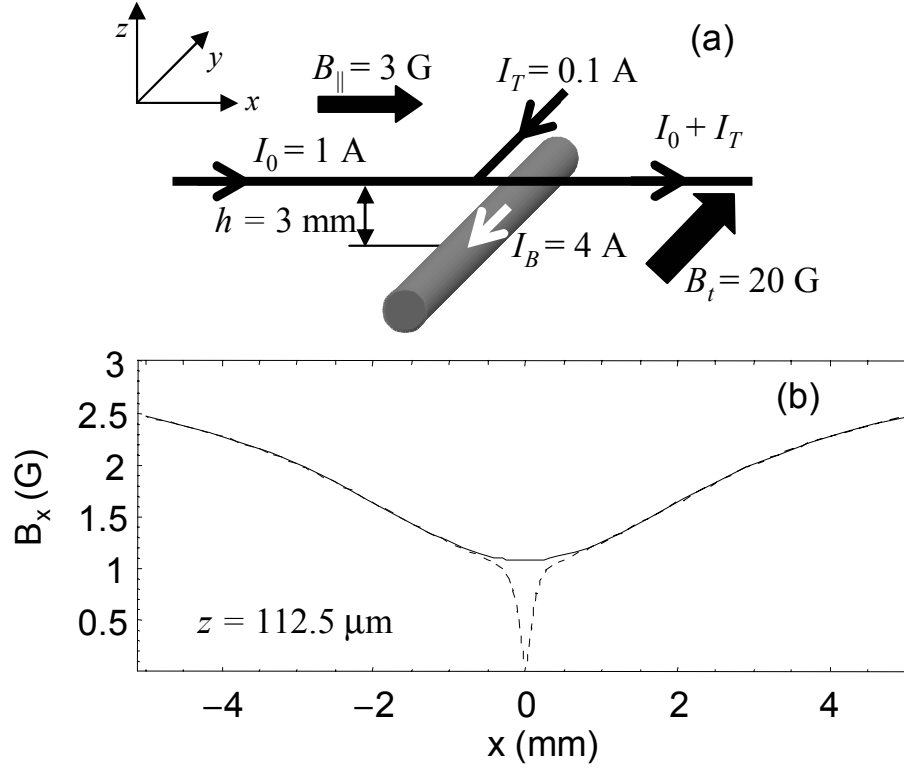


Figure 5.4: (a) Schematic of the big dimple wire set under the atom chip directly below the T wire. (b) Plot of the longitudinal field from the big dimple wire (solid line) and from the big dimple wire and the T wire combined (dashed line).

weakly confining longitudinal potential (Figure 5.4). The combination of the big dimple potential and the T trap can give a long range potential with a tight potential in the center. This is a good example of the flexibility of atom chips.

### 5.1.5 The Z Trap

A common wire trapping technique is the Z trap, which makes use of a Z-shaped wire (Figure 5.5). A Z wire and a transverse bias field create a Ioffe-type trap where the center part of the Z and the transverse bias field provide the radial confinement and the two end wires provide repulsive end caps to contain the atoms longitudinally. The fields from the two end wires add at the center of the Z, so no longitudinal field is required to eliminate the zero at the guide center. Depending on the length,  $l$ , of the

center section of the Z wire, the longitudinal confinement can be changed.

Many research groups have employed the Z trap, because the single current required and the planar geometry of the wire make this trap particularly easy to use. The elongated geometry of the trap allows the transfer of atoms from an optical dipole trap to a Z trap [58]. A macroscopic Z-wire trap has also been loaded directly from a MOT [80], but the Z trap is finding the widest use in loading atoms from a mirror MOT [49, 56]. In a mirror MOT, the surface of the atom chip is coated with a reflective layer, and by reflecting two beams at  $45^\circ$  off the surface, two of the six beams required for a MOT are created by the reflection from the mirror. In this way the MOT is made close to the surface of the atom chip. If one side of the Z wire is flipped to make a U-shape wire, a 3-D quadrupole field is created, which can be used to provide the magnetic field for the mirror MOT. With the atoms in the MOT created by the U-wire, the atoms are transferred to the Z trap by turning off the MOT light and causing the current to flow in the Z wire instead of the U wire.

## 5.2 Loading the T trap

In the trapping region of our atom chip there are a number of wires intersecting the primary wire (Figure 5.6). The intended use of the wires was for making a Z trap, but it turned out that the T trap was a much better trap for our purposes for reasons discussed below. We could potentially create a T trap in any of the crossing wires shown in Figure 5.6. Our first BEC was made with wire B1. We load the T trap at B1 in the following way (Figure 5.7). The atom guide is created by using a 1-A current in the primary wire, a 23-G bias field, and a 3-G longitudinal field. As the atoms are moving onto the chip and into the guide, they are being slowed and focused by the big slowing coil (Section 4.3.2). As the atoms are approaching wire B1, we turn on the anti-Helmholtz coils to decelerate the atoms such that the center of mass of the cloud comes to a stop over B1. While the atoms are still coming to a focus, we

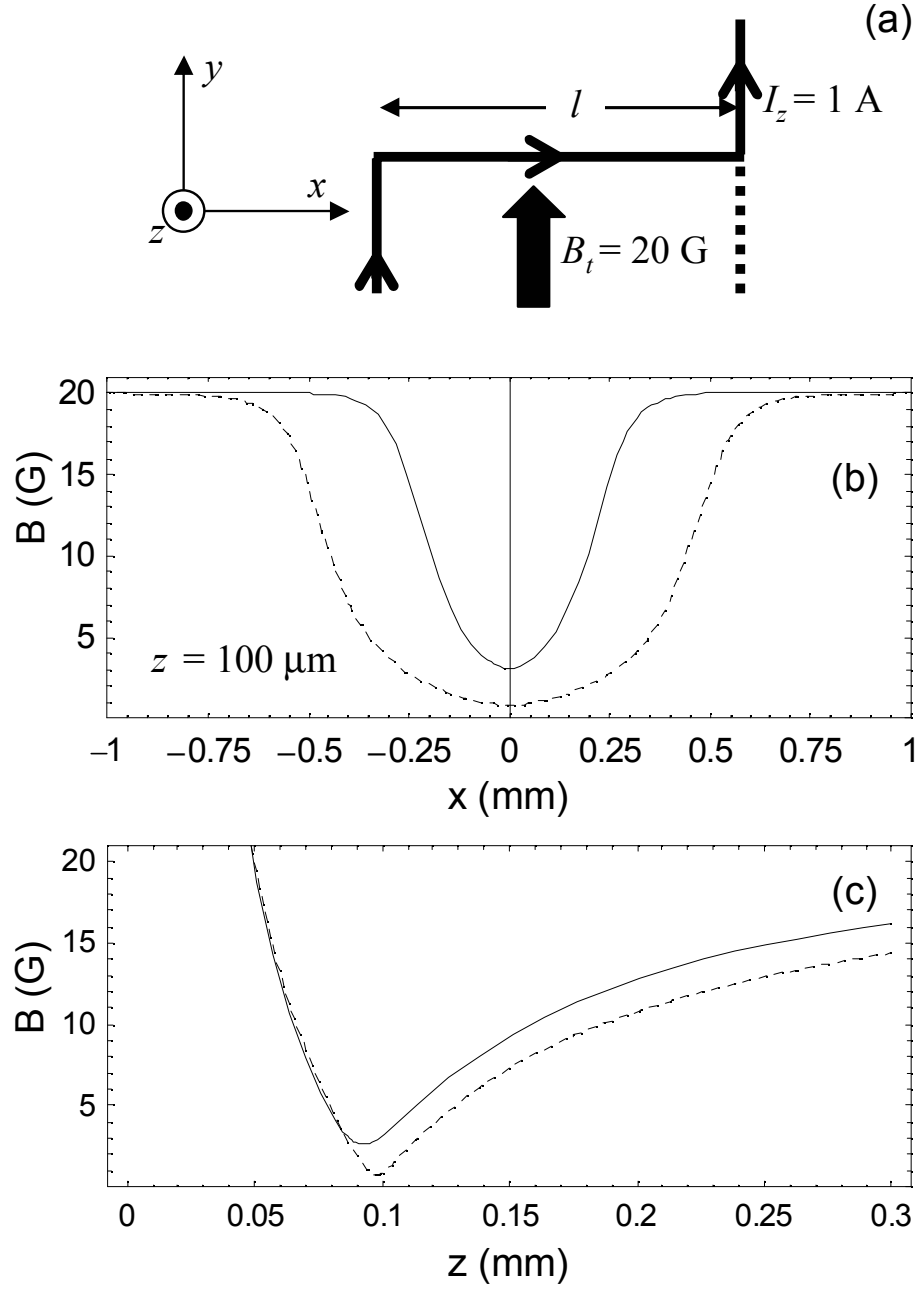


Figure 5.5: (a) Schematic of the Z wire. The dotted line shows the wire to make a U trap. (b) Plot of the total field parallel to the  $x$ -axis above the center of the Z wire at  $z = 100 \mu\text{m}$ . The solid line is for  $l = 0.5 \text{ mm}$ . The dashed line is for  $l = 1 \text{ mm}$ . (c) Plot of the total field along the  $z$ -axis above the center of the Z wire.

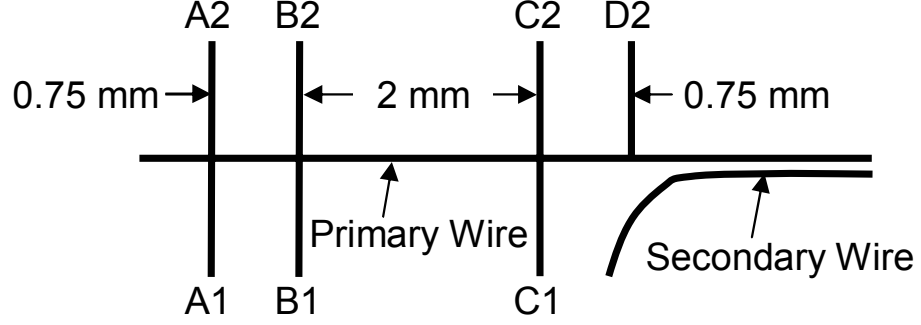


Figure 5.6: Schematic of the wires in the trapping region of our first atom chip.

Table 5.1: Atoms loaded into the Z trap and the T trap are compared.

Condition	Temperature ( $\mu\text{K}$ )	Peak Density ( $\times 10^{12} \text{ cm}^{-3}$ )	Phase Space Density	Number $\times 10^5$	Collision Rate (Hz)
In HIP trap	0.7	6	$8 \times 10^{-2}$	13	100
In coupling region moving at 15 cm/s	5	5	$3 \times 10^{-3}$	13	180
T trap at B1	19	31	$2 \times 10^{-3}$	3	2300
Z trap with B1 and D2	28	0.8	$4 \times 10^{-5}$	0.4	70

slowly ramp down the dimple potential of the T trap by allowing some current from the primary wire to flow into wire B1. Over a period of 200 ms, the current in B1 is ramped to 0.2 A to create a potential with a radial trap frequency of 1800 Hz and an axial frequency of 150 Hz (assuming the harmonic approximation near the minimum of the potential). Figure 5.8(c) shows the atoms loaded into the T trap at B1, and Table 5.1 gives the characteristics of the loaded atoms. Even though the atoms are heating as they are loaded into the trap, the phase-space density is reduced only slightly compared to atoms moving in the guide because the density of the atoms in the T trap is increased. The small decrease in phase-space density and drastic increase in the collision rate give excellent conditions for efficient RF evaporation to make a BEC.

Although we first loaded atoms at B1 to create a BEC, we quickly switched to loading the T trap at D2 because this is the T closest to the waveguide beamsplitter

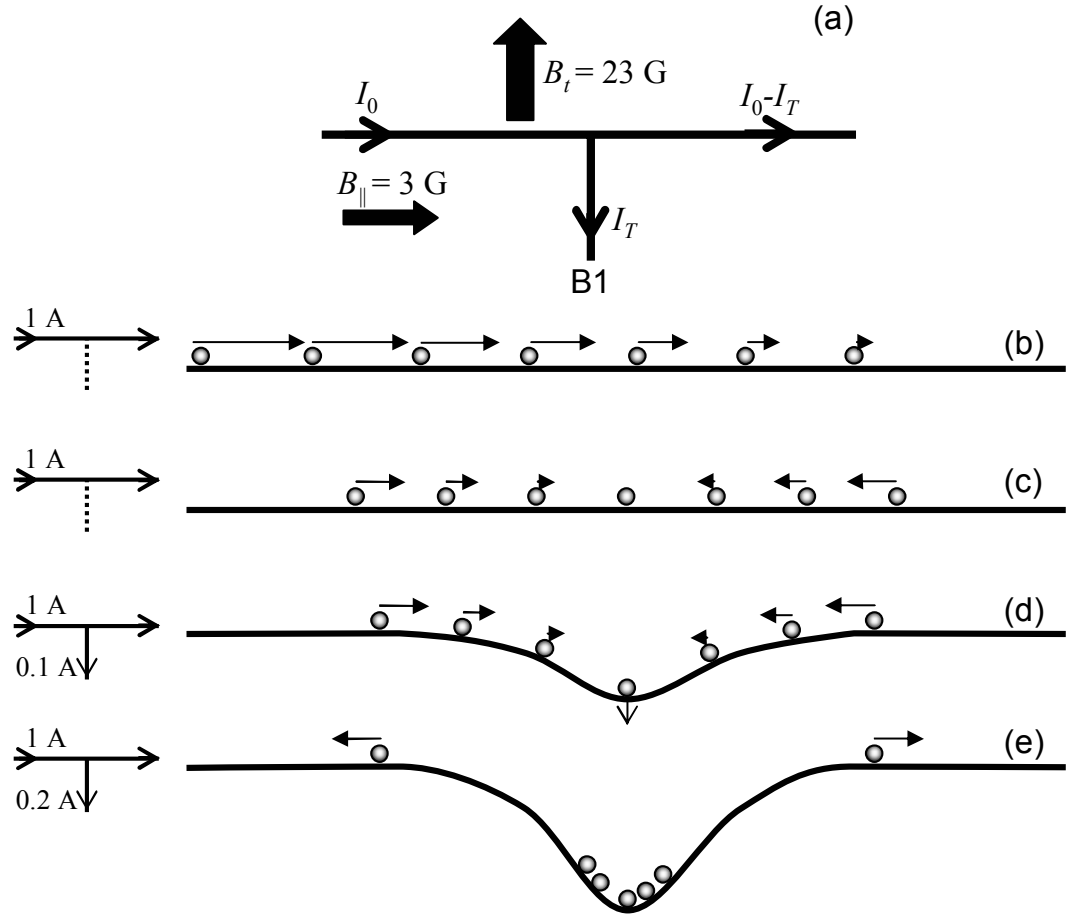


Figure 5.7: Loading the T Trap. (a) A schematic of the wires used for the T trap. (b)-(e) The current in the wires is shown on the left, and the atoms moving in the longitudinal direction are schematically shown on the right. (b) The atoms moving along the guide's longitudinal potential toward the T trap are starting to come to a focus after the big stopping coil is turned off. (c) The AH coils stop the center of mass of the cloud. (d) The current in the T wire is slowly ramped on to form the dimple potential. As the dimple is lowered, the atoms that move into the dimple are trapped and are adiabatically compressed. (e) At its full depth, the dimple traps the cooler atoms while the more energetic atoms leave the dimple and move into the guide.

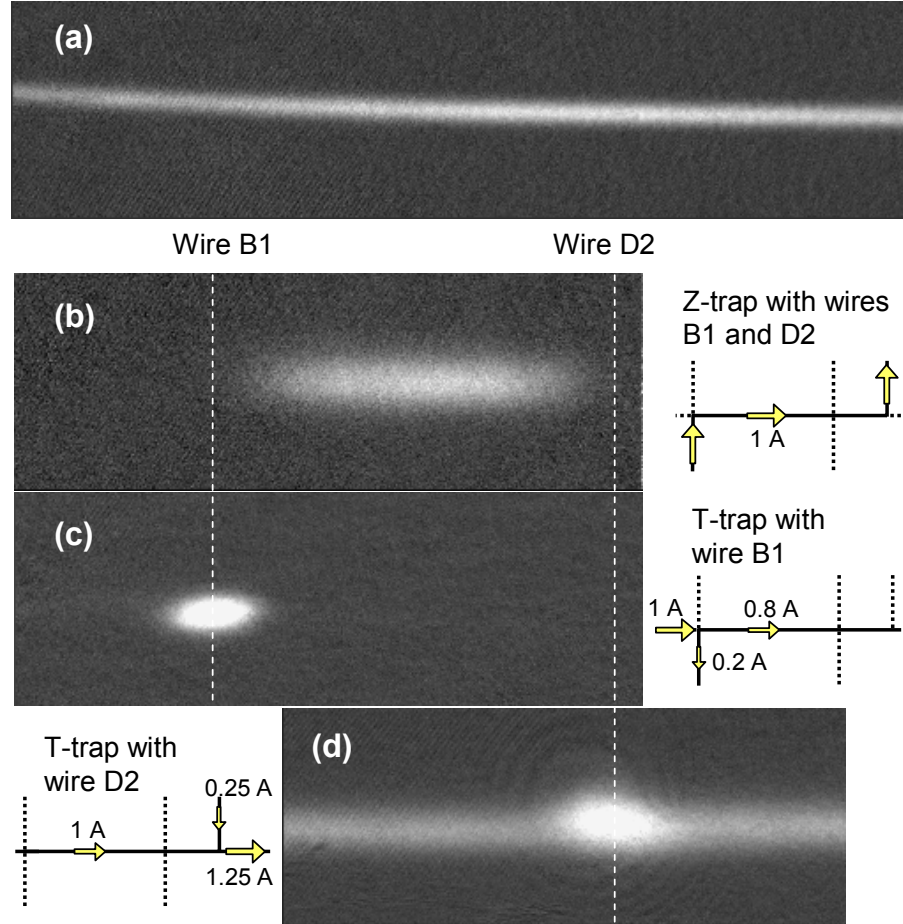


Figure 5.8: The figure shows images of atoms at various points on the chip. For the image the atoms are allowed to expand for  $t_{\text{expand}} = 5$  ms, and the wire pushes the atoms away from the chip for  $t_{\text{push}} = 0.54$  ms. (a) This image shows the atoms in the coupling region just after the big slowing coil has been turned off, and the atoms are beginning to focus. (b)-(d) Atoms in the trapping region of the chip. The vertical dashed lines on the images show where the trapping wires lie above atoms on the atom chip (Figure 5.6). The schematic next to each images shows the currents through the wires in the coupling region for each image. (b) Atoms in the Z trap for 500 ms. (c) Atom in the T trap for 500 ms. (d) This image is taken immediately after the atoms are loaded into the T trap, and there are still atoms in the guide on either side of the T trap.



(Figure 5.6). Wire D2 is a T, not a cross, so it produces a bump in the longitudinal field as described in Section 4.3.2. Thus, a BEC made at one of the crosses would have to have a significant velocity ( $\sim 3$  cm/s) to make it over the bump at D2 and reach the beamsplitter. To load the T trap at D2, we have to shift the center of the stopped thermal atoms from B1 to D2. To do this, we can either reduce the gradient on the AH coils or turn them on at a slightly later time. We find that we can load atoms into the T trap at D2 with approximately the same properties as those loaded at B1.

### 5.2.1 Loading the Z Trap

We had originally considered the Z trap for trapping atoms on the chip, but it turns out that we have not been able to successfully load this trap with sufficiently high number, phase-space density, and collision rate. We load the trap in the following way (Figure 5.9). We have 1 A in the primary wire, and this current exits the primary wire at wire D2. This creates a repulsive potential for atoms moving in the guide. Again, we shut off the big slowing coil and ramp on the AH coils to stop the cloud. During the stopping, the leading section of the cloud has already been repulsed by wire D2 so the leading section is accelerated by the AH coils back toward the evaporation chamber. Then, we ramp on the current in B1 to 1 A while ramping off the current in the primary wire to complete the Z trap. Because the current in B1 creates a repulsive potential, the atoms outside the Z trap cannot move into the Z trap while B1 is ramped on, whereas the T trap captures most of the atoms that come into the range of its potential. This significantly reduces the number of atoms trapped in the Z trap. For the data in Table 5.1 and the image in Figure 5.8(b), wire B1 is ramped on and the primary wire is ramped off in 15 ms. We have observed that slowly ramping on the Z trap over 100–200 ms increases the phase-space density but reduces the number of atoms trapped, while slowly ramping on the T trap does not significantly affect the final number of atoms trapped.

Overall, loading of the Z trap is significantly worse than loading the T trap (Table 5.1). Of great concern is the low number and collision rate of the loaded atoms, and we have never been able to achieve BEC with the Z trap. We could perhaps improve the loading of the Z trap by starting with a straight guide and then ramping up both sides of the Z trap at the same time. In this way, the leading section of the cloud is not repulsed by D2 while the cloud is being stopped, but we still have the problem of being able to collect only the atoms initially within the Z trap. We believe that the main advantage of the T trap is the ability of the trap to continually capture atoms from the guide as it is being ramped on, and we can capture nearly a quarter of the atoms delivered from the HIP trap in the T trap.

### 5.3 BEC on the Chip

Once a sample of atoms is loaded into the T trap with sufficient number, density, and collision rate, we apply the techniques of RF evaporative cooling [81] to achieve BEC. Forced RF evaporation selectively removes the highest energy atoms in the trap by flipping the spin of these atoms to an untrapped state. The Zeeman splitting of the magnetic sublevels of the hyperfine ground state increases with increasing magnetic field (Figure 3.1), and the high-energy atoms spend more time at the edge of the cloud where the magnetic field is the greatest compared to the low-energy atoms. We can drive transitions between the magnetic sublevels for the high-energy atoms by applying an RF field that is resonant with the Zeeman energy splitting at the high magnetic fields. Thus, the highest-energy atoms are removed from the trap. As the average energy of the cloud is reduced, we sweep the RF to lower and lower frequencies in order to continually cool the cloud. We use the logarithmic sweep function of our RF synthesizer to continually lower the RF such that equal time is spent in each decade of frequency. By setting the start frequency, the stop frequency, and the total time for the sweep, we determine the evaporation trajectory.

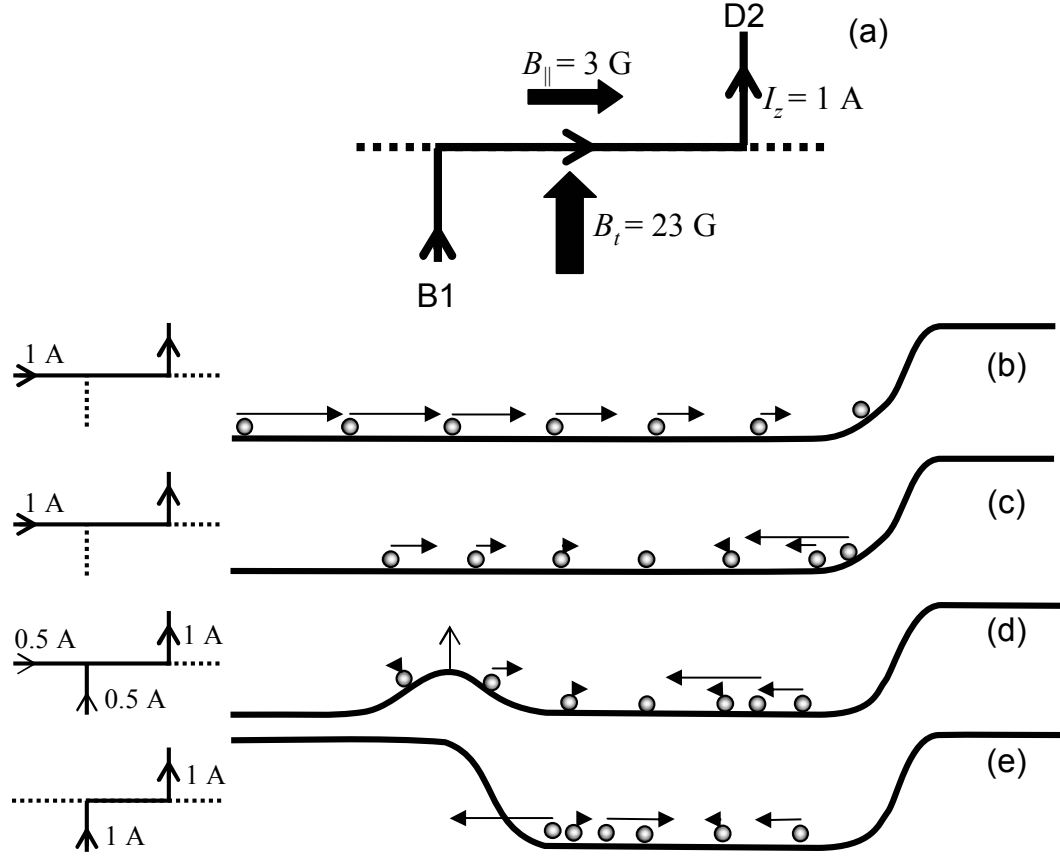


Figure 5.9: Loading the Z Trap. (a) A schematic of the wires used for the Z trap. (b)-(e) The current in the wires is shown on the left, and the atoms moving in the longitudinal direction is schematically shown on the right. (b) The atoms are moving along the guide's longitudinal potential toward the Z trap. The “downstream” side of the Z is at full strength, and any atom that approaches this repulsive potential is reflected. (c) The AH coils stop the center of mass of the cloud, but any atom reflected by the downstream side of the Z trap is accelerated to a higher speed. (d) The current in the upstream wire is ramped on to form the Z trap. Because the upstream side of the Z trap forms a potential barrier low energy atoms cannot continue to move into the Z trap as it is being ramped on. (e) To finally form the Z trap, all of the current flows in the Z wire only so there is no guiding potential on either side of the Z trap, and the depth of the potential is set by the transverse bias field. Thus, the trap depth is too high to allow the high energy atoms to leave the trap.

### 5.3.1 Coupling the RF to the Atoms

For the evaporation we need to apply RF radiation to the atoms. For evaporation in the HIP trap we have a small loop of wire outside the glass cell, and an oscillating current to the loop creates a small oscillating magnetic field to drive transitions in the atoms. Because the application chamber is large and made of stainless steel, it would be difficult to couple sufficient RF power to the atoms with a coil outside the chamber. Therefore, we use a wire inside the application chamber to supply the RF. To apply an oscillating magnetic field perpendicular to the quantization axis of the atoms (the longitudinal field), we can use either the bias sheet or the primary wire. By applying RF to the primary wire, we can evaporate the atoms, but for some unknown reason the DC current in the wire changes when the RF circuit is connected to the wire. We can achieve equally good evaporation, however, by coupling RF onto the bias sheet without any adverse effects on the circuitry supplying the DC current to the bias sheet or the wires on the chip. We apply the RF to the bias sheet through a capacitive connection, and we do need to take care that the connection is sound. Our original connectors were flexible and not shielded, and the coupling efficiency of the RF into the bias sheet varied dramatically as the wires to the connectors were shifted, causing nearly 100% number fluctuations in the BEC. By making the RF capacitive connection to the bias sheet inside of a small box such that the connectors could not move, we achieved a stable coupling.

### 5.3.2 BEC in the T Trap

Our first BEC was made in the T trap below wire B1. Because of the high collision rate of the atoms loaded into the trap (Table 5.1), we can perform the evaporation in only 143 ms by sweeping the RF from 2.5 MHz to the stop frequency of 0.93 MHz, approximately 200 kHz above the bottom of the trap. After the evaporation we have

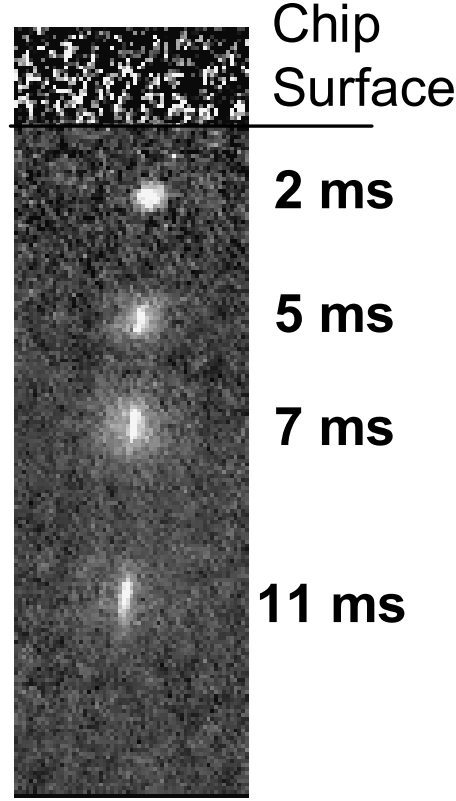


Figure 5.10: Several absorption images of the BEC as it expands out of the trap. A clear bimodal distribution is observed as the cloud expands where the anisotropically expanding BEC is observed inside the isotropically expanding thermal cloud.

a BEC with slightly less than  $10^4$  atoms. A BEC is first observed at a temperature of  $1.2 \mu\text{K}$  in good agreement with the calculated critical temperature of  $1.3 \mu\text{K}$  for 47000 atoms. Figure 5.10 shows a series of time-of-flight images after the BEC has been released from the T trap. The thermal cloud around the BEC expands isotropically while the BEC expands anisotropically, a clear signature of a quantum degenerate bose gas.

For releasing the atoms to the atom waveguide beamsplitter, we switched to making a BEC in a T trap made by wire D2. In using this T trap we worked to increase the number in the BEC. By optimizing the focusing and stopping with the big slowing coil and the AH coils, by increasing number and temperature of the atoms sent to the atom chip, and by decreasing the time to ramp on the current in T wire

to 70 ms, we can load 3.5 times more atoms into the T trap. We also improved the evaporation procedure. The T trap is loaded with 0.25 A in D2 and 1.2 A in the main wire, and the trap frequencies are 1990 Hz and 160 Hz for the radial and axial frequencies respectively. Again, the transverse and longitudinal bias fields are 23 G and 3 G respectively. We evaporate from 4 MHz to 1.7 MHz in 590 ms. We then ramp the current in D2 to 0.06 A to reduce the trap frequencies to 1210 Hz and 104 Hz. This reduces the peak density of the cloud by about a factor of two. The density of the condensate in these traps is on the order of  $10^{15}$  atoms per cubic centimeter, and at this density the three-body recombination rate is significant [82]. Decreasing the density by a certain amount reduces the three-body loss rate by that amount squared. Decompressing the trap raises the trap bottom from 0.8 G to 2.36 G, and we start the second evaporation ramp at 2.5 MHz and 170 ms later end at 1.7 MHz to achieve a BEC. With all of these improvements, we are able to increase the number of atoms in the condensate to 15000–25000.

### 5.3.3 Two BECs on the Chip

As an easy demonstration of the versatility of atom chip technology, we can load two T traps simultaneously and evaporatively cool both atomic samples to make two BECs. To do this, we focus and stop the atoms in the same way we do for loading the T trap at D2, but we run 0.21 A through wire C2 in addition to the 0.25 A through wire D2 (Figure 5.11). With the atoms loaded into the traps, we do a single RF sweep in 400 ms to make two BECs. We only need to make sure that the bottom of the two T traps are the same so that the evaporation cuts to the same final depth in both traps. The currents shown in Figure 5.11(b) are experimentally determined to give the same trap bottom. The current in D2 is larger mainly because the trap center is farther away from the chip than the T trap at C2 because of the larger current in the primary wire at the D2 intersection. The number of atoms in each BEC is approximately 7000. We

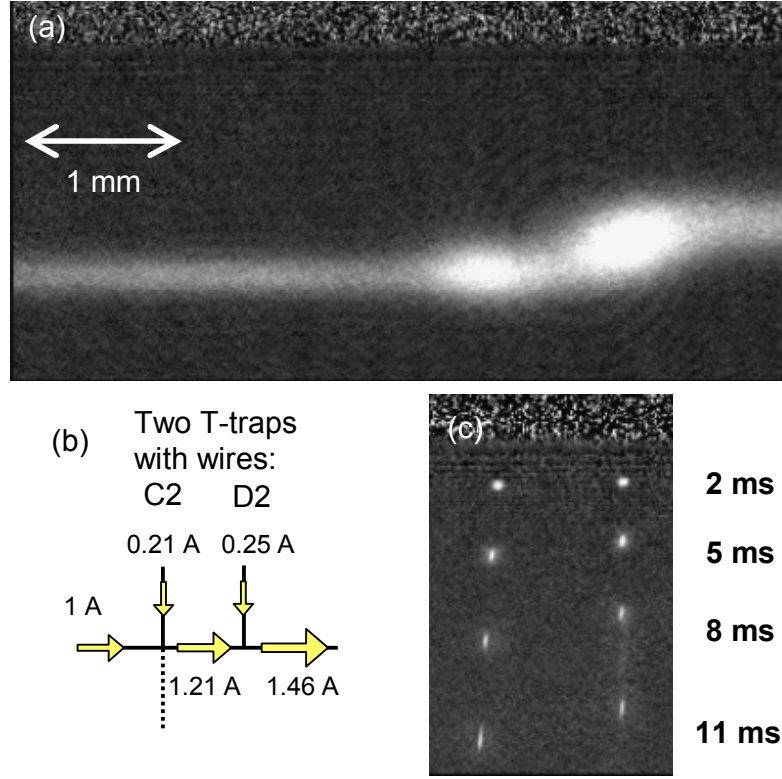


Figure 5.11: (a) This image shows atoms loaded into the two T traps while some of the atoms remain in the guide on both sides of the T traps. The two dimples are separated by 0.75 mm. The cloud is twisted because the current in the bias sheet and in D2 is switched off 500  $\mu$ s before the current in C2 and in the primary wire. Thus, the atoms are pushed unevenly. If all of the currents on the chip were shut off at the same time, the cloud would not appear significantly twisted. The atoms expand for 5 ms. (b) The schematic of the wires shows the currents in each wire. (c) A sum of several images showing the two BECs expanding as they move away from the chip. The two BECs are pushed away by the primary wire for 140  $\mu$ s.

observe a long-term drift in the relative number of atoms in each T trap as the focusing and stopping conditions slowly change with time.

#### 5.3.4 BEC in the Big Dimple Trap

After seeing the success of the T trap, we speculated that we could trap more of the atoms in the guide if we created a longer-range dimple potential for the longitudinal confinement. With more of the transferred atoms trapped, we should increase the number in the BEC made on the chip. We implemented this idea on our second atom

chip by imbedding a wire 3.28 mm under the atom chip in the atom chip holder. This “big dimple wire” runs perpendicular to the primary wire as shown in Figure 5.12(a). Also implemented on this chip is an L-shaped wire vertically aligned with the big dimple wire to create an L trap. The combination of these wires creates a long-range potential for capture and a short-range, more tightly confining trap to create a higher collision rate for evaporation.

In using this combination trap, we do a series of current ramps and RF sweeps (Figure 5.12). As usual, the atoms are stopped and focused with the big slowing coil and the AH coils. Over 100 ms the big dimple wire is ramped on to 4 A. This trap captures almost all of the atoms in the guide, and we load  $3 \times 10^6$  atoms at a phase-space density of  $1.5 \times 10^{-3}$ . This is ten times more atoms loaded than in the T trap at the same phase-space density (compare to Table 5.1). For the next 150 ms we ramp on the L wire to 0.2 A. Then, we start the RF evaporation at 4.5 MHz and sweep to 1.4 MHz over 800 ms. This evaporates virtually all of the atoms in the big dimple potential, and with these atoms gone, we can ramp off current in the big dimple wire over 40 ms, which relaxes the radial confinement. In the decompressed trap, we perform the final RF sweep, going from 2 MHz to 1.65 MHz in 1000 ms, to make a BEC. With the improved starting conditions, the number of atoms in the BEC is  $7\text{--}8 \times 10^4$ , a significant improvement over the lone T trap. The evaporation takes longer in this combination trap because we chose to reduce the radial confinement compared to previous traps, reducing the collision rate. Throughout the evaporation the collision rate varies from 500 Hz to 1500 Hz.

## 5.4 Conclusions

Loading the guided atoms into a trap was the main challenge of making of BEC on the atom chip. By trying several different trapping techniques and optimizing their use, we have been able to improve the loading process. In the initial experiments with the Z



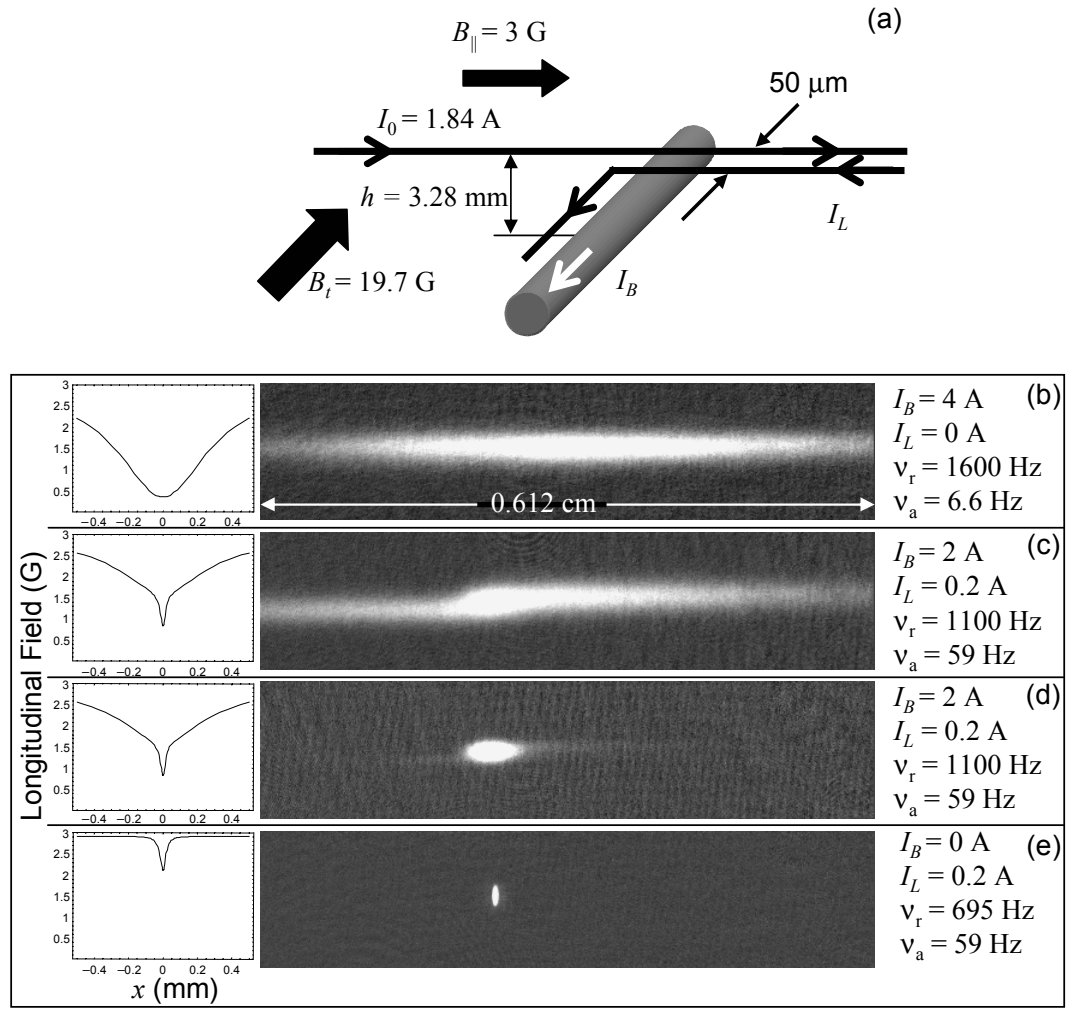


Figure 5.12: (a) The schematic shows the wires on the chip with the big dimple wire directly below the L wire. The L wire comes toward the primary wire and then runs parallel to the primary wire  $50 \mu\text{m}$  away. (b)-(e) The plot shows the confining longitudinal potential, and the image shows atoms in that potential. The current in the big dimple and L wire and the calculated radial and axial trap frequencies are shown on the right. For (b)-(d) the atoms are allowed to expand for 5 ms and are pushed away from the chip by the primary wire for 0.54 ms. For (e) the atoms expand for 15 ms and are not pushed by the primary wire. (b) The atoms are loaded into the big dimple trap. (c) The atoms are in the combination trap using both the big dimple wire and the L wire. (d) The atoms are almost all in the L trap after the atoms in the wings have been evaporated away. (e) A BEC of 70,000 atoms.

trap, we were able to load only  $4 \times 10^4$ , and on our second atom chip, we improved the loading by more than a factor of 100 by using the big dimple wire. After RF evaporation we obtain a BEC with 70,000 atoms. Now that we have a BEC on our atom chip, we can begin to explore the properties of our atom waveguide beamsplitter.

## Chapter 6

### The Atom Waveguide Beamsplitter and Other Experiments

The first step toward realizing an atom waveguide interferometer is to develop a single-mode source ready for release into a waveguide beamsplitter. As described in the previous chapter, we have accomplished this task by producing a BEC on our atom chip. The next step is to test the beamsplitter with this source. As a preliminary step to beamsplitting, we show that the atoms do propagate in the lowest transverse mode of the guide as they move toward the beamsplitter. We also observe a number of effects when the atoms are moved toward the chip surface. More specifically, the current within the wires on the chip produces adverse effects that limit the lifetime of the trapped atoms and inhibit propagation of the atoms in the guide and through the beamsplitter. Nevertheless, we are able to send a BEC through the beamsplitter, and we observe that the surface effects do not allow the coherent splitting of the atomic wavefunction. We study how the surface effects degrade the beamsplitter's performance, and propose ways to reduce the surface effects.

#### 6.1 Single Mode Propagation

For the atom waveguide beamsplitter to work properly, the atoms need to be propagating in a single transverse mode of the guide before they enter the beamsplitter. Certainly, the easiest mode for a BEC to populate is the lowest mode of a guide since a BEC is formed in the ground state of our microtrap. A clear signature of the number of

modes populated in the guide is the transverse size of the cloud. If the cloud populates only the lowest mode, its in-trap transverse size should be that of the harmonic oscillator ground state. In measuring the cloud size, we compare the measured rms width of the cloud in the radial direction,  $\sigma_r$ , to the radial harmonic oscillator length, which is given by

$$x_o = \sqrt{\frac{\hbar}{2m_{Rb}\omega_r}} \quad (6.1)$$

where  $\omega_r$  is the radial frequency of the guide. If  $\sigma_r$  and  $x_o$  are equal and the cloud is not sloshing radially, we know that the atoms are propagating in the lowest mode of the guide.

This experiment is performed using our first atom chip, and the T trap is made using wire D2 (Figure 5.6). For this experiment, we first make a BEC in a T trap. Initially, the current in the primary wire,  $I_1$ , is 1.21 A, and the current in D2 is 0.06 A, and we apply a 22.5 G transverse bias field and a 2.96 G longitudinal field. To release the atoms out of the T trap and into the guide, we simply reverse the direction of the current in the T wire to -0.04 A over 10 ms, and the longitudinal dimple potential of the trap turns into a bump (Figure 6.1(b) and (c)). Because of the asymmetry in the T trap's potential (Figure 4.10), the atoms are accelerated down the waveguide toward the beamsplitter, moving at a speed of 3 cm/s. While we are ramping the current in wire D2, we can also ramp the longitudinal field,  $B_{||}$ , to change  $\omega_r$ .

Initially, the radial size of the BEC is larger than the harmonic oscillator size because of the mean-field interaction. As the BEC propagates, it expands longitudinally. As the density of the cloud decreases, so does the mean-field energy, allowing the radial size of the cloud to asymptotically approach  $x_o$ . Figure 6.2 shows how the radial and axial sizes of the BEC vary as it expands. For this data, the current in the primary wire on the beamsplitter side of D2 is 1.17 A, and we decrease  $B_{||}$  to 0.6 G, which gives a radial-guide frequency of  $\omega_r = 2\pi \times 2.55$  kHz. For this frequency the harmonic oscillator

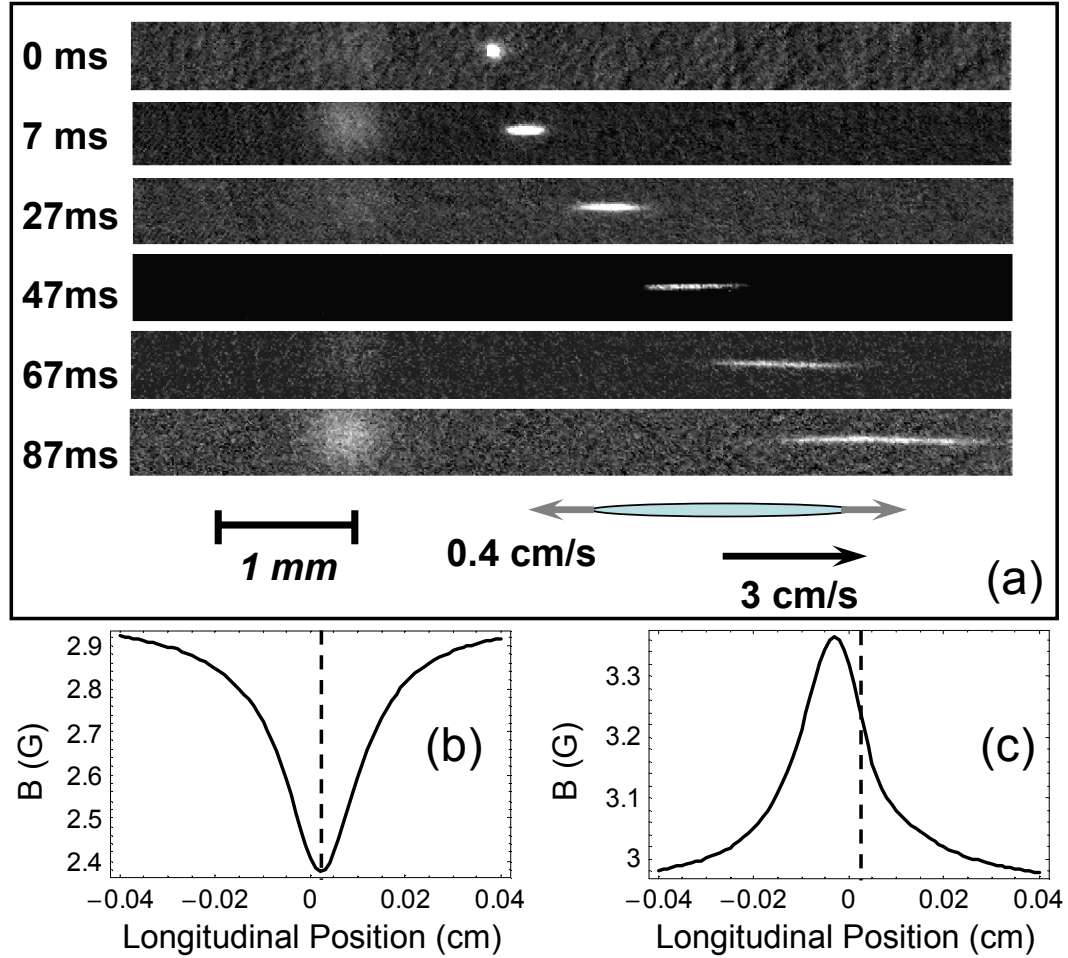


Figure 6.1: (a) A series of expansion images showing the BEC as it is released from the T trap at D2. The cloud is traveling at 3 cm/s, and the rms axial size is increasing at 0.4 cm/s. (b) The plot shows the calculated longitudinal confinement of the atoms before they are released. The longitudinal frequency is 104 Hz with a current of 0.06 A in wire D2. (c) When the current is reversed to -0.04 A, the atoms are now pushed by the T wire. Due to the deviation in the primary wire current in the T, the bottom of the dimple potential is offset toward the beamsplitter compared to the peak of the bump, causing the atoms to move toward the beamsplitter region of the chip. (see also Figure 4.10)

size is  $0.15 \mu\text{m}$ . Figure 6.2(b) shows that the radial size of the BEC does approach  $x_o$ .

To further understand the expansion, we calculate the size to the BEC as it expands into the guide following the work by Stickney and Zozulya [83]. In the hydrodynamic approximation, they solve the Gross-Pitaevskii equation, deriving an analytical solution for the axial size as a function of time

$$\left(b_a(\tau)^{3/4} + \frac{3}{2}b_a(\tau)^{1/4}\right) \left(b_a(\tau)^{1/2} - 1\right)^{1/2} + \frac{3}{2}\ln \left[b_a(\tau)^{1/4} + \left(b_a(\tau)^{1/2} - 1\right)^{1/2}\right] = 2\tau \quad (6.2)$$

where  $b_a$  is the dimensionless axial size of the BEC normalized to its initial size,  $\tau = \omega_a t$ , and  $\omega_a$  is the axial frequency. The dimensionless radial size is approximately

$$b_r(\tau) \approx b_a(\tau)^{-1/4} \quad (6.3)$$

The atoms are released from the T-trap with frequencies of  $\omega_r = 2\pi \times 1.21 \text{ kHz}$  and  $\omega_a = 2\pi \times 104 \text{ kHz}$ . Using Equation 6.2, we find that the predicted axial expansion is approximately two times faster than observed in Figure 6.2(a). The expansion slowed because the axial confinement is not instantaneously switch off. The T trap is ramped off over 10 ms, and the potential that accelerates the BEC has a curvature which gives a weak confinement in the moving frame of the BEC. By choosing an effective initial axial frequency of 20 Hz, we find that Equation 6.2 agrees well with the data. Given the axial expansion, we can use Equation 6.3 to calculate the radial expansion. By scaling the initial calculated size to the initial measured size, we see that during the beginning of the expansion the radial size decreases according to Equation 6.3. However, after 40 ms the hydrodynamic approximation is no longer applicable, and the contraction in the radial size slows and asymptotically approaches  $x_o$ . The expansion shown in Figure 6.2(b) demonstrates that at least 90% of the atoms populate the lowest mode guide. However, when we measure the population of the lowest mode for lower guide frequencies we find that it can be as low as 45%. We still need to explore how we can achieve single mode propagation over a broad range of guide frequencies, but this

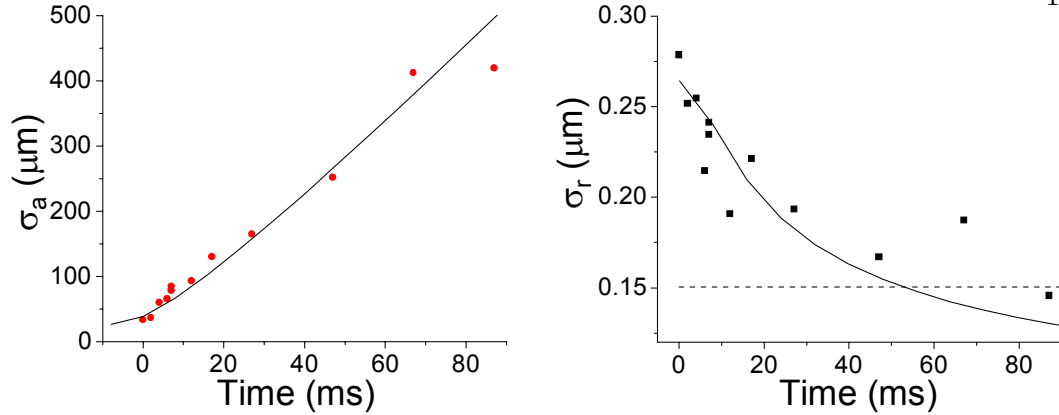


Figure 6.2: The expansion of the BEC into a guide with a frequency of  $\omega_r = 2\pi \times 2.55$  kHz. (a) The plot shows the rms axial size of the cloud as a function of time. The line is a calculation of the expansion in the hydrodynamic approximation. (b) The plot shows the inferred in-trap rms radial size as the cloud expands axially. After 60 ms the cloud approaches the harmonic ground state size (dashed line). The solid line shows the hydrodynamic calculation.

source has a sufficient population in the lowest mode for the beamsplitter experiments described below.

## 6.2 Surface Effects

The close proximity of the atoms to the surface of the atom chip affects the atoms in several ways. The two major effects come from the current in the wires: a spatially irregular current flow and a broad spectrum of noise on the current. At this point we do not see any effect from the chip's aluminum-nitride substrate unless we are very close to it. We observe that atoms that come within less than one micron from the surface are lost from the trap due likely to the van der Waals' interaction. However, for most atom-chip applications the dielectric surface does not play a role, while the effects caused by the conductors need to be carefully considered.

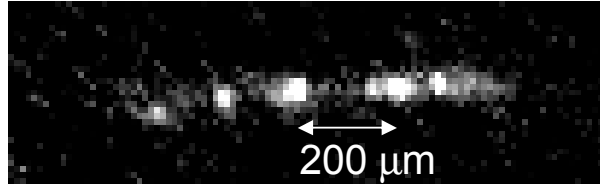


Figure 6.3: A fragmented BEC propagating in the guide  $37\ \mu\text{m}$  from the wire.

### 6.2.1 Fragmentation of the Cloud

Fragmentation occurs on an atom chip when atoms confined in an atom guide or an elongated trap break up into sections along the longitudinal dimension (Figure 6.3). We first observed this effect when stopping a  $1.4\text{-}\mu\text{K}$  cloud on the chip (Figure 4.9(c)), but the fragments were not very pronounced. Later, we observed the effect clearly as we released a BEC into the guide and allowed it to propagate toward the beamsplitter in the primary waveguide (Section 6.1). For this experiment the atoms propagate in the guide  $100\ \mu\text{m}$  below the wire; then we decrease the current in the primary wire to bring the atoms closer to the wire. As we move the atoms closer to the wire, we begin to observe the fragmentation  $80\ \mu\text{m}$  from the wire, and the closer the atoms are to the wire, the more pronounced the fragmentation effect becomes (Figures 6.3 and 6.4). At a distance of  $60\ \mu\text{m}$  we can probe how the cloud fragments at different points on the chip, and we find that the atoms fragment with a periodicity of  $150\text{--}200\ \mu\text{m}$  at this distance. Because the atoms are moving, the positions at which the atoms bunch up must be the location of a potential barrier of some kind.

The Zimmermann group was the first group to observe the fragmentation effect on an atom chip, and they experimentally explored how a BEC would break up into multiple fragments where the number of fragments depended on the distance from the surface of the chip [84]. With a  $1\text{-}\mu\text{K}$  cloud  $150\ \mu\text{m}$  away from the wire, they observed a longitudinal potential with a  $300\text{-}\mu\text{m}$  period. With a BEC  $50\ \mu\text{m}$  away from the surface, they observed multiple fragments spaced by  $50\ \mu\text{m}$ . Most other groups working with



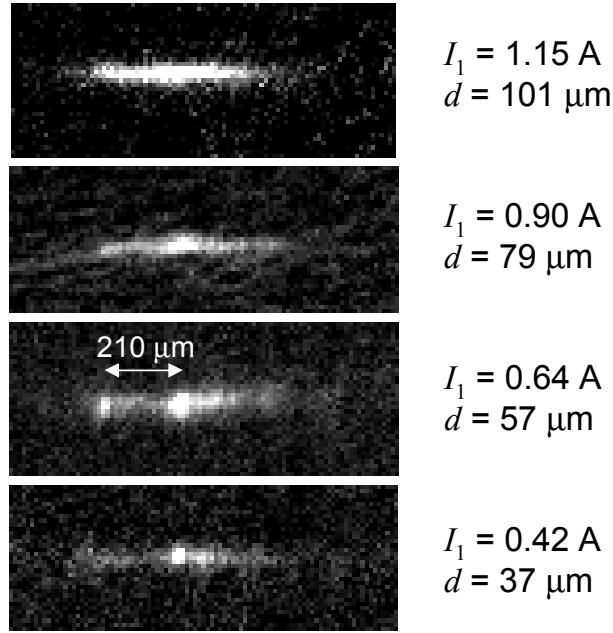


Figure 6.4: This series of images shows how the cloud fragments as we move it closer to the primary wire. Before the images are taken, the cloud is ramped from  $100 \mu\text{m}$  to its final position over 10 ms and is then released and allowed to expand for 8 ms.  $B_t = 23 \text{ G}$  and  $B_{\parallel} = 3 \text{ G}$ .  $I_1$  is the current in the primary wire and  $d$  is the distance from the center of the wire.

atom chips have observed this fragmentation effect [55, 59], and others [85] that have not observed the effect likely do not have sufficient atom number to be sensitive to it.

Two experiments performed in the Ketterle group and the Zimmermann group show that the origin of the fragmentation is from a magnetic field produced by the current-carrying wire, giving rise to a corrugated longitudinal potential. The Ketterle group has the advantage that they can trap the atoms near the surface of the chip with both an optical dipole trap or the magnetic microtrap on the chip [86]. When the atoms are confined optically, the cloud is not fragmented, but when the atoms are confined in the magnetic trap at the same distance from the chip, the cloud becomes fragmented. The Zimmermann experiment measures the longitudinal position of the fragments relative to the chip with the current in the microfabricated wire flowing in two different directions [79]. For a given direction of the current, the atoms are fragmented

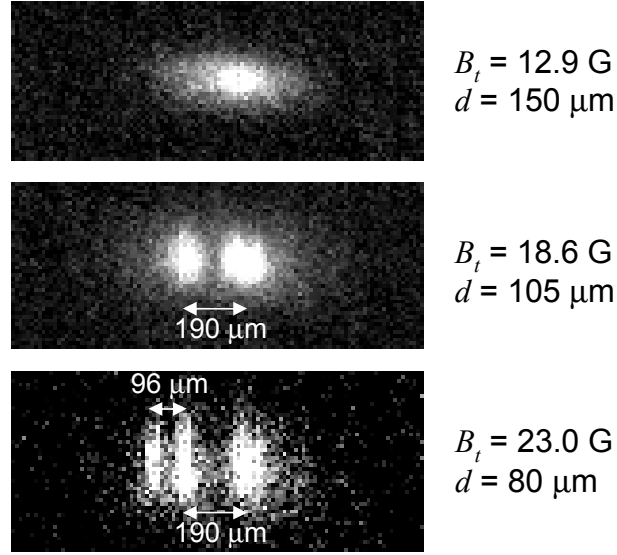


Figure 6.5: This series of images shows the fragmentation of a BEC as we move it closer to the primary wire by increasing  $B_t$ . The atoms are longitudinally confined by the big dimple wire (Section 5.3.4).  $I_1 = 1$  A and  $B_{\parallel} = 3$  G.

periodically. When the current in the wire is reversed while a longitudinal bias field (parallel to the wire) is maintained in the same direction, the periodic pattern of atoms is shifted by a half period, indicating that what had been a bump in the corrugated longitudinal potential has turned into a dip. The Ketterle experiment shows that the fragmentation is caused by current flow in the wire on the chip, and Zimmermann experiment shows that the corrugated potential is magnetic in origin. This magnetic field adds to the longitudinal bias field. Thus, the current is creating a spatially varying longitudinal field, which can occur if the current is not flowing straight down the wire but deviates from side to side. Perhaps, these small current deviations are caused by impurities in the wire or shape deviations in the wire (the wire is not perfectly straight). Reference [79] speculates further on the origins of the corrugations.

On our second atom chip we have been able to better characterize the fragmentation. On this chip we can make an elongated trap with the big dimple wire embedded under the chip (Section 5.3.4). With the big dimple wire providing a longitudinal fre-

quency of 5.5 Hz and 1 A in the primary wire, we can vary the distance of the BEC to the wire by changing  $B_t$ . Figure 6.5 shows how a BEC fragments as we vary the distance. At a distance of 155  $\mu\text{m}$  the cloud is a single condensate, and at 120–130  $\mu\text{m}$  the cloud splits into two BECs. As we move the cloud to 90  $\mu\text{m}$  below the wire, it splits into three fragments. The closer we move the atoms to the wire the shorter the periodicity of the fragments becomes. If a BEC in the corrugated potential is split, then the height of the corrugations must be higher than the chemical potential of the condensate. Given the chemical potential of the condensate, a lower bound on the height of the corrugations can be calculated. We observe that at a distance of 120  $\mu\text{m}$ , the chemical potential of the BEC is  $k_B \times 200 \pm 75$  nK.

Several other groups have also been able to measure the depth of the corrugation for their respective experiments, as shown in Table 6.1. However, the results are for a wide range of experimental conditions, and it is difficult to compare the results. The Zimmermann group has empirically determined a functional form for the depth of the corrugated potential

$$U = \frac{C m_F g_F j w}{d^2} \quad (6.4)$$

where  $U$  is measured in Joules,  $C$  is a scaling factor to be experimentally determined,  $m_F$  is the magnetic quantum number of the atom,  $g_F$  is the Lande  $g$ -factor,  $j$  is the current density in the wire,  $w$  is the width of the wire (for a circular wire,  $w$  is the radius), and  $d$  is the distance from the atom cloud to the surface of the wire, not the center of the wire [79]. They have compared Equation 6.4 to experimental results from both a  $30 \times 2 \mu\text{m}^2$  microstructure wire on a substrate and an ordinary wire 90  $\mu\text{m}$  in diameter. They find that Equation 6.4 successfully describes their data if  $d$  is measured from the surface of the wire, suggesting that fragmentation is due to an effect from the wire's surface. For all of their data they find  $C \simeq 5 \times 10^{-42} \text{ m}^3 \text{ J/A}$ . Using Equation 6.4, we can compare the fragmentation from several groups by calculating  $C$  for the

various conditions (Table 6.1). Our results give the lowest  $C$ , and at this point we do not have an explanation for this (but we are thankful). We suspect that the materials and fabrication techniques used affect the depth of the corrugations produced by the current. Given the widely varying experimental conditions, it is remarkable that all of the  $C$ s are within an order of magnitude, and the agreement reinforces the validity of the functional form of Equation 6.4.

By knowing the depth of our potential, we can estimate the amount the current needs to deviate within the wire to produce this field. We measure the depth of the corrugated potential to be 200 nK which corresponds to a 6 mG longitudinal field. We model the current deviations with infinitely thin wire segments that are placed end to end (Figure 6.6(a)). Thus, we assume that the center of current, the average position of the current within the wire, makes a small deviation from the physical center of the wire. A single deviation creates both a dip and a bump in the longitudinal potential (Figure 6.6(b)), and the peak-to-peak amplitude of the corrugation is the well depth we measure in the experiment. To achieve an amplitude of 6 mG at a distance of 125  $\mu\text{m}$  from the center of the wire, the deviation can have a length  $l = 0.4$  mm and a width  $h = 0.06$   $\mu\text{m}$ . This width is small compared to the 20  $\mu\text{m}$  width of our wire, and it is easy to imagine that our wire contains shape imperfections on the 0.1  $\mu\text{m}$  scale. Indeed, evaluation of the microstructure wires with an optical microscope shows that the edges of the wires show features 1  $\mu\text{m}$  or less, but the features' lengths are approximately 10  $\mu\text{m}$ . To create corrugations with a length of 100–200  $\mu\text{m}$  as observed in the experiment, the wire must have deviations in width that occur on this length scale, but the shorter period deviations make it difficult to observe deviations 200  $\mu\text{m}$  in length. Figure 6.6(c) shows that at  $l = 0.4$  mm the deviation produces the largest longitudinal field 125  $\mu\text{m}$  away from the wire. If we calculate the field closer to the wire, the  $l$  that gives the largest field becomes smaller, i.e. the peak in Figure 6.6(c) shifts to smaller length deviations. This means that as we move the atoms closer to the wire, higher frequency

Table 6.1: A survey of the fragmentation results from various atom chip groups. The Zimmermann group tested a commercially produced, ordinary copper wire and an on-chip electroplated wire. A measurement of their ordinary wire is shown in the table, but the  $C$  is derived from a fit to the data from both wires.

Group [Reference]	Wire Material	Wire Size ( $\mu\text{m}^2$ )	Current (A)	Distance from Wire Surface ( $\mu\text{m}$ )	Well Depth (nK)	$C$ ( $\text{m}^3 \text{ J A}^{-1}$ )
Our Group	Electroplated Copper	$20 \times 10$	1	120	$200 \pm 75$	$0.8 \times 10^{-42}$
Ketterle [86]	Electroplated Copper	$50 \times 10$	0.13	85	120	$2 \times 10^{-42}$
Zimmermann [79]	Ordinary Copper Wire and Electroplated Copper	$\pi 45^2$	0.9	109	250	$5 \times 10^{-42}$
Hinds [55]	Aluminum/Copper Wire	$\pi 250^2$	4	27	1000	$2 \times 10^{-42}$

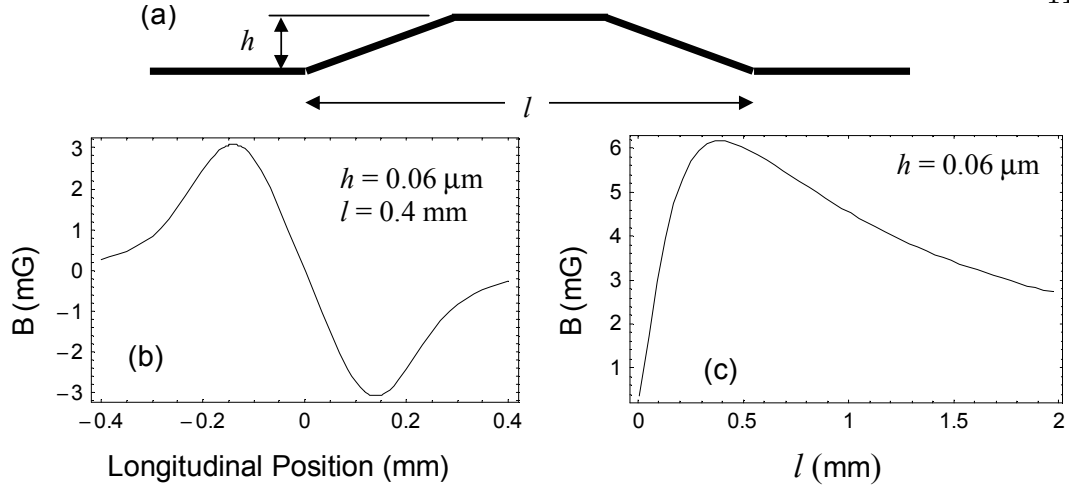


Figure 6.6: (a) A schematic of a current deviation within a wire. The lines show the path of the center of current. (b) The longitudinal component of the field produced by the wire carrying 1 A as a function of the position along the wire. The field is calculated  $125 \mu\text{m}$  above the wire, the height at which we observe the BEC to fragment. (c) The plot shows the peak-to-peak value of the longitudinal field created by the deviation with 1 A in the wire as a function of the length of the deviation,  $l$ . The field is calculated  $125 \mu\text{m}$  above the wire.

corrugations become apparent as observed in the experiment.

### 6.2.2 Current Noise

The previous section discussed the problem of spatial deviations of the current within the wire, but the atoms are also sensitive to temporal fluctuations of the current. Confined atoms are affected by noise at the trap frequency and higher harmonics and at the Zeeman splitting frequency. Noise at the Zeeman splitting frequency (around 0.5–2 MHz, depending on the trap bottom) causes spin-flip transitions to untrapped states, resulting in loss from the trap. Atoms confined near an atom chip are particularly sensitive to noise at these frequencies because they are very close to wire. The field from a wire decays as  $1/d$ , so the power in the field and thus the loss rate of atoms from the trap decays as  $1/d^2$ . In conventional magnetic traps the confining coils and wires are centimeters away from the atoms, and the atoms are not affected by small

amounts of RF noise. In atom chip experiments the atoms are only microns away from the wires, and large loss rates are observed if care is not taken to minimize the RF noise. The Ketterle group has been able to show the  $1/d^2$  dependence of the loss in their magnetic microtrap [86]. After working to eliminate this technical RF noise, they observe distance-independent 20-s lifetimes, limited by the background pressure. In our chip traps we observe lifetimes from 1–3 seconds when the atoms are 100  $\mu\text{m}$  away from the wire, which is an order of magnitude less than we expected from a lifetime limited by the background pressure. We have done some work to reduce the RF noise in the wires, such as reducing the overall length of the cables that drive the currents on the chip, eliminating ground loops, and passively filtering the RF frequencies at the vacuum feedthroughs for the wires, but we have only seen minimal improvement in the lifetime. We have not worked extensively to eliminate all RF noise because the lifetime is long enough for our experiments, and we are in a regime where we have significant loss due to three-body recombination since our atom density is  $10^{14}$ – $10^{15}$   $\text{cm}^{-3}$ . The work to reduce RF noise also reduced noise at the trapping frequencies which range from 50–3000 Hz. This noise heats the atoms and decreases the loading efficiency of the on-chip traps. We have seen improvements of a factor of 2 in loading from our efforts, but again we have not studied this problem thoroughly. As the experiments on the chip become more demanding and require a longer lifetime and a lower heating rate, we will have to study the effects of technical noise and work to reduce it.

Even if all of the technical RF noise is eliminated, the wires will still produce a small amount of noise due to thermal Johnson noise which can unfortunately drive Zeeman transitions. Henkel *et.al.* derive the loss rate for atoms near a conducting metallic slab [87]. They predict that with the trap-bottom frequency at 1 MHz the lifetime is  $\sim 20$  s at a distance of 100  $\mu\text{m}$  from a surface and  $\sim 0.9$  s at 10  $\mu\text{m}$ . The Hinds group has observed the effect thermal RF currents as the atoms are moved close to their 500  $\mu\text{m}$  in diameter wire, with approximate agreement to the predicted loss

rate [55]. However, the Henkel results are derived for a copper slab that is much thicker than the skin depth ( $\sim 70 \mu\text{m}$  for copper at 1 MHz) and much wider than the distance of the atoms from the slab. Our small  $10 \times 20 \mu\text{m}$  wires do not meet either of these conditions, and at a distance of  $10 \mu\text{m}$  from the surface of the wire, we will probably not be able to observe this effect.

### 6.3 The Waveguide Beamsplitter

The precisely patterned wires on an atom chip allow the magnetically guided atom beamsplitter to be realized. Our group and the Schmiedmayer group showed experimentally that the magnetic waveguide beamsplitter made from lithographically patterned wires works well as a multi-mode device [46, 47]. Both groups used a MOT as a source of atoms and demonstrated that, as the atoms move through the device, the beamsplitting ratio between the two output ports can be changed by varying the current ratio between the two wires that make up the beamsplitter. Since the demonstration of the multi-mode beamsplitter, there has been much work in the field, both theoretically [60–64] and experimentally, toward the realization of a coherent single-mode beamsplitter, but as of yet there has been no successful experimental implementation of a coherent waveguide beamsplitter.

#### 6.3.1 A Two-Wire Beamsplitter

We have been pursuing the development of a two-wire beamsplitter in which two bias-field guides are made to merge and separate. The field from a single bias-field guide is given by Equation 5.1. To model the beamsplitter, we place two wires in the  $xy$ -plane running parallel to the  $x$ -axis with a current of  $I_0$  flowing in each wire. The wires are separated by a distance  $2s$  such that they are centered about the  $x$ -axis. The total field



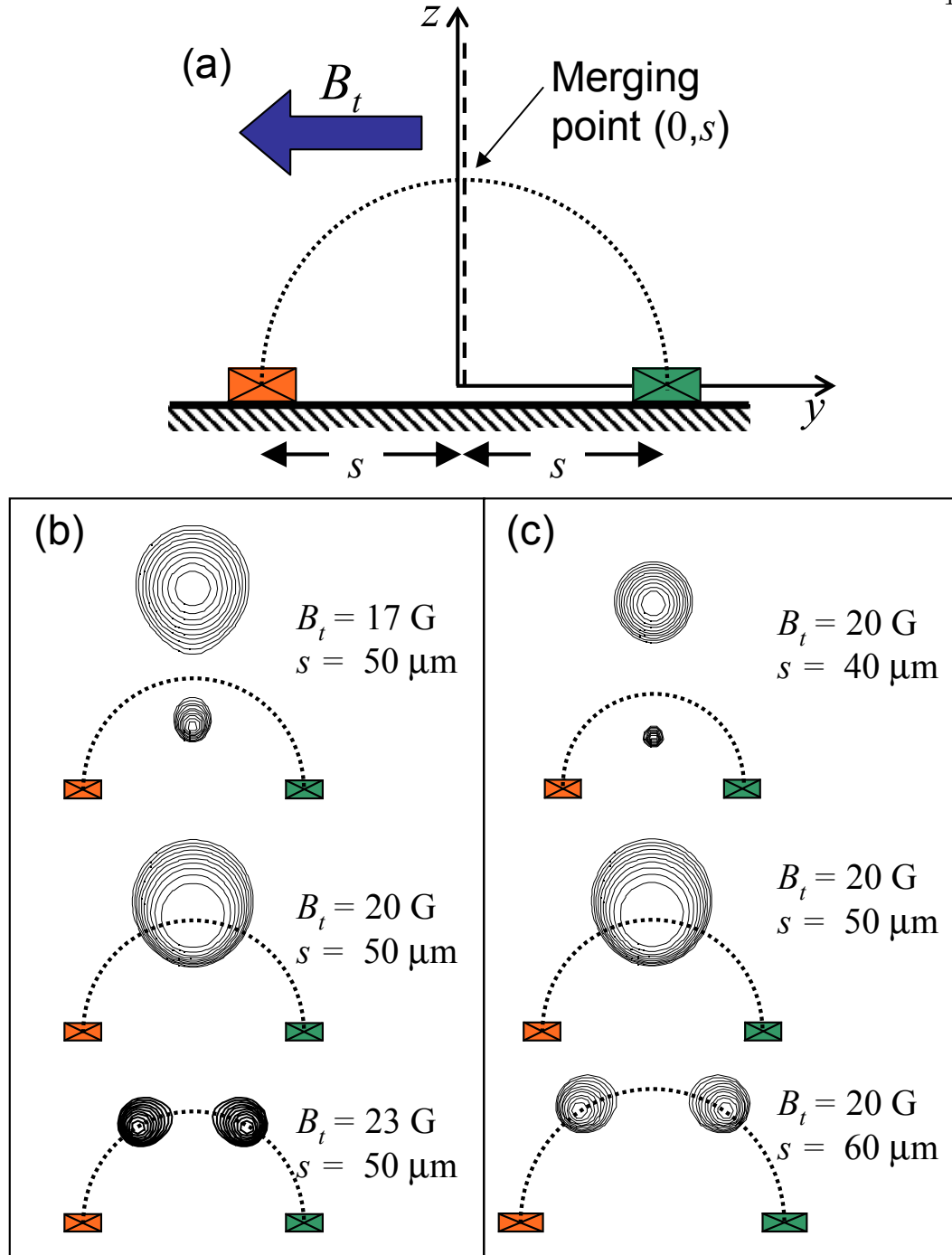


Figure 6.7: The two wire beamsplitter. (a) With a small transverse bias field or small wire spacing, the zeros are split vertically and are located on the dashed line. As the bias field or wire spacing increases, the minima move toward each other and merge when Equation 6.6 is satisfied. Then, the minima separate along the dotted circle as  $s$  or  $B_t$  is increased farther. Figures (b) and (c) show contour plots of the magnetic field for different splitting parameters. For these plots  $I_0 = 0.5$  A and  $B_{\parallel} = 3$  G, and contours are spaced by 0.1 G with the inner contour being 3.1 G. (b) The time varying beamsplitter occurs as the transverse bias field is ramped in time, and (c) the spatially varying beamsplitter occurs as the wires curve away from each other as the atoms move along them.

of the two bias-field guides is given by

$$\mathbf{B} = \begin{pmatrix} B_{\parallel} \\ B_t - \frac{\mu_o I_0}{2\pi} \left( \frac{z}{(y-s)^2+z^2} + \frac{z}{(y+s)^2+z^2} \right) \\ \frac{\mu_o I_0}{2\pi} \left( \frac{y-s}{(y-s)^2+z^2} + \frac{y+s}{(y+s)^2+z^2} \right) \end{pmatrix} \quad (6.5)$$

where  $B_{\parallel}$  is the applied longitudinal field and  $B_t$  is the transverse bias field. In general, there are two minima produced by the wires, but the minima can be made to merge if the following condition is satisfied

$$B_t = \frac{\mu_o I_0}{2\pi s} \quad (6.6)$$

The  $y$  and  $z$  position of this single minimum is  $(y_0, z_0) = (0, s)$ . By varying the bias field around the value dictated by Equation 6.6, we can split the minimum either vertically or horizontally (Figure 6.7(a)). Decreasing  $B_t$  causes the minima to split vertically along the  $z$ -axis, and the positions of the minima are given by

$$(y_0, z_0) = \frac{\mu_o I_0}{2\pi B_t} \left( 0, 1 \pm \sqrt{1 - \left( \frac{2\pi B_t}{\mu_o I_0} s \right)^2} \right) \quad \text{for} \quad B_t < \frac{\mu_o I_0}{2\pi s} \quad (6.7)$$

Increasing  $B_t$  causes the minima to move toward the wires. In fact, the minima move on a circle with a radius of  $s$  centered at the origin. Their positions in the  $yz$ -plane are

$$(y_0, z_0) = \frac{\mu_o I_0}{2\pi B_t} \left( \pm \sqrt{\left( \frac{2\pi B_t}{\mu_o I_0} s \right)^2 - 1}, 1 \right) \quad \text{for} \quad B_t > \frac{\mu_o I_0}{2\pi s} \quad (6.8)$$

We call a beamsplitter where we vary  $B_t$  in time a temporally varying beamsplitter. Atoms experiencing this type of beamsplitter are all split at one point in time.

Another type of beamsplitter based on this two wire design is a spatially varying beamsplitter (Figure 6.7(c)). In this case the spacing between the wires is slowly varied as a function of the longitudinal position, and the velocity of the atoms moving through the beamsplitter determines the rate at which  $s$  changes. If we make the assumption that the wires are locally parallel to the  $x$ -axis for all  $x$ , then Equations 6.5–6.8 are still valid except we now compare  $s$  to  $\frac{\mu_o I_0}{2\pi B_t}$ . For  $s > \frac{\mu_o I_0}{2\pi B_t}$ , the minima are split horizontally,

and Equation 6.8 shows that the height of the minima above the chip is independent of the separation between the wires. When  $s$  is less than  $\frac{\mu_o I_0}{2\pi B_t}$ , the minima are split vertically, and their location is given by Equation 6.7. The first guided-beamsplitter experiments performed in our group used a spatially varying X-shaped beamsplitter in which two wires were at first well separated, came together to merge the minima, and finally separated again [47].

To design a beamsplitter for use in an experiment, we need to know how we can generate a 50/50 beamsplitter using this two wire design. We also need to know how fast we can vary the fields or the spacing of the wires such that the atoms are not radially excited as the atoms go through the beamsplitter. Consider an X-shaped beamsplitter where the minima are first separated horizontally, and then either by ramping  $B_t$  or by changing the spacing between the wires, we cause the minima to merge and then separate again. To understand the operation of the beamsplitter, we solve the one-dimensional time-independent Schrödinger equation for a single atom in the  $y$ -direction at a height  $z_0 = \frac{\mu_o I_0}{2\pi B_t}$ . We assume that the wavefunction of the atom in  $z$ -direction is in the ground state, and is neglected in this calculation. For this calculation we consider how the eigenmodes and eigenenergies in the  $y$ -direction vary as we change the separation of the wires. To perform this numerical calculation, let us use some reasonable experimental numbers:  $B_{\parallel} = 3$  G,  $B_t = 20$  G, and  $I_0 = 0.5$  A, which gives  $z_0 = 50$   $\mu\text{m}$  for  $s \geq 50$   $\mu\text{m}$ . Figure 6.8 shows the eigenstates and their energies for a single atom in the two-wire potential, labeled by the quantum number,  $n$ , which counts the number of nodes in the wavefunction along the  $y$ -direction.

Once we know the eigenenergies, we can know how fast we need to ramp the minima together to make a beamsplitter. We input an atom into one of the ports of the beamsplitter in the ground state of that port. However, if the atom is localized in one well (or port) of the beamsplitter's double well potential, it is actually in a superposition of ground state,  $|n = 0\rangle$ , and the first excited state,  $|n = 1\rangle$ , of the double well potential

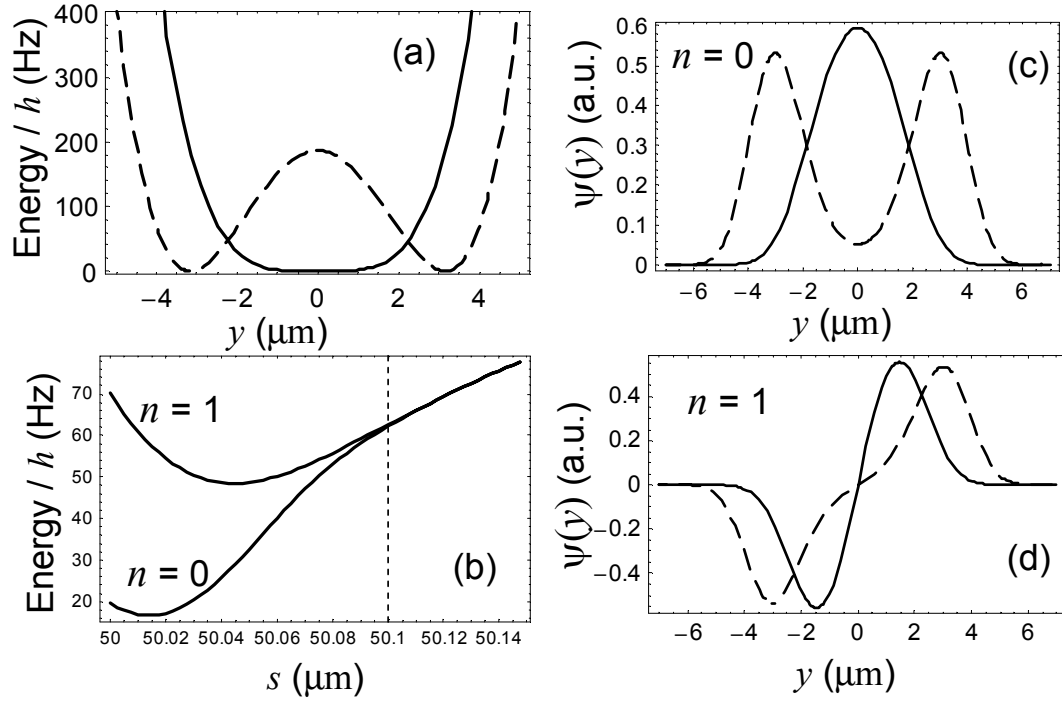


Figure 6.8: The figures show the results of integrating the Schrödinger equation for the potentials shown in (a). The conditions chosen for this integration are  $B_{\parallel} = 3$  G,  $B_t = 20$  G, and  $I_0 = 0.5$  A, which gives  $z_0 = 50$   $\mu\text{m}$ . In figures (a), (c), and (d) the solid line is for  $s = z_0 = 50$   $\mu\text{m}$  and the dashed line is for  $s = 50.1$   $\mu\text{m}$ . (b) This plot shows the eigenfrequencies,  $\omega/(2\pi)$ , for the ground state and the first excited state as a function of half the wire separation,  $s$ . (c) The ground state wavefunction is plotted for two different wire separations. (d) The first excited state wavefunction.

because when the two wells are widely separated ( $s \gg 50 \mu\text{m}$ ), the energies of the lowest two states are degenerate (Figure 6.8(b)). As the wells merge together, the degeneracy is lifted, and the atom's wavefunction starts to oscillate between the two wells. The time evolution of the wavefunction is given by

$$|\psi(t)\rangle = \frac{1}{\sqrt{2}} \left( |0\rangle + e^{i(\omega_1 - \omega_0)t} |1\rangle \right) \quad (6.9)$$

where  $\omega_0$  ( $\omega_1$ ) is the eigenfrequency of the ground (first excited) state. If the phase of the exponential in Equation 6.9 is an even (odd) integer multiple of  $\pi$ , the atoms are localized in the well on the positive (negative) side of the  $y$ -axis. This can be seen by adding or subtracting the wavefunctions of the ground and first excited states in Figure 6.8(c) and (d). When the phase of the exponential is an integer multiple of  $\pi/2$ , the wavefunction is evenly distributed between the two wells. Thus, to split an atom's wavefunction (make a 50/50 beamsplitter), we spatially reduce the wire spacing,  $s$ , from  $s > z_0$  toward  $s = z_0$  and back to the original distance such that the total accumulated relative phase is  $\pi/2$ . The total accumulated relative phase between the ground and first excited states is given by

$$\phi = \int_{t_{BS}} \omega_1(s(t)) - \omega_0(s(t)) dt \quad (6.10)$$

where  $t_{BS}$  is the time during which  $\omega_1 - \omega_0$  is significantly greater than zero, i.e. the time an atom spends in the beamsplitter. The exact functional form of the spacing between the wires as function of time,  $s(t)$ , is determined by the spacing of the wires as a function of longitudinal position and the speed at which the atoms travel through the beamsplitter. The form of  $\omega_0(s)$  and  $\omega_1(s)$  is shown in Figure 6.8(b). For 50/50 beamsplitting, we need to adjust  $t_{BS}$  such that  $\phi = \pi/2$ , and  $t_{BS} \rightarrow t_{\pi/2}$ . The closer we ramp the wires together during the beamsplitting, the shorter  $t_{\pi/2}$  needs to be and the faster the atoms have to go through the beamsplitter.

For the conditions in Figure 6.8(b),  $s$  only has to be greater than  $50.1 \mu\text{m}$  for the wells to be widely split and for little relative phase evolution to take place. For  $s < 50.1$

$\mu\text{m}$ , the wavefunction starts to oscillate from one well to the other. This typical case shows that we need to control all of the parameters of the beamsplitter to the  $10^{-4}$  level or better to be able to control the splitting ratio of the atoms. We believe that we can control the current in the wires and the bias fields to this level, but as discussed in Section 6.2.1, the wire spacing is not easily controllable because the current inside the wires deviates from the center of the wire. The necessary level of control for the currents and the fields is reduced if we can increase the ground state frequency. This is easily achieved by moving the atoms closer to the wires, but the fragmentation of the guided atoms also increases closer to the wires.

Another difficulty in using this beamsplitter is the reduction of the transverse frequency when the minima merge to form a single minimum. When the minima are separated, each minimum is formed by a quadrupole field, and with the addition of  $B_{\parallel}$ , the minimum is quadratic. When the quadrupole fields merge in the beamsplitter, they form a hexapole field, which is already quadratic, and the addition of the  $B_{\parallel}$  causes the potential to be quartic. A quartic potential has a very low ground-state frequency, and for the conditions in Figure 6.8 when the minima are merged,  $\omega_0 = 2\pi \times 20$  Hz, whereas for  $s \gg 50 \mu\text{m}$ ,  $\omega_0$  asymptotically approaches  $2\pi \times 1040$  Hz. This low ground state frequency means that we need to send the atoms through the beamsplitter slowly such that the spacing between the minima and the transverse frequency are changed adiabatically. The atoms must stay in a coherent superposition between the ground and first excited state. However, the time to accumulate a  $\pi/2$  phase shift can be relatively short. If the minima are made to completely merge, then the estimated  $t_{\pi/2}$  to change  $s$  from  $> 50.1 \mu\text{m}$  to  $s = 50 \mu\text{m}$  and back is

$$t_{\pi/2} \approx \frac{\pi}{2(\omega_1(50 \mu\text{m}) - \omega_0(50 \mu\text{m}))} = \frac{\pi}{4\pi(72 \text{ Hz} - 20 \text{ Hz})} = 4.8 \text{ ms} \quad (6.11)$$

where the ground and first excited state frequencies are taken from Figure 6.8(b). However, to be adiabatic, we need to change the potential on a time scale longer than the

period of the ground state, which is 50 ms. Thus, the need to be adiabatic and the need to accumulate a relative phase of only  $\pi/2$  seem to exclude each other. To make these two time scales comparable, we can allow the atoms to accumulate a relative phase equal to an integer multiple of  $\pi/2$ , say  $10\pi/2$ . However, this is undesirable because for example, a 5% error in the time,  $t_{10\pi/2}$ , will result in all of the atoms being in one of the output ports, but a 5% error in  $t_{\pi/2}$  will only effect the splitting ratio by  $\sim 5\%$ . Another method for making  $t_{\pi/2}$  comparable to the time necessary for adiabaticity is to maintain a small barrier between the minima by reducing  $s$  to only  $50.08 \mu\text{m}$  such that the largest splitting between the first two states is only 5 Hz, giving  $t_{\pi/2} = 50$  ms. For these conditions the atoms are tunneling through the barrier between the minima. This requirement for adiabaticity becomes easier to attain if, again, the trap frequencies are higher. Overall, higher frequencies will make the beamsplitter easier to operate.

Analysis of a two-wire beamsplitter is given in more detail in References [61, 64]. Of particular interest is the paper by Stickney and Zozulya. They explore more thoroughly the problem of adiabaticity and include atom-atom interactions in the treatment of the two-wire beamsplitter. They discuss two regimes for beamsplitting. One is where the minima are made to merge completely, and the other is where the horizontal minima do not merge and a small barrier between the minima allows a weak coupling between them, i.e. the atoms tunnel through the barrier. When the two minima merge completely, they find that indeed adiabaticity is difficult to achieve, and the atoms have to be in the beamsplitter for numerous transverse oscillation periods in order to be adiabatic, during which they accumulate a large relative phase. In this case a small amount of nonlinearity caused by the atom-atom interactions does not affect the beamsplitter. In the tunneling beamsplitter, as mentioned above, adiabatic propagation through the beamsplitter is much easier to attain, but the nonlinear atom-atom interaction modifies the tunneling rate through the barrier. They give a nonlinearity parameter for the

center of a BEC propagating in a guide as

$$P \approx 4\pi a_s N / L_{BEC} \quad (6.12)$$

where  $a_s$  is the s-wave scattering length,  $N$  is the total number of atoms, and  $L_{BEC}$  is the length of the BEC. Increasing  $P$  first increases the period of oscillation between the two minima and then decreases it. For a BEC traveling in a guide, the nonlinearity is weak in the head and tail of the cloud but strong near the center. Thus, for  $P > 1$ , the number of atoms transferred from one minima to the other will vary along the length of the cloud. For  $P \gg 1$ , not only is the tunneling rate suppressed but the nonlinearity can prevent the exchange of atoms between the minima. We typically operate the beamsplitter with  $P = 0.5$ – $2$ , where  $N = 10^4$  and  $L_{BEC} \approx 1$  mm so we should be able to observe the nonlinear effects in future experiments.

### 6.3.2 Thermal Atom Beamsplitter

The atom waveguide beamsplitter on our first chip consists of a straight section of the primary wire on which the atoms are coupled into the beamsplitter (Figure 6.9(a)). The primary wire is joined by the secondary wire where they are parallel for 10 mm, and then split symmetrically. The separation between the two wires is 100  $\mu\text{m}$  in the beamsplitter; after the beamsplitter the separation is 1 mm. For this wire spacing the atoms need to be guided at a distance 50  $\mu\text{m}$  away from the chip for the magnetic minima to merge. This wire configuration allows us to achieve both a temporally varying beamsplitter and a spatially varying beamsplitter. If we set the currents and the bias fields correctly and allow the atoms to move through the beamsplitter, we can realize the spatially varying beamsplitter. To achieve a temporally varying beamsplitter, we can at first have the secondary wire off ( $I_2 = 0$  A). Then, when the atoms are in the beamsplitter traveling on the primary wire, we can ramp  $B_t$  and  $I_2$  in time to cause the beamsplitting to occur.



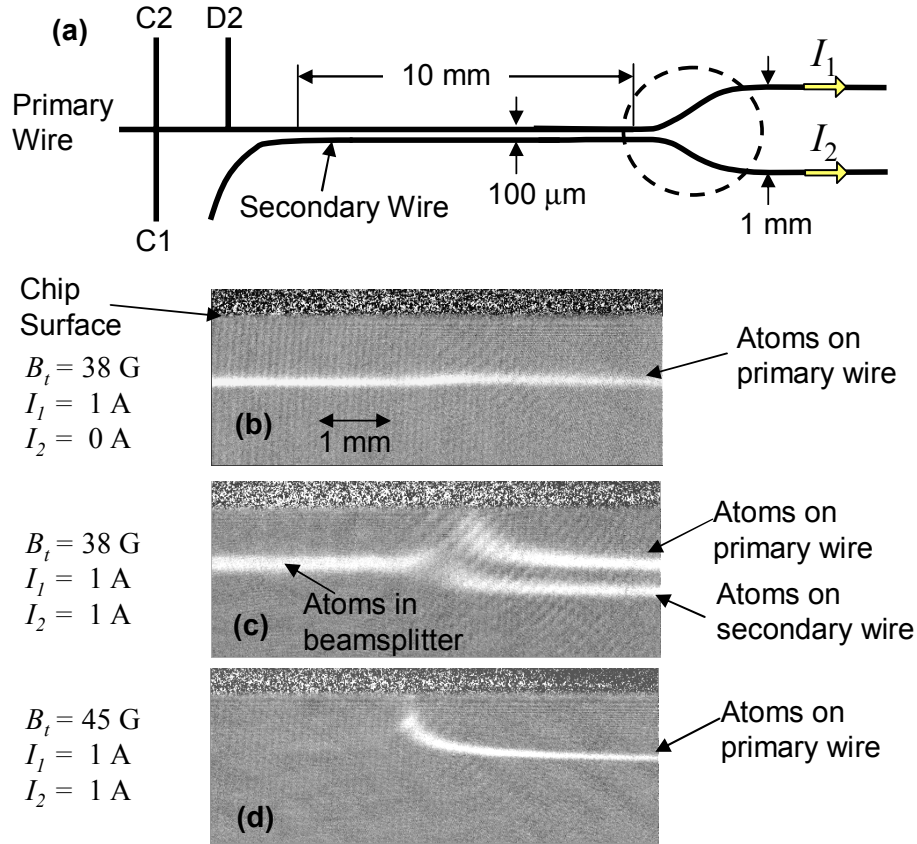


Figure 6.9: (a) A schematic of the wires in the beamsplitter region of the chip. The dashed circle indicates the location of the images in (b)–(d). For the images (b)–(d)  $B_{\parallel} = 2$  G. To image the atoms, we shut off the transverse bias field, allow the wires to push the atoms away for 2 ms, and then take the image. (b) An image of thermal atoms moving along the primary wire with the secondary wire off. (c) Here  $I_2 = 1$  A, and the atoms are split between the two output ports. The beam splitting ratio is 55% on the primary wire and 45% on the secondary wire. Before imaging,  $I_2$  is jumped to 2 A when  $B_t$  is shut off so the atoms on the secondary wire are pushed farther away during the expansion. The atoms do not continuously split in the image because where the wires start to separate, they are slightly attractive during the expansion process. (d) The conditions for this image are the same as image (c) except  $B_t = 45$  G. With this strong bias field the minima in the beamsplitter never merge so the atoms remain on the primary wire. The atoms in the beamsplitter are not visible in the image because they are attracted to the surface of the chip during the expansion.

As an initial beamsplitting experiment, we send  $10\text{-}\mu\text{K}$  atoms traveling at  $28\text{ cm/s}$  through the beamsplitter. These atoms are released from the evaporation chamber and allowed to move through the beamsplitter using the methods described in Section 4.3. For this experiment we realize a spatially varying beamsplitter by setting the current in the primary wire and the secondary wire to  $1\text{ A}$  and the longitudinal bias field to  $2\text{ G}$ . For these currents the required transverse bias field for the magnetic minima to merge is  $B_t = 40\text{ G}$ . For bias fields less than this value the minima are split vertically in the beamsplitting region, and atoms moving into the beamsplitter split roughly equally between the two output ports (Figure 6.9(c)). For bias fields larger than  $40\text{ G}$ , the minima of the two wires never merge, and they remain horizontally split in the beamsplitter so the atoms cannot be coupled onto the secondary wire (Figure 6.9(d)). With this simple experiment we can verify that our beamsplitter functions properly at least for thermal atoms. We now turn to the testing of the beamsplitter with a BEC.

### 6.3.3 The Beamsplitter with a BEC

Section 6.1 shows that we can achieve single mode propagation of the BEC in the waveguide as it moves toward the beamsplitter. By using this source, rather than thermal atoms, we can probe the coherence properties of the beamsplitter. However, there are two problems in trying to move the atoms the  $2\text{-mm}$  distance from the T trap at D2 into the beamsplitter where the primary wire and the secondary wire are parallel. The first problem is relatively minor: as the secondary wire curves in to approach the primary wire, it produces a significant longitudinal field. Because the current in the secondary wire has to run in the same direction as the current in the primary wire, this longitudinal field adds to the externally applied longitudinal field,  $B_{\parallel}$ , creating a barrier to the atoms as they move toward the beamsplitter on the primary wire. With  $I_2 = 1\text{ A}$ , the wire produces a  $\sim 2\text{ G}$  barrier for the atoms, which means that the atoms

need to be traveling at  $> 11$  cm/s to enter the beamsplitter, a speed that is not easily achieved. This problem can easily be avoided by allowing the atoms to move into the beamsplitter before ramping on the secondary wire. This means we can only make a temporally varying beamsplitter with this wire configuration.

The second problem is more serious. To make an X-shaped beamsplitter where the minima merge and separate horizontally, the atoms need to propagate  $< 50$   $\mu\text{m}$  below the wires as required by the  $100$   $\mu\text{m}$  spacing between the primary and secondary wires. However, various surface effects do not allow the atoms to propagate at this distance. To test the propagation at  $50$   $\mu\text{m}$ , we release the atoms into the guide at  $100$   $\mu\text{m}$  and then decrease the current in the primary wire until the atoms are  $50$   $\mu\text{m}$  below the primary wire. We observe that as the atoms propagate at  $50$   $\mu\text{m}$ , they begin to heat dramatically and within  $20$  ms their temperature has increased by a factor of four. Atoms that propagate  $100$   $\mu\text{m}$  below the chip do not heat and remain in the lowest mode of the guide as seen in Figure 6.1.

We are not sure why the atoms heat as they move closer to the wires. A possibility is that the small current deviations within the wire cause this problem as the atoms move over the corrugated potential. However, the atoms are moving at  $2.4$  cm/s and the corrugations have a period of  $\sim 170$   $\mu\text{m}$  which means the atoms see the potential changing at  $100$ – $300$  Hz. The transverse guide frequency,  $\nu_r$ , is  $2.4$  kHz so the atoms should move adiabatically through the corrugated potential. Perhaps a more likely source is that the amplitude of the current noise from the wire increases linearly as the atoms are moved closer to the wire. If the frequency of the noise is near the trap frequency or a higher harmonic, the atoms can rapidly heat. We can reduce some of this noise as described in Section 6.2, but we are not sure if this improved the performance of the guide at  $50$   $\mu\text{m}$ . To avoid the problem, we have changed the way we operate the beamsplitter.

To form the beamsplitter in this new method, we allow the atoms to propagate

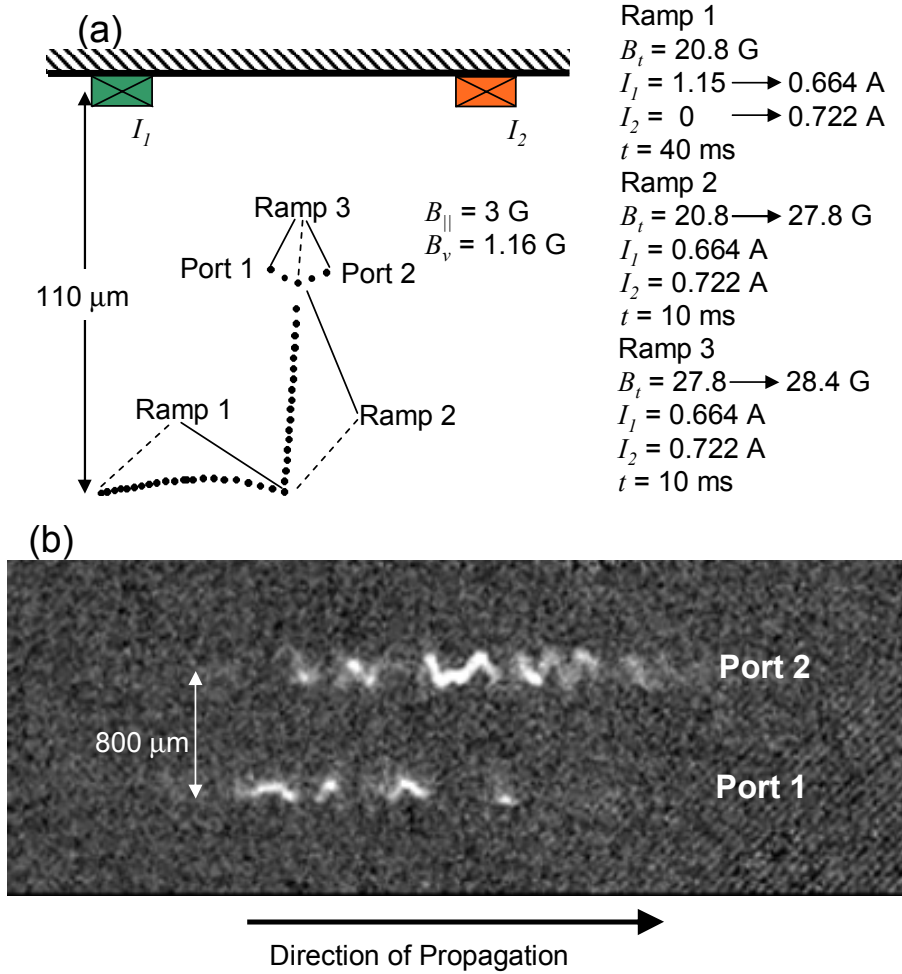


Figure 6.10: (a) This figure shows how we ramp the atoms through the beamsplitter. The dots indicate the transverse position of the atoms as we ramp the currents. The dashed lines point to the position of the atoms at the beginning of the ramps, and the solid lines point to the position at the end. (b) This image shows the longitudinal and vertical distribution of the atoms after 8 ms of expansion. To release the atoms, we first shut off  $B_t$  and  $I_2$ , and then  $540\ \mu\text{s}$  later we shut off  $I_1$ . This sequence pushes the atoms that start closer to the primary wire farther away from the chip during the expansion, which is why the ports are separated vertically in the image. The atoms in Port 1 are lower in the image.

into the beamsplitter at  $100\ \mu\text{m}$  below the primary wire. We also accelerate the atoms to  $6.3\ \text{cm/s}$  as they leave the T trap. When the atoms are in the beamsplitter, the length of the cloud is only to  $1\ \text{mm}$  FWHM to maintain sufficient signal for imaging. Once the atoms are in the beamsplitter region, we ramp on  $I_2$  and slightly lower  $I_1$  over  $40\ \text{ms}$ . This translates the atoms under the center of the beamsplitter (Figure 6.10(a)), and the atoms are in the minimum farthest from the chip surface as seen in upper plot of Figure 6.7(b). Then, we increase  $B_t$  over  $10\ \text{ms}$  to cause the vertically aligned minima to merge, and finally a ramp of  $10\ \text{ms}$  is applied to  $B_t$  to separate the minima in the horizontal direction. Again, we find that the atoms rapidly heat as they move close to the chip's surface, but the atoms are at a distance of  $50\ \mu\text{m}$  for only a short time ( $\sim 10\ \text{ms}$ ), and we can complete the beamsplitter experiments. However, these ramps of  $B_t$  are not adiabatic, and we excite some transverse slosh during the ramps.

Figure 6.10(b) shows an image after the BEC has gone through the beamsplitter. We find that the beamsplitting occurs with currents of  $I_1 = 0.644\ \text{mA}$  and  $I_2 = 0.722\ \text{mA}$  and a bias field of  $B_t = 27.7\ \text{G}$ . Ideally, the currents in the wires should be equal for the minima to merge, but the different currents can be explained by a stray vertical bias field,  $B_v$ . A calculation shows that if  $B_v = 0$ , the difference in currents would cause the minima to be separated by  $28\ \mu\text{m}$  during the bias field ramp, but if we include  $B_v$ , the minima do merge although the merging point is offset  $2\ \mu\text{m}$  toward the primary wire. We infer that  $B_v$  is  $1.16\ \text{G}$  pointing toward the chip surface.

The image in Figure 6.10(b) shows that the BEC is either in one output port or the other. There does not seem to be any point along the cloud where 50/50 beamsplitting occurs. If there is, it is only one imaging pixel wide. We attribute this high-contrast splitting to the small current deviations inside the two wires. Evidence for this is shown in Figure 6.11. The current deviations are stationary within the wires. Thus, no matter the position of the center of mass of the cloud, at a particular point on the chip the beamsplitter will always put the atoms into a particular port. More specifically,

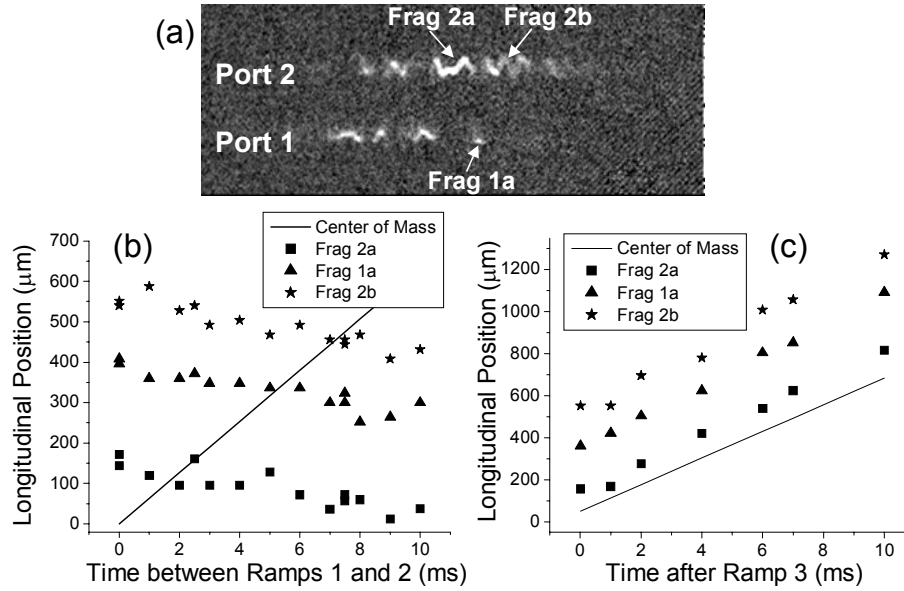


Figure 6.11: (a) This is the same image as in Figure 6.10(b). Here we label three fragments of the cloud. (b) The fragments are seen to move slightly backwards as a function of the time between Ramps 1 and 2 (Figure 6.10(a)). The solid line is an estimate of the longitudinal position of the center of mass of the cloud. (c) The fragments move at the center-of-mass speed after the atoms have undergone the beamsplitting process in Ramp 3.

fragment 2a (as shown in Figure 6.11(a)) will always be imaged in the same position regardless of the position of the center of the cloud when the atoms are ramped through the beamsplitter. The data in Figure 6.11(b) are obtained by varying the time between Ramps 1 and 2 while recording the position of the various fragments. Indeed, the fragments appear to be stationary while the center of mass of the cloud is moving forward. In fact, the fragments are moving slowly backwards. This is due to the longitudinal spreading of the cloud, and the slope of this backward movements agrees with the spreading velocity. Figure 6.11(c) shows the position of the fragments as a function of the time after Ramp 3. In this case the atoms have already been ramped through the beamsplitter, and the fragments travel at the center-of-mass velocity.

To better understand how the beamsplitter fragments the atoms into the ports without any 50/50 beamsplitting, we have developed a simple model of a small current

deviation inside the conductors similar to the model used to calculate the width of the current deviation in Section 6.2.1. In this case the straight primary wire lies next to the secondary wire containing a single deviation (Figure 6.12(a)). From this model we would like to discover why we do not observe 50/50 beamsplitting. From the measured amplitude of the slosh in each port we can derive the energy of the atoms as the minima merge. This energy is estimated to be  $\mu \times 0.2$  mG where  $\mu$  is the magnetic moment of the atoms. For beamsplitting to occur the minima need to merge vertically and then split symmetrically in the horizontal direction (Figure 6.12(b) and (c)). However, current deviations can tip the beamsplitting potential so that when the single minimum separates, all of the atoms end up in one of potential minima. When the barrier between the two minima emerges as we ramp  $B_t$ , there is a difference between the bottom of the two minima (Figure 6.12(d) and (e)). If the difference is greater than 0.2 mG, there will be no atoms in the higher port. The deviation tilts the beamsplitter's potential because the longitudinal field produced by the deviation decays away with the distance from the wire (Figure 6.12(a)). Thus, there is a horizontal gradient (in the  $y$ -direction) in the longitudinal field. For the conditions in Figure 6.12(d) and (e) the gradient is 1.17 G/cm. If the deviation is 100  $\mu\text{m}$  long, it must have a width  $> 0.01$   $\mu\text{m}$  to affect the splitting. On the positive- $x$  side of the deviation the atoms will move toward the secondary wire, and on the negative- $x$  side of the deviation, the gradient pushes the atoms toward the primary wire.

When the currents in the two wires are not adjusted for beamsplitting, the two minima will not merge but will pass by each other as we ramp the bias field. If a 0.2 mG barrier is maintained between the two minima, the atoms will remain in the minimum in which they started, the minimum farthest from the chip. This farthest minimum will move toward the wire that has a current larger than the current required for beamsplitting. We observe experimentally that if we increase (decrease) the current in the secondary wire by 2.3 mA, we can force all of the atoms into Port 2 (1). The

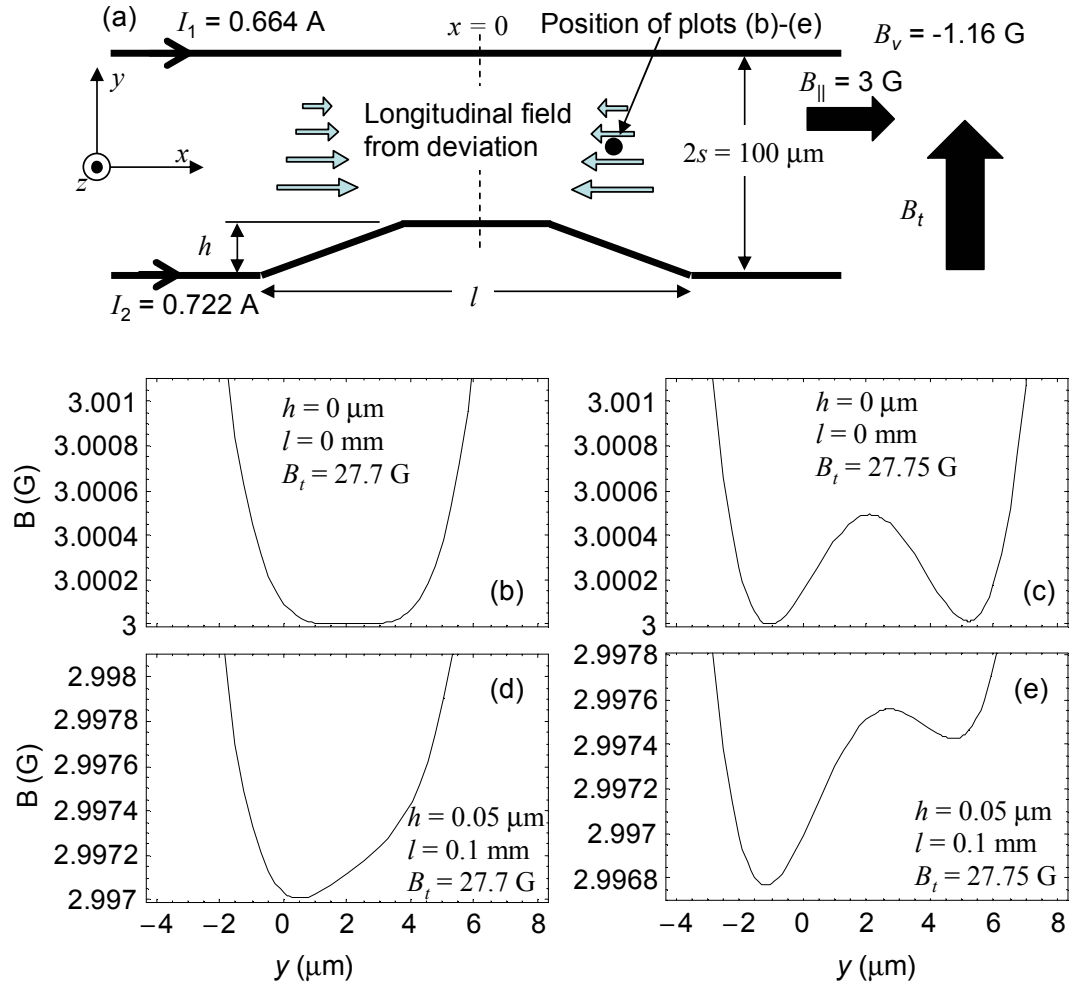


Figure 6.12: (a) The schematic shows the two wires of the beamsplitter where the secondary wire has a deviation in its center of current. The deviation causes a longitudinal field that decays away with the distance from the secondary wire. Figures (b) and (c) show the horizontal potential of the beamsplitter when the width of the deviation is zero. The plots are in the  $y$ -direction at  $z = 50$   $\mu\text{m}$ . Figures (d) and (e) show how the horizontal gradient of the longitudinal field from the current deviation tilts the beamsplitting potential to put the atoms in a particular port.



change in currents overcomes the gradients caused by the current deviations. From this change in current we can extract the maximum width of the current deviation,  $h$ , by seeing how small  $h$  has to be such that  $\pm 2.3$  mA in  $I_2$  creates a 0.2 mG barrier between the minima. We find that the deviation has to be less than  $0.07 \mu\text{m}$ , similar to the width we found in the fragmentation experiments in Section 6.2.1.

The above model assumed that the current deviation is in the horizontal plane of the chip. However, the current could also deviate in the vertical plane. In this case the angled segments of current in the deviation still produce a decaying longitudinal field that tips the splitting potential, but there is an additional effect. For the horizontal deviation, equal splitting occurs in the center of the deviation because the longitudinal fields from the deviation cancel. For a vertical deviation equal splitting does not occur because the center of current is lifted out of the plane of the wires. In the new plane defined by the center of current, the transverse bias field has both vertical and horizontal components. In essence, the transverse bias field adds to the vertical bias field, causing the minima to avoid each other. Even though the effect of a vertical deviation is subtly different, all of the above arguments are true, and the deviation of the current is still on the order of  $0.05 \mu\text{m}$ .

With this model we can also address the question of how small the deviations have to be in order to achieve a coherent beamsplitter with 50/50 splitting. For our current beamsplitter the ground state frequency is approximately 20 Hz which corresponds to a magnetic field of 0.03 mG. Thus, the width of the deviations have to be reduced to less than 4 nm for  $l = 100 \mu\text{m}$ , a factor of ten to twenty reduction in deviation width. If we can achieve a higher ground state frequency, we can tolerate larger deviations.

## 6.4 Outlook for the Waveguide Beamsplitter

For work to progress in the area of the guided atom interferometry, we need to overcome the difficulties caused by the fragmentation of the cloud. There may be

ways to reduce the fragmentation effect by using different fabrication techniques for the microstructure wires [79]. We have focused on developing ways of working with the corrugated potential that causes the fragmentation. Here, I present several ideas for improving the beamsplitter.

One way to avoid the fragmentation is to work farther away from the wires. Even though the fragmentation reduces as  $1/d^2$ , so does the transverse frequency of the guide for a given wire current. To form the beamsplitter, we would like the atoms to be as close to wires as possible because higher frequencies reduce the sensitivity of the beamsplitter to noisy fields and currents and relaxes the stringent requirements imposed by adiabaticity. Thus, moving farther away is not an ideal solution. Perhaps more promising is to configure the wires to form a spatially varying beamsplitter. In this type of beamsplitter the splitting occurs in a limited section of the guide, and all of the atoms experience the same potential. Hopefully, we could tune the currents so that we could control the splitting. However, to make sure that the cloud moves adiabatically through the beamsplitter, we would have to make it quite long, and the cloud would be split and recombined several times as the corrugated potential modulates the splitting potential. Additionally, the cloud has a longitudinal velocity spread, and the splitting ratio in a spatially varying beamsplitter is velocity dependent so the splitting ratio varies along the length of the cloud.

To reduce the fragmentation effect we could vary in time both the wire currents and the transverse bias field in order to average out the corrugations [79], similar in method to the time-averaged, orbiting potential (TOP) trap [76]. The wire currents and the transverse bias field oscillate at a frequency approximately ten times the radial guide frequency while the longitudinal bias field is held constant. The atoms would see the time-averaged potential, and because the longitudinal field created by the wires continually changes direction, it averages to zero. Our simulations show that the fragmentation in a beamsplitter caused by a horizontal deviation would be reduced by at

least a factor of 100. However, the fragmentation caused by a vertical deviation would only be reduced by a little more than a factor of 10 because the center of current is lifted out of the plane of the wires, and this effect does not average out. This technique may be worth pursuing since vertical deviations in the current may be reduced by using vertically thin, horizontally wide wires. Both the spatially varying and the temporally varying beamsplitters would benefit from the time-averaging technique.

Another idea to reduce the fragmentation effect is to replace the larger  $20 \times 10 \mu\text{m}$  wire with several small parallel wires, for example  $2 \times 1 \mu\text{m}$  wires space by  $1 \mu\text{m}$ . Each small wire would hopefully produce a randomly corrugated potential, and the field far away from several closely spaced wires would average to form a smooth longitudinal potential. The idea depends on the corrugated potential from each wire being random. The fabrication process may affect the corrugation, and side-by-side wires could exhibit a correlated corrugated potential. However, the origin of the corrugated potentials is not known, and the geometry of several closely spaced wires may significantly reduce the fragmentation effect. One concern is that the total current will have to be reduced when implementing this multi-wire design because the total cross section of the conductor is reduced. However, the total amount of current carried by the multiple wires will not be reduced by the same amount because the smaller conductors can transfer heat to the substrate more efficiently and can tolerate a higher current density.

A final beamsplitter idea is shown in Figure 6.13. Confining wires provide the radial trapping potential, and a small splitting wire and a transverse bias field split the trapping potential. Splitting can be done by changing the transverse bias field, the splitting wire current, or the spacing of the confining wires. The nice feature of this beamsplitter is that the ground state frequency can be made a factor of ten or more higher than the typical two-wire beamsplitter because of the close proximity of the splitting wire ( $\sim 5 \mu\text{m}$ ) to the point where the minima merge. This reduces the stability requirements on the currents and the fields, and an adiabatic beamsplitter is much easier

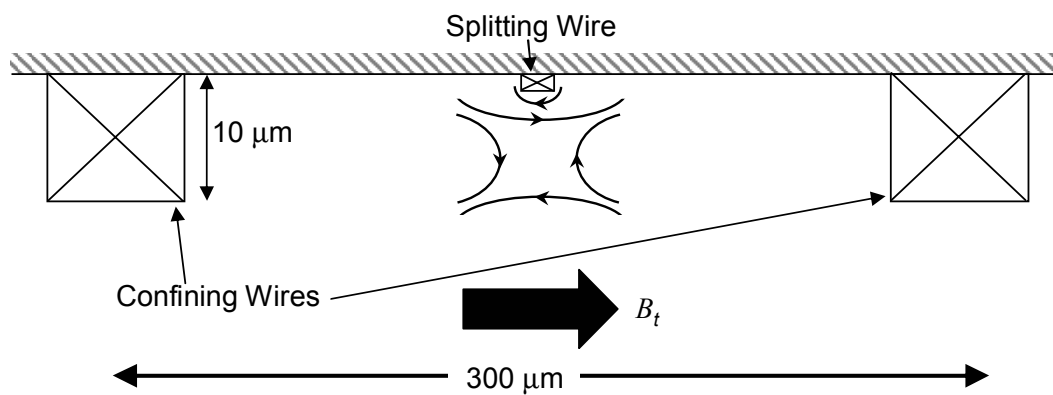


Figure 6.13: A new beamsplitter idea. The large outer wires provide the confinement while the small inner wire in combination with the transverse bias field provides the splitting potential. Typical currents are 1 amp in the confining wires and 10 mA in the splitting wire. The transverse bias field is then 4 G.

to achieve. However, according to Equation 6.4, the fragmentation could be 1000 times worse, although it remains to be seen why the current causes the fragmentation effect, and perhaps different wire materials and fabrication processes can reduce it or eliminate it all together.

Overall, there are a number of ideas to pursue for improving the performance of the atom waveguide beamsplitter, and we have only just begun this research. The fragmentation of the cloud is a serious problem at this point, but there seem to be several ways to overcome it. Our modular three-chamber experimental apparatus will allow us to test a wide variety of atom chips, and as research continues to produce new ideas, the system can easily be reconfigured to accommodate them. The combination of the flexible experimental apparatus and the creative people that continue to work on the experiment should provide rapid progress toward guided atom interferometry.

## Bibliography

- [1] A. A. Michelson and E. W. Morley. . Am. J. Sci., 34:333, 1887.
- [2] C. Davisson and L. H. Germer. Diffraction of Electrons by a Crystal of Nickel. Phys. Rev., 30:705–40, 1927.
- [3] L. Marton. Electron Interferometer. Phys. Rev., 85:10571058, 1952.
- [4] L. Marton, J. A. Simpson, and J. A. Studdeth. . Rev. Sci. Instrum., 25:1099, 1954.
- [5] T. Springer H. Maier-Leibnitz. . Z. Phys., 167:386, 1962.
- [6] David W. Keith, Christopher R. Ekstrom, Quentin A. Turchette, and David E. Pritchard. An Interferometer for Atoms. Phys. Rev. Lett., 66:2693–2696, 1991.
- [7] O. Carnal and J. Mlynek. Young’s Double-Slit Experiment with Atoms: A Simple Atom Interferometer. Phys. Rev. Lett., 66:2689–72, 1991.
- [8] David M. Giltner, Roger W. McGowan, and Siu Au Lee. Atom Interferometer Based on Bragg Scattering from Standing Light Waves. Phys. Rev. Lett., 75:2638–41, 1995.
- [9] Mark A. Kasevich and Steven Chu. Atomic Interferometry Using Stimulated Raman Transitions. Phys. Rev. Lett., 67:181–4, 1991.
- [10] F. Riehle, Th. Kisters, A. Witte, J. Helmcke, and Ch. J. Borde. Optical Ramsey Spectroscopy in a Rotating Frame: Sagnac Effect in a Matter-Wave Interferometer. Phys. Rev. Lett., 67:177–80, 1991.
- [11] S. Chu. Atom Interferometry. In R. Kaiser, C. Westbrook, and F. David, editors, Coherent Atomic Matter Waves, NATO Advanced Studies Institute, Les Houches, Session LXXII, pages 317–370, Paris, 1999. EDP Sciences and Springer.
- [12] Paul R. Berman. Atom Interferometry. Academic Press, San Diego, CA, 1997.
- [13] Mark A. Kasevich. Private Communication.
- [14] T. L. Gustavson, A. Landragin, and M. A. Kasevich. Rotation Sensing with a Dual Atom-Interferometer Sagnac Gyroscope. Class. Quantum Gravity, 17:2385–98, 2000.

- [15] Dirk Müller. Toward Integrated Atom-Interferometry: Guides, a Beamsplitter, and a Switch. PhD thesis, JILA, University of Colorado.
- [16] W. Seifert, C. S. Adams, V. I. Balykin, C. Heine, Yu Ovchinnikov, and J. Mlynek. Reflection of Metastable Argon Atoms from an Evanescent Wave. Phys. Rev. A, 49:3814–23, 1994.
- [17] I. G. Hughes, P. A. Barton, T. M. Roach, M. G. Boshier, and E. A. Hinds. Atom Optics with Magnetic Surfaces. I. Storage of Cold Atoms in a Curved 'Floppy Disk'. J. Phys. B: At. Mol. Opt. Phys., 30:647–58, 1997.
- [18] I. G. Hughes, P. A. Barton, T. M. Roach, M. G. Boshier, and E. A. Hinds. Atom Optics with Magnetic Surfaces: II. Microscopic Analysis of the 'Floppy Disk' Mirror. J. Phys. B: At. Mol. Opt. Phys., 30:2119–32, 1997.
- [19] K. S. Johnson, M. Drndic, J. H. Thywissen, G. Zabow, R. M. Westervelt, and M. Prentiss. Atomic Deflection Using an Adaptive Microelectromagnetic Mirror. Phys. Rev. Lett., 81:1137–41, 1998.
- [20] P. Rosenbusch, B. V. Hall, I. G. Hughes, C. V. Saba, and E. A. Hinds. Manipulation of cold atoms using a corrugated magnetic reflector. Phys. Rev. A, 61:031404, 2000.
- [21] J. E. Bjorkholm, R. R. Freeman, A. Ashkin, and D. B. Pearson. Observation of Focusing of Neutral Atoms by the Dipole Forces of Resonance-Radiation Pressure. Phys. Rev. Lett., 41:1361–64, 1978.
- [22] G. Timp, R. E. Behringer, D. M. Tennant, J. E. Cunningham, M. Prentiss, and K. K. Berggren. Using Light as a Lens for Submicron, Neutral-Atom Lithography. Phys. Rev. Lett., 69:1636–9, 1992.
- [23] W. G. Kaenders, F. Lison, I. Muller, A. Richter, R. Wynands, and D. Meschede. Refractive Components for Magnetic Atom Optics. Phys. Rev. A, 54:5067–75, 1996.
- [24] E. Maréchal, S. Guibal, J.-L. Bossennec, R. Barbé, J.-C. Keller, and O. Gorceix. Longitudinal focusing of an atomic cloud using pulsed magnetic forces. Phys. Rev. A, 59:4636–40, 1999.
- [25] W. D. Phillips and H. Metcalf. Laser Deceleration of an Atomic Beam. Phys. Rev. Lett., 48(9):596–9, 1982.
- [26] W. Ertmer, R. Blatt, J. L. Hall, and M. Zhu. Laser Manipulation of Atomic Beam Velocities: Demonstration of Stopped Atoms and Velocity Reversal. Phys. Rev. Lett., 54:996–9, 1985.
- [27] M. Zhu, C. W. Oates, and J. L. Hall. Continuous High-Flux Monovelocity Atomic Beam Based on a Broadband Laser-Cooling Technique. Phys. Rev. Lett., 67:46–9, 1991.
- [28] J. Nellessen, J. Werner, and W. Ertmer. Magneto-optical compression of a monoenergetic sodium atomic beam. Opt. Comm., 78:300–308, 1990.

- [29] E. Riis, D. S. Weiss, K. A. Moler, and S. Chu. Atom Funnel for the Production of a Slow, High-Density Atomic Beam. Phys. Rev. Lett., 64:1658–61, 1990.
- [30] E. L. Raab, M. Prentiss, Alex Cable, Steven Chu, and D. E. Pritchard. Trapping of Neutral Sodium Atoms with Radiation Pressure. Phys. Rev. Lett., 59:2631–4, 1987.
- [31] M. H. Anderson, J. R. Ensher, M. R. Matthews, C. E. Wieman, and E. A. Cornell. Observation of Bose-Einstein Condensation in a Dilute Atomic Vapor. Science, 269(5221):198–201, 1995.
- [32] K. B. Davis and W. Ketterle. Bose-Einstein Condensation in a Gas of Sodium Atoms. Phys. Rev. Lett., 75:3969–73, 1995.
- [33] C. C. Bradley, C. A. Sackett, and R. G. Hulet. Bose-Einstein Condensation of Lithium: Observation of limited condensate number. Phys. Rev. Lett., 78:985–9, 1997.
- [34] M. J. Renn, D. Montgomery, O. Vdovin, D. Z. Anderson, C. E. Wieman, and E. A. Cornell. Laser-Guided Atoms in Hollow-Core Optical Fibers. Phys. Rev. Lett., 75:3253–6, 1995.
- [35] M. J. Renn, E. A. Donley, E. A. Cornell, C. E. Wieman, and D. Z. Anderson. Evanescent-Wave Guiding of Atoms in Hollow Optical Fibers. Phys. Rev. A, 53:R648–51, 1996.
- [36] H. Ito, T. Nakata, K. Sakaki, M. Ohtsu, K. I. Lee, and W. Jhe. Laser Spectroscopy of Atoms Guided by Evanescent Waves in Micron-Sized Hollow Optical Fibers. Phys. Rev. Lett., 76:4500–3, 1996.
- [37] G. Workurka, J. Keupp, and K. Sengstock. Guiding of Metastable Neon Atoms in Hollow-Core Optical Fibers. In Proceedings of International Quantum Electronic Conference, volume 7, page 256. Opt. Soc. America, 1998.
- [38] J. Schmiedmayer. Guiding and Trapping a Neutral Atom on a Wire. Phys. Rev. A, 52:R13–R16, 1995.
- [39] J. Schmiedmayer. A Wire Trap for Neutral Atoms. Appl. Phys. B, 60:169–79, 1995.
- [40] A. Goepfert, F. Lison, R. Schütze, R. Wynands, D. Haubrich, and D. Meschede. Efficient Magnetic Guiding and Deflection of Atomic Beams with Moderate Velocities. Appl. Phys. B, 69:217–22, 1999.
- [41] M. Key, I. G. Hughes, W. Rooijakkers, B. E. Sauer, E. A. Hinds, D. J. Richardson, and P. G. Kazansky. Propagation of Cold Atoms along a Miniture Magnetic Guide. Phys. Rev. Lett., 84:1371–4, 2000.
- [42] J. A. Sauer, M. D. Barrett, and M. S. Chapman. A storage ring for neutral atoms. Phys. Rev. Lett., 87:270401, 2001.
- [43] D. Müller, D. Z. Anderson, R. J. Grow, P. D. D. Schwindt, and E. A. Cornell. Guiding Neutral Atoms Around Curves with Lithographically Patterned Current-Carrying Wires. Phys. Rev. Lett., 83:5194–7, 1999.



- [44] N. H. Dekker, C. S. Lee, V. Lorent, J. H. Thywissen, S. P. Smith, M. Drndić, R. M. Westervelt, and M. Prentiss. Guiding Neutral Atoms on a Chip. Phys. Rev. Lett., 84:1124–7, 2000.
- [45] P Engels, W Ertmer, and K Sengstock. Magnetic guiding of a slow metastable Ne\* beam. Opt. Comm., 204:185, 2002.
- [46] D. Cassettari, B. Hessmo, R. Folman, T. Maier, and J. Schmiedmayer. Beam Splitter for Guided Atoms. Phys. Rev. Lett., 85:5483–5487, 2000.
- [47] D. Müller, E.A. Cornell, M. Prevedelli, P.D.D. Schwindt, A. Zozulya, and D.Z. Anderson. Waveguide Atom Beam Splitter for Laser-Cooled Neutral Atoms. Opt. Lett., 25:1382–4, 2000.
- [48] D. Müller, E.A. Cornell, M. Prevedelli, P.D.D. Schwindt, Y.-J. Wang, and D.Z. Anderson. Magnetic switch for integrated atom optics. Phys. Rev. A, 63:041602, 2001.
- [49] J. Reichel, W. Hänsel, and T. W. Hänsch. Atomic Micromanipulation with Magnetic Surface Traps. Phys. Rev. Lett., 83:3398–401, 1999.
- [50] W. Hänsel, J. Reichel, P. Hommelhoff, and T. W. Hänsch. Magnetic Conveyor Belt for Transporting and Merging Trapped Atom Clouds. Phys. Rev. Lett., 86:608–611, 2001.
- [51] T. Calarco, E. A. Hinds, D. Jaksch, J. Schmiedmayer, J. I. Cirac, and P. Zoller. Quantum gates with neutral atoms: Controlling collisional interactions in time-dependent traps. Phys. Rev. A, 61:022304, 2000.
- [52] P. Horak, B. G. Klappauf, A. Haase, R. Folman, J. Schmiedmayer, P. Domokos, and E. A. Hinds. Towards single-atom detection on a chip. Phys. Rev. A, 67:043806, 2003.
- [53] M. Vengalattore, W. Rooijakkers, and M. Prentiss. Ferromagnetic atom guide with in situ loading. Phys. Rev. A, 66:053403, 2002.
- [54] W. Hänsel, P. Hommelhoff, T. W. Hänsch, and J. Reichel. Bose-Einstein condensation on a microelectronic chip. Nature, 413:498, 2001.
- [55] M. P. A. Jones, C. J. Vale, D. Sahagun, B. V. Hall, and E. A. Hinds. Thermally induced spin flips above an atom chip. arXiv:quant-ph, 0301018.
- [56] A. Kasper, S. Schneider, Ch. vom Hagen, B. Engeser, T. Schumm, I. Bar-Joseph, R. Folman, L. Feenstra, and J. Schmiedmayer. A Bose-Einstein Condensate in a Microtrap. Journal of Optics B: Quantum and Semiclassical Optics, 5:S143–S148, 2003.
- [57] H Ott, J Fortágh, G. Schlotterbeck, A. Grossmann, and C Zimmermann. Bose-Einstein Condensation in a Surface Trap. Phys. Rev. Lett., 87:230401, 2001.
- [58] T. L. Gustavson, A. P. Chikkatur, A. E. Leanhardt, A. Göllitz, S. Gupta, D. E. Pritchard, and W. Ketterle. Transport of Bose-Einstein Condensates with Optical Tweezers. Phys. Rev. Lett., 88:020401, 2002.

- [59] A. E. Leanhardt, A. P. Chikkatur, D. Kielpinski, Y. Shin, T. L. Gustavson, W. Ketterle, and D. E. Pritchard. Propagation of Bose-Einstein Condensates in a Magnetic Waveguide. Phys. Rev. Lett., 89:040401, 2002.
- [60] O. Zobay and B. M. Garraway. Controllable double waveguide for atoms. J. Phys. B, 178:93, 2000.
- [61] E. A. Hinds, C. J. Vale, and M. G. Boshier. Two-Wire Waveguide and Interferometer for Cold Atoms. Phys. Rev. Lett., 86:1462–1465, 2001.
- [62] W. Hänsel, J. Reichel, P. Hommelhoff, and T. W. Hänsch. Trapped-Atom-Interferometer in a Magnetic Microtrap. Phys. Rev. A, 64:063607, 2001.
- [63] E. Andersson, T. Calarco, R. Folman, M. Andersson, B. Hessmo, and J. Schmiedmayer. Multimode Interferometer for Guided Matter Waves. Phys. Rev. Lett., 88:100401, 2002.
- [64] Alex Zozulya. private communication.
- [65] Jason R. Ensher. The First Experiments with Bose-Einstein Condensation of  $^{87}\text{Rb}$ . PhD thesis, JILA, University of Colorado.
- [66] Heather Lewandowski. Coherences and Correlations in an Ultracold Bose Gas. PhD thesis, JILA, University of Colorado.
- [67] D. Mehuys, D. F. Welch, and L. Goldberg. 2.0 W CW, Diffraction-Limited Tapered Amplifier with Diode Injection. Electron. Lett., 28:1944–1946, 1992.
- [68] J. N. Walpole. Semiconductor Amplifiers and Lasers with Tapered Gain Regions. Opt. Quantum Electron., 28:623–645, 1996.
- [69] K. B. MacAdam, A. Steinbach, and C. Wieman. A narrow-band tunable diode laser system with grating feedback and a saturated absorption spectrometer for Cs and Rb. Am. J. Phys., 60:1098 – 111, 1992.
- [70] C. Monroe, H. Robinson, and C. E. Wieman. Observation of the Cesium Clock Transition Using Laser-Cooled Atoms in a Vapor Cell. Opt. Lett., 16:50–2, 1991.
- [71] K. I. Lee, J. A. Kim, H. R. Noh, and W. Jhe. Single-Beam Atom Trap in a Pyramidal and Conical Hollow Mirror. Opt. Lett., 21:1177–1179, 1996.
- [72] W. Petrich, M. H. Anderson, J. R. Ensher, and E. A. Cornell. Behavior of atoms in a compressed magneto-optical trap. J. Opt. Soc. Am. B, 11:1332–1335, 1994.
- [73] C. Cohen-Tannoudjiy, J. Dupont-Roc, and G. Grynberg. Atom-Photon Interactions. Wiley-Interscience, 1992.
- [74] J. Denschlag, D. Cassettari, and J. Schmiedmayer. Guiding Neutral Atoms with a Wire. Phys. Rev. Lett., 82:2014–7, 1999.
- [75] E. Majorana. Nuovo Cimento, 8:107, 1931.

- [76] W. Petrich, M. H. Anderson, J. R. Ensher, and E. A. Cornell. Stable, Tightly Confining Magnetic Trap for Evaporative Cooling of Neutral Atoms. Phys. Rev. Lett., 74:3352, 1995.
- [77] J. Reichel, W. Hänsel, P. Hommelhoff, and T. W. Hänsch. Applications of integrated magnetic microtraps. Appl. Phys. B, 72:81–89, 2001.
- [78] J. Reichel. Microchip traps and Bose-Einstein condensation. Appl. Phys. B, 74:469–487, 2002.
- [79] S. Kraft, A. Günther, H. Ott, D. Wharam, C. Zimmermann, and J. Fortágh. Anomalous longitudinal magnetic field near the surface of copper conductors. J. Phys. B, 35:L496–L474, 2002.
- [80] A. Haase, D. Cassettari, B. Hessmo, and J. Schmiedmayer. Trapping neutral atoms with a wire. Phys. Rev. A, 64:043405, 2001.
- [81] H. Hess. Evaporative cooling of magnetically trapped and compressed spin-polarized hydrogen. Phys. Rev. B, 34:34763479, 1986.
- [82] E. A. Burt, R. W. Ghrist, C. J. Myatt, M. J. Holland, E. A. Cornell, and C. E. Wieman. Coherence, Correlations, and Collisions: What One Learns about Bose-Einstein Condensates from Their Decay. Phys. Rev. Lett., 79:337–40, 1997.
- [83] J. A. Stickney and A. Zozulya. Expansion of a Bose-Einstein condensate from a microtrap into a waveguide. Phys. Rev. A, 65:053612, 2002.
- [84] J. Fortágh, H. Ott, S. Kraft, and C. Zimmermann. Surface effects in magnetic microtraps. Phys. Rev. A, 66:041604(R), 2002.
- [85] Vladen Vuletic and Jakob Reichel. Private communication. Both the Stanford group and the Munich group have not reported an observation of a significant fragmentation effect, and they attribute this to their low number of atoms. .
- [86] A. E. Leanhardt, A. P. Chikkatur, D. Kielpinski, Y. Shin, T. L. Gustavson, W. Ketterle, and D. E. Pritchard. Bose-Einstein Condensates near a Microfabricated Surface. arXiv: cond-mat, 0211345.
- [87] C. Henkel, S. Pötting, and M. Wilkens. Loss and heating of particles in small and noisy traps. Appl. Phys. B, 69:379, 1999.